

Theory of Electronic Transport and Novel Modeling of Amorphous Materials

A dissertation presented to
the faculty of
the College of Arts and Sciences of Ohio University

In partial fulfillment
of the requirements for the degree
Doctor of Philosophy

Kashi Subedi

April 2022

© 2022 Kashi Subedi. All Rights Reserved.

This dissertation titled
Theory of Electronic Transport and Novel Modeling of Amorphous Materials

by
KASHI SUBEDI

has been approved for
the Department of Physics and Astronomy
and the College of Arts and Sciences by

David A. Drabold
Distinguished Professor of Physics and Astronomy

Florenz Plassmann
Dean, College of Arts and Sciences

ABSTRACT

SUBEDI, KASHI, Ph.D., April 2022, NanoScale and Quantum Phenomena Institute
Theory of Electronic Transport and Novel Modeling of Amorphous Materials (127 pp.)
 Director of Dissertation: David A. Drabold

Amorphous materials have myriad applications. There are persistent challenges in understanding their structure due to the absence of long range order. *Ab initio* methods are useful tools to model these materials and determine their microscopic properties. To utilize materials for technological applications, understanding of electronic transport is of central importance. More specifically, for a heterogeneous system, determining conduction-active sites in the network may provide an insight to engineer the material for a desired application. In this dissertation, we describe and develop a novel method to project electronic conductivity onto real-space grids and visualize conduction-active sites in selected materials. To implement the method, we utilize the Kohn-Sham eigenvalues and eigenfunctions obtained from hybrid functional calculations. We then apply the method to study conduction mechanisms in insulating, semi-conducting, metallic and mixed systems.

In this dissertation, we also describe atomistic modeling of two promising resistive memory materials: amorphous aluminum oxide ($a\text{-Al}_2\text{O}_3$) and silicon suboxide ($a\text{-SiO}_x$). For the former case, we study the impact of transition metal Cu in a highly ionic host $a\text{-Al}_2\text{O}_3$ and discuss its effect to electronic structure and transport in the material. We reveal that the Cu atoms segregate and form a cluster or chain-like structure in the oxide host. We find that such Cu-cluster/chain like network forms the major conduction-active sites in the material. For the latter case, we present $a\text{-SiO}_x$ models with $x = 1.7, 1.5$ and 1.3 and study their structure and electronic transport. In our study, we find that the decrease in x results in the complexity of the network with different tetrahedral structures of the form $\text{SiSi}_y\text{O}_{4-y}$, where $y = 0$ to 4 . This results in different types of oxygen

(O)-vacancy sites in the material. We propose that a-SiO_x also has a potential as a computer security device: physical unclonable functions (PUFs) due to the inherent randomness in its structure, particularly for low x .

In the last section of the dissertation, we employ the building-block method to model sodium silicate glasses among the most important glasses for practical application. We provide a detailed study of structural, electronic and thermal properties with varying concentration of modifier (Na₂O) in the glass (SiO₂). For the first time (to our knowledge), we have computed the linear thermal expansion coefficient using first principles and our results find close agreement with experiments.

In memory of my grandparents and dedicated to my mother

ACKNOWLEDGMENTS

Throughout my PhD and writing the dissertation, I have received a great support and assistance from people and organizations.

First, I would like to express my sincere gratitude to my advisor Prof. David A. Drabold who guided me throughout the PhD. His continuous support, motivation and feedback has made me enthusiastic and focused on my research. The knowledge and expertise that he has shared with me will be valuable resource during my future endeavours.

I would like to thank Dr. Gang Chen, Dr. Michael Kozicki, Dr. Frank Kraft, Dr. Keerti Kappagantula and Dr. Venkatesh Botu with whom we collaborated in different projects during these four and a half years of my doctoral research. I appreciate Dr. Michael Kozicki for sharing his ideas on transport in resistive memory devices and physical unclonable functions that led to my research projects. I would like to thank my committee members for their valuable time and suggestions.

I am especially thankful to my senior group member Dr. Kiran Prasai for his valuable suggestions that were helpful during my research. I want to thank other senior members Dr. Bishal Bhattarai and Dr. Dale Igram for their help and support during my early stages of the PhD program. I would also like to thank my colleagues Rajendra Thapa, Chinonso Ugwumadu and Kishor Nepal for their discussions and suggestions.

I am grateful to Donald Roth for his assistance in setting up and managing computing resources.

I would like to extend my acknowledgement to Ohio University and department of Physics and Astronomy for providing me a suitable environment and resources to pursue my doctoral degree. I would also like to extend my sincere thanks to all the funding agencies Pacific Northwest National Laboratory (PNNL), US Department of Energy and Nanoscale and Quantum Phenomena Institute (NQPI). I want to acknowledge the computing resources from Ohio Supercomputer Center (OSC) and the Extreme Science

and Engineering Discovery Environment (XSEDE). I also want to thank staff at Pittsburgh supercomputer center who provided training on high performance computing that was useful during my research.

I would also like to thank Dr. Björn Lüssem for guiding me during master's degree research.

I would like to express my gratitude to my mother, wife, son, sister, wife's mother for their love and support. I would also like to thank other members of my family, relatives and friends who have directly or indirectly supported me.

TABLE OF CONTENTS

	Page
Abstract	3
Dedication	5
Acknowledgments	6
List of Tables	11
List of Figures	12
List of Acronyms	18
1 Introduction	19
1.1 Background	19
1.2 Theoretical Study of Amorphous Solids	20
1.3 Commonly used Descriptors of Amorphous Solids	23
1.3.1 Structural Topology	23
1.3.2 Electronic Structure	24
1.3.3 Lattice Dynamics	25
1.4 Dissertation Outline	26
2 Real-Space Projection of Electronic Conductivity	27
2.1 Introduction	27
2.2 Kubo Formula	28
2.3 Computing Spatial Information about Transport	30
2.4 Theory	31
2.4.1 Spatially Projected Conductivity (SPC)	31
2.4.2 Spectral Properties of the Conduction Matrix	33
2.5 Computational Details	34
2.5.1 Models	34
2.5.2 Methods	35
2.6 Results and Discussion	35
2.6.1 Low Density Amorphous Carbon (a-C)	35
2.6.2 Amorphous Silicon	40
2.6.3 Conductivity Fluctuations in Liquid Silicon	44
2.6.4 Amorphous Silicon Suboxide: Application for Finite ω	48
2.6.5 FCC Aluminum	50
2.7 Conclusions	54

3	Structural Origins of Electronic Conduction in Amorphous Copper-doped Alumina	56
3.1	Introduction	56
3.2	Computations	58
3.2.1	Model Generation	58
3.2.2	Spatial Projection of Electronic Conductivity	58
3.3	Results and Discussion	59
3.3.1	Bonding and Topology of the Models	59
3.3.2	Electronic Structure	62
3.3.2.1	Density of States and the Localization	62
3.3.2.2	Charge Analysis on Cu Atoms	64
3.3.2.3	Thermally Driven Conduction Fluctuations	67
3.3.2.4	Space-Projected Conductivity	68
3.3.3	Ion and Lattice Dynamics	69
3.3.3.1	Ionic Motion	69
3.3.3.2	Lattice Dynamics	71
3.4	Conclusions	73
4	Electronic Conduction in Amorphous Silicon Suboxides	75
4.1	Introduction	75
4.2	Computational Details	76
4.2.1	Generation of Atomistic Models	76
4.3	Results and Discussion	77
4.3.1	Structural Topology	77
4.3.2	Electronic Structure	80
4.3.2.1	Density of States and Localization	80
4.3.3	Conduction Active Parts of the Network	81
4.4	Conclusions	84
5	Atomic Properties of Sodium Silicate Glasses using Building-Block Method	85
5.1	Introduction	85
5.2	Methodology and Computational Details	87
5.2.1	Generation of Models using Building Block Method	87
5.2.2	Quasi-Harmonic Approximation	89
5.3	Results and Discussion	91
5.3.1	Structural Properties	91
5.3.2	Electronic Properties	101
5.3.3	Thermal Properties	103
5.3.4	Elastic Properties	104
5.4	Conclusions	107
6	Conclusions	109
6.1	Future Work	111

References 114

LIST OF TABLES

Table	Page
3.1 Initial and Final Densities of α -Al ₂ O ₃ :Cu Models	59
3.2 Average Coordination Numbers around Cu Atoms for 10%, 20% and 30% Cu Models.	61
4.1 System Stoichiometries and Densities for SiO _x Models	77
5.1 Average Coordination Number (n) and its Distribution Among Each Atomic Pairs $n()$, where () is Filled by the Corresponding Atomic Species. The Coordination is Counted Only if the Distance for Each Atomic Pair is no More than the Sum of Their Covalent Radii Plus a Tolerance Factor of 0.1 Å. Covalent Radii of 1.11, 0.73 and 1.66 Å was Taken for Si, O and Na Atoms Respectively.	100
5.2 Elastic Properties Obtained From (Na ₂ O) _x (SiO ₂) _{1-x} Models	106

LIST OF FIGURES

Figure	Page	
2.1	a-C: Left and right correspond to the SPC (ζ) and the diagonal approximation $\Delta(\mathbf{x})$ projected on grids as an isosurface plot (yellow blobs) respectively. The middle plot corresponds to the structural topology of the network in one region of the supercell that forms a continuous conduction path. The straight and the curved lines with arrowhead are guides to the eye to indicate the conduction path. The colored spheres represent C atoms with different configurations; Red (sp^3), blue (sp^2), green (sp) and purple (singly bonded).	37
2.2	a-C: Logarithmic spectral density of states of Γ -matrix. The left scale represents the DOS of the eigenvalues displayed in a log scale (solid black line) and the right scale corresponds to the extent of localization of eigenvectors measured as IPR (\mathcal{I}) (red circles). Large \mathcal{I} implies a spatially localized eigenvector of Γ	38
2.3	a-C: Spectral form for SPC (ζ_s) projected on grids as an isosurface plot (yellow blobs). Left and right plots correspond to the ζ_s from the sum of last 75 and 100 eigenvectors respectively. Same cutoff for the isosurface has been used in both plots and the left plot in Figure 2.1. Same color code is used to describe atoms as in Figure 2.1. ζ_s from extreme 75-100 eigenvectors is equivalent to ζ and is sufficient to essentially exactly determine the SPC in a-C.	39
2.4	a-C: Eigenvectors projected on grids as an isosurface plot (yellow blobs). Left and right plots correspond to the second largest ($\Lambda_\mu = 22.04$ S/cm) and the largest ($\Lambda_\mu = 31.98$ S/cm) eigenvalues respectively (ref Figure 2.2). Same color code is used to describe atoms as in Figure 2.1.	39
2.5	a-Si: SPC (ζ) projected on grids as heat map plot (labeled by colorbars on left of the plot) scaled with maximum value in each plot. The size of the hot spheres is scaled with the magnitude of the SPC value. The colored spheres represent Si atoms with different bonding environment; The blue and heliotrope colored spheres represent 4-fold coordinated Si atoms with one and two very long Si-Si bonds respectively. The green colored spheres represent typical Si atoms with "normal" bondlengths. The bond cutoff distance of 2.72 \AA was chosen.	41
2.6	a-Si: Logarithmic spectral density of states of Γ -matrix. The left scale corresponds to density of states (DOS) of the eigenvalues displayed in a log scale (solid black line) and the right scale corresponds to the extent of localization measured as IPR (\mathcal{I}) (red circles).	42

- 2.7 a-Si: Eigenvectors projected on grids as an isosurface plot (yellow blobs). Left and right plots correspond to the second largest ($\Lambda_\mu = 0.26$ S/cm) and the largest ($\Lambda_\mu = 0.34$ S/cm) eigenvalues respectively. For atoms, the color code is same as used in Figure 2.5. Since the atoms picked by the eigenvectors that are adjacent to each other are separated by the periodic box, we shifted the coordinates to make these atoms include in the same side of the box to make the connectivity clear. The left panel emphasizes short bonds, right panel long bonds and defects. 43
- 2.8 l-Si: A snapshot showing fluctuations of energy levels near the Fermi-level (units in eV) plotted against simulation time. The inset plot shows a specific region (shown by the curly brace) with closing and opening of the electronic gap. The markers correspond to the time step for the atomic configurations that were selected for the SPC calculations. 45
- 2.9 l-Si: SPC (ζ) projected on grids as a heat map (labeled by colorbars on left of each subplots) for atomic configurations at that are temporally close to each other shown by the marker signs in the inset plot of Figure 2.8. a), b), c) and d) correspond to the atomic configurations shown by star, triangle, square and the plus signs in the inset plots of Figure 2.8 respectively. Atom color represent Si with different instantaneous coordination as labeled as shown at the top of the figure. The cutoff distance of 3.10 \AA is used to define the coordination. 46
- 2.10 l-Si: SPC (ζ) projected on grids as a heat map plot (labeled by colorbars on left of each subplots) for configurations at intervals of 1.2 ps. a), b), c) and d) correspond to the SPC plot at simulation time 1.95, 3.15, 4.35 and 5.55 ps respectively. Atoms color represent Si with different coordination environment and we adopt the same convention as in Figure. 2.9. The cutoff distance of 3.10 \AA is used to define the coordination. Note the spatial fluctuation in the heat maps over these snapshots. 47
- 2.11 a-SiO_{1.3}: SPC (ζ) projected on grids as isosurface (yellow blobs) plots. Left and right plots correspond to $\hbar\omega = 0.62$ eV and 0.76 eV respectively. Multicolored spheres refer to Si atoms within the conduction-active region having different coordination environment shown as legends at the top of the figure. Top 3.7% SPC values are included in both plots. The gray colored spheres represent Si and O atoms that lie outside the conduction active region for the given cutoff. The small size spheres represent O atoms. 49
- 2.12 c-Al: Logarithmic spectral density of states of Γ -matrix. The left scale corresponds to density of states (DOS) of the eigenvalues displayed in a log scale (solid black line) and the right scale corresponds to the extent of localization measured as IPR (\mathcal{I}) (solid red circles). The inset shows the magnitude of conduction eigenvalues in ascending order. 51
- 2.13 c-Al: The correlations of the eigenvalues with IPR (\mathcal{I}) shown by the scattered plots as heatmap. The colorbar at the central top of the figure refers to the magnitude of eigenvalues. 52

2.14	c-Al: Conductivity projected on grids weighted by the eigenvalues from all eigenvectors as a heat map plot (labeled by colorbars on the left) scaled with maximum value. The spheres represent Al atoms.	53
2.15	c-Al: Isosurface plots for eigenvectors corresponding to the degenerate eigenvalues ($\Lambda_\mu = 1.0013$ S/cm). The isosurface plot displayed as a heat map (labeled by the colorbars on left of each subplots) includes the values within 0.001 times the maximum value on the grids. Al atoms are represented by gray spheres in each plot.	54
3.1	$g(r)$ and $S(q)$ of a-Al ₂ O ₃ : (a) $g(r)$ computed on models are compared with measured $g(r)$. (b) $S(q)$ computed on models are compared with measured $S(q)$. (c) and (d) partial $g(r)$ and partial $S(q)$ respectively for Al-O, O-O and Al-Al pairs	60
3.2	Total $g(r)$ computed from the models of a-Al ₂ O ₃ :Cu at various concentrations of Cu. The hump appearing in Cu-doped models, indicated by arrow, originates from Cu-Cu correlation.	61
3.3	Final relaxed a-Al ₂ O ₃ :Cu models. Top plots (from left) represent for 0%, 10% Cu and bottom plots (from left) represent for 20% and 30% Cu. Atoms color: Al (gray), Cu (blue) and O (red).	62
3.4	Electronic density of states (EDOS) and the inverse participation ratio (IPR) computed from a-Al ₂ O ₃ :Cu models for different concentrations of Cu. The black curve represents EDOS and red vertical lines show IPR. The Fermi level is shifted to zero in all plots.	63
3.5	Projected electronic density of states (EDOS) computed from a-Al ₂ O ₃ :Cu models with 20% Cu. (a) Site projected EDOS (b) Orbital projected EDOS. The Fermi energy is shifted to zero.	65
3.6	Net Bader charge on Cu atoms calculated from a-Al ₂ O ₃ :Cu models with 20% Cu-concentration. A color code displayed on top is used to represent the charge state. Charge state of zero, shown by green, represents a neutral Cu atom; the charge values are in units of electronic charge. All Cu-atoms are shown in color. Light gray atoms represent Al and O atoms within the first cutoff distance of Cu atoms	66
3.7	Fluctuation of HOMO, LUMO and HOMO-LUMO gap (η) with time for 20% model at 1000 K. $\eta(t)$ is represented by black line with its values given by right axis of the plot as shown by arrowhead in the plot.	68
3.8	Overlaying SPC values (orange transparent spheres) with atomic configuration: On the left, large gap (high resistance) state of a-Al ₂ O ₃ :Cu model with 20% Cu. On the right, small gap (low resistance) state of the same system. Color nomenclature: blue- Cu atom, red- O atom and gray- Al atom. The bond length of cutoff 2.6 Å is chosen. Circles with same color represent same part of local configurations. There is a factor of about 10 ⁴ between the conductivities of the two conformations.	70
3.9	Mean-squared displacement at 800 K and 1000 K for 20% Cu model.	71

3.10	Normalized total and partial vibrational density of states for 10% and 30% of Cu models.	72
3.11	Vibrational IPR different models. Left column for 10% model and the right column for 30% model.	73
4.1	LEFT: Pair correlation function $g(r)$ with inset showing the partial $g(r)$ due to Si-Si bonding. RIGHT: Local coordination environment for Si atoms (frequencies expressed in percentage). The inset plots correspond to the correlations that belong only to that model. The first index of the label represents Si and the second index represents O atom.	78
4.2	Relaxed structure for a-SiO _x model with $x = 1.3$. The color of Si atoms correspond to the coordination of Si in the network within the first nearest distance for each atom pairs. The color code is same as the right plot of Fig. 4.1. The O atoms are colored gray.	79
4.3	LEFT: Electronic density of states (EDOS) and the inverse participation ratio (IPR) for a-SiO _x models. RIGHT: Electronic density of states projected on to each orbital of each atomic species for a-SiO _x models.	80
4.4	Iso-surface plots showing SPC (yellow colored blobs) for intrinsic a-SiO _x models. From left to right representing for $x = 1.7, 1.5$ and 1.3 respectively. The Si atoms within the conduction-active region are color coded same as in right plot of Fig. ???. The conductivity values up to 0.04 times the highest value are considered in each plot. The remaining Si and O atoms are shown by gray color, O atom being represented by small spheres. The order of the magnitude of SPC is different in each plot.	82
4.5	Iso-surface plots (yellow-colored blob) showing SPC for $x = 1.3$ model with shifted Fermi-level. LEFT: Valence-tail region (Fermi-level at ≈ -2.0 eV) and RIGHT: Conduction-tail region (Fermi-level at ≈ 2 eV). The cutoff up to 0.04 times the highest value is considered. Same color code description used in Figure 4.4.	83
5.1	Schematic “flow chart” for building-block (BB) method. (a) Initial configurations of atoms in the sub-unit cell. (b) The sub-unit cell with minimum energy from several melt-quench cycles. (c) 8×8×8 supercell formed from the optimized sub-unit cell. (d) The final model formed after one melt-quench cycle followed by relaxation.	89
5.2	Total distribution function $T(r)$ and the Structure factor $S(q)$ for sodium silicate models with $x = 0.0$ and 0.3 respectively. The left and right subplots correspond to $T(r)$ and $S(q)$ respectively.	91

- 5.3 Radial distribution function $g(r)$ (left subplot) and bond length distribution of Si and O atoms (right subplot) for $(\text{Na}_2\text{O})_x(\text{SiO}_2)_{1-x}$ models. The inset in left subplot shows partial $g(r)$ attributed to Na-O correlations for the doped models. Solid and dashed lines in legends in right subplot correspond to bonding of Si with bridging oxygen (BO) and non-bridging oxygen (NBO) atoms respectively. NBO atoms here refer to O atoms that are linked to only one Si atom. BO atoms refer to O atoms that are not NBO atoms. 93
- 5.4 Bond angle distribution functions (BADF) for the $(\text{Na}_2\text{O})_x(\text{SiO}_2)_{1-x}$ models within the first cutoff distance for each atomic pairs showing the contribution of BO and NBO atoms. “A” in the legend refers to either Si or Na atom and black solid line corresponds to total distribution for each case. Left and right subplots correspond to O-Si-O and O-Na-O angles respectively. BO and NBO atoms used here are same as defined in Figure 5.3. 95
- 5.5 Bond angle distribution functions (BADF) corresponding to Si-BO-Si angles for the $(\text{Na}_2\text{O})_x(\text{SiO}_2)_{1-x}$ models shown by black lines in all subplots. The distribution decomposed based on number of modifier atom (Na) that are linked to BO atoms shown by the colored lines and labeled at the top of the figure for the doped models. The cutoff distance of 2.74 Å for Na-O pairs is used. 97
- 5.6 Q^n distribution for the doped models. The red and blue bars correspond to the calculated Q^n from the relaxed models with $x = 0.1$ and 0.3 respectively. The light blue bars correspond to the experimental data estimated for $x = 0.3$ from reference [1]. A cutoff distance of 1.94 Å is used to define the bonds between Si and O atoms based on their covalent radii plus a tolerance factor of 0.10 Å. 99
- 5.7 (a) Total and projected electronic density of states (EDOS), and the inverse participation ratio (IPR) for $(\text{Na}_2\text{O})_x(\text{SiO}_2)_{1-x}$ models.(b) and (d) Partial charge density for the defect state in the gap shown as iso-surface (purple colored blobs) plots for the doped models with $x = 0.1$ and 0.3 respectively. (c) and (e) show close look of the defect sites in (b) and (d) respectively. Atoms color match with the legends in (a). 101
- 5.8 (a) Helmholtz free energy obtained for seven different volumes at selected temperatures shown by the filled circles. The dashed lines represent the fit to the EOS. The black star symbols represent the Gibb’s free energy. (b) The volume vs temperature plot for the doped model with $x = 0.3$. (c) Linear thermal expansion coefficient (LTEC) for both doped models. 103
- 5.9 Specific heat capacity at constant pressure (C_p) for $(\text{Na}_2\text{O})_x(\text{SiO}_2)_{1-x}$ models with $x = 0.1$ and 0.3 shown by solid lines and the experimental values for $x = 0.33$. The triangle and star symbols correspond to the values taken from references [2, 3]. 105

- 6.1 a), b), c): Conductivity projected on grids closest to crystallographic planes 010, 011 and 111 containing a vacancy as a 2D gray scale plot. The magnitude of conductivity increases from white to black. The colored lines with small spheres are just for guide to an eye representing different directions from the vacancy. d), e), f): Variation of conductivity with distance from the grid closest to the vacancy along different directions on planes 010, 011 and 111 respectively. θ and ϕ refer to the polar and azimuthal angles respectively. Color of legends in d), e) and f) match with the lines shown in a), b) and c) respectively. 112

LIST OF ACRONYMS

AIMD	<i>Ab initio</i> molecular dynamics
BADF	Bond angle distribution function
BO	Bridging oxygen
CBRAM	Conducting bridge random access memory
CNT	Carbon nano-tube
CRN	Continuous random network
DFT	Density functional theory
DOS	Density of states
EDOS	Electronic density of states
FCC	Face centered cubic
GGA	Generalized gradient approximation
HOMO	Highest occupied molecular orbital
IPR	Inverse participation ratio
IRO	Intermediate range order
KGF	Kubo-Greenwood formula
LDA	Local density approximation
LRS	Low resistance state
LUMO	Lowest unoccupied molecular orbital
MD	Molecular dynamics
MSD	Mean-squared displacement
NBO	Non-bridging oxygen
PAW	Projector augmented wave
PUF	Physical unclonable function
RAM	Random access memory
RDF	Radial distribution function
RRAM	Resistive random access memory
RMC	Reverse monte carlo
SPC	Space projected conductivity
VASP	Vienna <i>ab initio</i> simulation package
VDOS	Vibrational density of states
VIPR	Vibrational inverse participation ratio
WWW	Wooten Winer Weaire

1 INTRODUCTION

1.1 Background

This dissertation is concerned with simulating of amorphous and glassy materials that have technological importance. The work is focused primarily on transport properties of electronic materials that have potential applications for the resistive memory devices and physical unclonable functions (PUFs). The growth of the Internet of Things (IoT) and neuromorphic computing has demanded memory devices with high data density and reduced power consumption. The limitation of scaling of the conventional electronics due to charge leakage [4, 5] has required non-volatile memory and the logic devices based on new concepts and materials [6]. Non-volatile memory devices based on resistive switching behavior have emerged as a promising alternative to the conventional Si-based memory devices in terms of device simplicity, low power consumption, switching speed and high density integration [7, 8, 9]. Several different devices have been proposed that work on different physical concepts [10]. These devices function by switching the conductivity of the material between high and low resistance states upon applying voltage to the metal-insulator-metal (MIM) memory cell. Amorphous forms of insulating metal oxides such as aluminium oxide [11, 8, 12], silicon oxide [13, 14], tantalum oxide [15, 16], hafnium oxide [17] are among studied materials for resistive memory devices. Beside metal oxides, chalcogenides [18, 19] are also promising for these devices. With the growth of IoT, data confidentiality and authentication have become equally important along with its storage. The current practice of providing a secure memory or authentication using electrically erasable programmable ROM (EEPROM) or static random access memory (SRAM) are usually expensive both in terms of design and power consumption [20]. Using physical keys, commonly termed as PUFs, is a promising alternative for secret key storage without any expensive hardware [21]. The PUF is a

physical observable derived from inherent randomness of the structure such that each physical realization of the PUF produces a stable and unique identifier. Such identifiers are difficult to be cloned, guessed, stolen or shared. Amorphous silicon and carbon nanotubes (CNTs) have been studied for PUF applications [22, 23]. Experimental evidence has suggested that amorphous silicon suboxides are promising materials for the PUF applications [24].

These computer technologies (resistive memory devices, conducting bridges RAM, PUF devices) involve poorly understood conduction pathways, and the microscopic understanding of such systems might be improved by a detailed atomistic study of the flow of charge through the systems. For such heterogeneous systems, an answer to a basic question “ what parts of the network are conducting” is important to optimize these devices.

Sodium silicate glass is a prototype multi-component glasses that has many applications in photonics, and bio-material engineering [25, 26, 27]. Despite their importance, the atomic structure, thermal and mechanical properties of these glasses is still not well understood. To fully exploit these glasses for practical applications, fundamental insight about the atomic structure and their interactions is required.

1.2 Theoretical Study of Amorphous Solids

A widely accepted approach to model amorphous solids is the *continuous random network* (CRN) proposed by W. H. Zachariasen [28]. The CRN model assumes that every atom that is fully coordinated according to Mott’s ‘8- N rule’ [29], where N is the number of valence electrons. Such a model possesses homogeneous disorder and absence of ordered crystalline zones and voids. The model also assumes that there is an absence of long range order in the network. Gutmann built the first computer CRN model in 1976 [30]. The CRN models are often successful for describing electronic and structural

properties of the materials. Wooten, Winer and Weaire introduced an algorithm which was able to produce experimentally plausible CRN models for amorphous column IV materials based on a Monte Carlo bond switching scheme [31]. This method assumes *a priori* information of the coordination environment of all atoms and the Monte-Carlo moves needed that includes a Maxwell-Boltzmann factor. The method is limited to handful of systems. These models are still used as the references for comparison with other newer theoretical methods.

Molecular dynamics (MD) is now the standard approach to obtain atomistic models of amorphous and glassy materials. It was introduced by Alder and Wainwright [32, 33] in the late 1950s. It aims to study a system of interacting particles in a way as close to the real world as possible and simulate its dynamics over a physical time scale that is relevant to properties of interest. In this method, atoms are represented by the point particles and Newton's equations of motion are integrated numerically. The time step has to be chosen to be tiny ($\approx 10^{-15}$ fs) because of the natural time scale of atomic dynamics [34, 35]. A system is heated at a temperature higher than the melting point so that it forgets its initial configuration. The system is then quenched to obtain the low energy models representing the given material. This method is commonly called as "melt-quench method". This method is not free from limitations. It usually freezes in too many defects and may lead to localized states in the gap that are rare or absent in real materials. The accuracy of the MD approach depends upon the system size, the time scale and the quality of interatomic forces to describe the interactions among the atoms in the system of electrons and ions.

The MD method is mostly used with two types of interactions, namely empirical and quantum mechanical. Empirical potentials are generated by guessing a functional form that mostly involve bonding (bending, stretching, etc.) and other interactions such as electrostatic, van der Waals, etc. The functional form has free parameters which may be tuned such that the experimentally observed properties are reproduced. The quality of

potentials determine the accuracy and validity of the models. MD using empirical potentials are computationally inexpensive and therefore larger models with thousands of atoms can be simulated. Such approaches suffer severely from transferability issues (the capability of correctly representing energetics of diverse configurations). Such potentials are mostly focused on unary or binary systems. It is quite difficult to accurately predict the correct potential for multi-component systems having complex structure. The quantum mechanical interactions on the other hand involve detailed electronic structure computations. The electronic Hamiltonian of a system with N_e electrons and N_n nuclei can be expressed as:

$$H = - \sum_i^{N_e} \frac{\hbar^2}{2m_e} \nabla_i^2 + \frac{e^2}{4\pi\epsilon_0} \left[- \sum_i^{N_e} \sum_I^{N_n} \frac{Z_I}{|r_i - R_I|} + \frac{1}{2} \sum_i^{N_e} \sum_{j,j \neq i}^{N_e} \frac{1}{|r_i - r_j|} + \sum_I^{N_n} \sum_{J,J \neq I}^{N_n} \frac{Z_I Z_J}{|R_I - R_J|} \right] \quad (1.1)$$

where indices i and j run over the electronic degrees of freedom (DOF) and I and J run over nuclear DOF. Z represents the atomic number of a given nucleus. The first term in the expression of H corresponds to the kinetic energy operator for electrons, the second term corresponds to nuclei-electron interactions, the third term corresponds to electron-electron interactions and the last term corresponds to nuclei-nuclei interactions. We have already decoupled nuclear and electron degrees of freedom using the Born-Oppenheimer approximation [36] that assumes nuclei are frozen in their equilibrium position in electronic timescale. Directly solving the Schrodinger equation for a real many particle systems is almost an intractable problem. The many-body problem was made simplified by Dirac, Slater, Kohn, Hohenberg and Sham [37, 38, 39, 40] by treating the ground state electron density $\{n(r)\}$ instead of many-body wavefunctions. This approach is known as density functional theory (DFT). This method uses the exchange-correlation energy functional which is not known and different approximations are used for it. Modern efficient and accurate implementations of DFT involving technical details that are authoritatively discussed in reference [41].

1.3 Commonly Used Descriptors of Amorphous Solids

In order to interpret the atomic properties of amorphous materials, we require mathematical ways to compute different quantities.

1.3.1 Structural Topology

The structure of amorphous materials underlies its other atomic properties. The radial distribution function $g(r)$ describes the atomic pair correlations as a function of distance and is generally expressed as [42, 43]:

$$g(\vec{r}) = \frac{1}{\rho N} \sum_i \sum_{j \neq i} \delta(\vec{r} - \vec{r}_i) \delta(\vec{r} - \vec{r}_j) \quad (1.2)$$

where $\rho = N/V$ is the number density. N and V represent the number of atoms and the volume of the cell used. \vec{r}_i represents the position of i^{th} atom with respect to the reference atom. To obtain the radial distribution function $g(r)$, we average $g(\vec{r})$ over the space:

$$g(r) = \int \frac{d\Omega}{4\pi} g(\vec{r}) \quad (1.3)$$

This reduces to

$$g(r) = \frac{1}{4\pi\rho r^2 N} \sum_{i \neq j} \delta(r - r_{ij}) \quad (1.4)$$

where r_{ij} is the distance between atom i and atom j . The radial distribution function contains structural information of the amorphous materials. For unary system, the first peak provides information about the nearest neighbor bond length and coordination. The first minimum gauges the extent of the short range order. Medium range order is characterized by intermediate peaks beyond the first coordination sphere. For longer distances, $g(r)$ flattens out to unity. For multi-component systems, partial correlations are used to compute the correlations between different atomic species and are expressed as:

$$dn_{\alpha\beta} = 4\pi r^2 \rho_{\beta} g_{\alpha\beta} dr \quad (1.5)$$

where $dn_{\alpha\beta}$ is the average number of atoms with β species between distance r and $r + dr$ from the center α atom. ρ_β is the number density of β species. To obtain the total radial distribution functions, we need to obtain the weighted sum over the partial $g_{\alpha\beta}(r)$:

$$g(r) = \frac{1}{N^2} \sum_{\alpha, \beta} N_\alpha N_\beta g_{\alpha\beta}(r) \quad (1.6)$$

where N_α and N_β represents the number of atoms with species α and β respectively.

Experimental methods like neutron or X-ray diffraction are used to probe the structure in a form of smooth function in reciprocal space known as the static structure factor $S(q)$. The radial distribution function can also be expressed as a Sine transform of $S(q)$:

$$g(r) = 1 + \frac{1}{2\pi r \rho_o} \int_0^\infty q[S(q) - 1] \sin(qr) dq \quad (1.7)$$

1.3.2 Electronic Structure

The electronic structure is mostly studied by the electronic density of states (EDOS) which is still an appropriate concept that can be carried from crystalline to amorphous systems. The EDOS is defined as:

$$g(E) = \frac{1}{N} \sum_{i=1}^N \delta(E - E_i) \quad (1.8)$$

where N is basis size and E_i is the eigenvalue of i^{th} electronic (Kohn-Sham) eigenvector. The EDOS provides information concerning the electronic band gap and also the states that are present near the Fermi-level which are always of key interest to transport and optical calculations. The band gap is associated with electronic conductivity which describes the transport properties in the material. Amorphous materials possess structural disorder so that electronic states are not all extended as in crystals. The localization of the electronic states is generally gauged by inverse participation ratio (IPR) [44] and is defined as:

$$\mathcal{I}(\psi_n) = \frac{\sum_1^N a_{ni}^4}{(\sum a_{ni}^2)^2} \quad (1.9)$$

where a_{ni} are the contribution to the eigenfunction ψ_n from the i^{th} projected atomic orbital obtained from VASP. In our case, \mathcal{I} ranges from 0 to 1. Larger \mathcal{I} signifies that the states are localized on fewer atomic sites, whereas the smaller \mathcal{I} indicates states are evenly distributed over many atomic sites.

1.3.3 Lattice Dynamics

The lattice dynamics of amorphous materials can be studied from the quantities such as vibrational density of states (VDOS), vibrational IPR, etc. In this dissertation, we study these quantities within the harmonic approximation using first principles methods. The vibrational eigenfrequencies and eigenmodes are obtained by diagonalizing dynamical matrix. The normalized VDOS and the partial VDOS are expressed as [45]

$$Z(E) = \frac{1}{3N} \sum_n \delta(E - \hbar\omega_n) \quad (1.10)$$

$$Z_\alpha(E) = \frac{1}{3N} \sum_{i \in \alpha} \sum_n |e_i^n|^2 \delta(E - \hbar\omega_n) \quad (1.11)$$

where ω_n are the normalized eigenfrequencies ($3N$ in total). Here, the sum over i is over all the atoms belonging to the species α and e_i^n corresponds to the displacement vector (vibrational eigenstate) of atom i with Cartesian components $e_{i\mu}^n$ where $\mu = x, y$ and z . The vibrational IPR is useful to understand the nature of the vibrations. Similar to IPR that we defined for electronic structure, the vibrational IPR can be calculated from the eigenvectors as:

$$\mathcal{I}(e^n) = \frac{\sum_{i=1}^N |e_i^n|^4}{(\sum_{i=1}^N |e_i^n|^2)^2} \quad (1.12)$$

The values of VIPR range from 0 to 1. For a given eigenmode, higher value signifies that the vibrations are localized to few atoms and lower value implies that the vibrations are evenly distributed among many atoms.

1.4 Dissertation Outline

The remainder of the dissertation is organized in the following way: In chapter 2, we give a fairly self contained treatment of charge transport treated by DFT and significantly extend these conventional methods. We spatially decompose electronic conductivity onto real-space grids. In this method, we construct a Hermitian positive semi-definite matrix which we call the *conduction matrix*. It has interesting spectral properties and maps the computation of conduction paths onto a diagonalization. We apply the method to study electronic transport in semiconducting, metallic and mixed systems. In chapter 3, we model an aluminum oxide (a promising resistive material) with varying concentrations of copper into it. We discuss its structural, vibrational properties and apply the method of Chapter 2 to electronic transport. In chapter 4, we provide atomistic modeling of another promising resistive memory material: amorphous silicon suboxide. We vary the O-deficient sites in the material and study the structural topology of this material. We compute conduction pathways in this material and introduce it as a promising candidate for physical unclonable functions. In chapter 5, we utilize the building block method to model sodium silicate glasses and study their atomic properties with focus on structural topology and thermal expansion coefficients.

2 REAL-SPACE PROJECTION OF ELECTRONIC CONDUCTIVITY

The work presented in this chapter has been published as **Subedi, K. N., Prasai, K., and Drabold, D. A.** *Space-projected conductivity and spectral properties of conduction matrix*, Phys. Status Solidi B 258, 2000438 (2021).

2.1 Introduction

Practical calculation of electron transport in materials [46] always involves assumptions and approximations. The most natural and oldest approach is to employ Boltzmann's equation [47], which is ideal for a crystalline system with relatively weak impurity or thermal disorder. It describes the dynamics of the electron distribution function that takes into account of external fields and scattering process. It can also describe quantum interference effects by including the non-local terms into the collision integral [48]. A different way of framing the problem is due to Kubo [49], who in 1957 computed the linear response (current) to an external electric field. The resulting expression for the electrical conductivity, further approximated within a single-particle picture of the electronic structure [50] is called the Kubo-Greenwood formula (KGF). This was later generalized as the "Fluctuation-Dissipation theorem", that mathematically connects dissipative processes with equilibrium fluctuations [51]. The ultimate roots of this work extend through time to Einstein and his work on Brownian motion and diffusion [52].

In this chapter, we review the Kubo-Greenwood formula and discuss the background materials on computing the spatial transport information from computer models of materials. We then describe the method to compute space projected conductivity and apply it to different systems: a low density phase of amorphous carbon, amorphous and liquid silicon, amorphous silicon suboxide, and for a useful contrast, FCC aluminum. We also discuss the conduction in terms of conduction eigenmodes.

2.2 Kubo Formula

For calculations of charge transport in disordered systems, it is natural to adopt the Kubo approach. Mott and Davis [53] and Moseley and Lukes [54] offered an appealing physical derivation of the KGF that we tersely repeat here. Consider a system with an applied (external) AC electric field \mathbf{E} . The system absorbs photons from the electromagnetic field, and this drives electronic transitions near the Fermi level, ϵ_F . Associated with this field, there is an electric current density \mathbf{j} . The Joule heat produced by the electric field per unit time is $\Omega \mathbf{j} \cdot \mathbf{E}$, where Ω is the cell volume. The rate at which energy is absorbed from electronic transitions is $\gamma = \sum_{if} \epsilon_{fi} (w_{fi} P_i - w_{if} P_f)$. Here ϵ_{fi} is the energy difference between initial and final states, w_{fi} is the transition probability per unit time between final state f and initial state i , $P_{i(f)}$ is the occupation probability of the initial (final) state. Next, one assumes that $\gamma = \Omega \mathbf{j} \cdot \mathbf{E}$. By using Fermi's Golden Rule to estimate the transition probabilities, and defining the conductivity σ from the identification that $\sigma E^2/2$ is the mean rate of energy loss per unit volume, one obtains the KGF for each k -point \mathbf{k} [49, 50] (written here in a form most convenient for our purposes):

$$\sigma_{\mathbf{k}}(\omega) = \sum_{i,j} g_{ij}(\mathbf{k}, \omega) \sum_{\alpha} |p_{ij}^{\alpha}|^2. \quad (2.1)$$

In the shorthand notation of Equation 2.1, we averaged over diagonal elements of the conductivity tensor¹ ($\alpha = x, y, z$), i and j index Kohn-Sham orbitals (or other single-particle states) $\psi_{i,\mathbf{k}}(x)$ with associated energies² $\epsilon_{i,\mathbf{k}}$, p^{α} is the momentum operator and $g_{ij}(\mathbf{k}, \omega) = 2\pi e^2 [f_i(\mathbf{k}) - f_j(\mathbf{k})] \delta(\epsilon_j(\mathbf{k}) - \epsilon_i(\mathbf{k}) - \hbar\omega) / (3m^2\omega\Omega)$, and f is the Fermi-Dirac distribution. The matrix elements of the momentum operator are $p_{ji}^{\alpha} = \langle \psi_j | p^{\alpha} | \psi_i \rangle$. It is remarkable that this expression for the conductivity, which exactly coincides with the paper of Greenwood [50], does not require an explicit expression for

¹ This is devised for amorphous materials which are assumed to be isotropic, it is equally easy to implement this method for a particular direction to explore anisotropy of conduction.

² Since all such calculations depend upon excited states, it would be better to apply post DFT methods or at least hybrid functionals, a point we do not explore in this chapter.

the current density. By carefully deriving the current density \mathbf{j} , one discovers that this derivation, and also Greenwood's, veil significant approximations involving the DC limit, and more subtly, the spatial homogeneity of carrier density. We will not further dwell on these technical issues here, and adopt the "standard" KGF (Equation 2.1). See for example Equation 19 of reference [55] and associated discussion. For a full many-body picture see reference [56, 57].

The Kubo formula has been heavily employed in liquids [58, 59, 60, 61], amorphous semiconductors [62] and mixed systems [63, 64]. In its usual application, the KGF is applied to a static disordered lattice. As such, it provides no information about thermal disorder and its consequences to conduction. For applications of the KGF in disordered systems, the electron-phonon coupling is large for localized single-particle states [65, 66], especially those orbitals near the Fermi energy. In a room temperature thermal molecular dynamics simulation, energy levels may fluctuate with a thermally-induced root mean squared fluctuation $\sigma_E \gg kT$ [67, 68].

Above the Debye temperature, it is sensible to estimate the temperature-dependent conductivity by undertaking a long constant-temperature MD simulation and averaging the KGF over the trajectory. This appears to give reasonable results for the temperature dependence of pure and hydrogenated amorphous silicon, and explains the high temperature coefficient of resistance and functionality of doped *a*-Si:H as a material for night-vision device applications [69].

Apart from the approximations mentioned earlier, there are many technical details for properly using the KGF, including finite size effects and such details as the broadening of the δ function in Equation 2.1. A recent review details many issues about the use of KGF in hot condensed matter [70]. The KGF is a valuable tool, linking as it does transport experiments to the quantum mechanics of materials, but in its usual implementation gives

just one function (the AC conductivity) or one *number* (the DC conductivity). It provides no spatial information about the conduction.

2.3 Computing Spatial Information About Transport

For heterogeneous systems, a basic question is: “what parts of the network are conducting?” Some emerging computer memory technologies (resistive random access memory (RAM) and conducting bridge RAM) involve specific conduction pathways, and our microscopic understanding of such systems might be improved by a detailed atomistic understanding of the flow of charge through the systems. Conducting Bridge RAM can be made from many amorphous insulating hosts (such as GeSe_3 or Al_2O_3 , heavily doped with a transition metal like Ag or Cu). These are technologically important electrochemical devices for which basic questions arise about whether transport is simply through metal filaments or a more intricate process involving transport through metal rich regions [71]. We have provided direct insight into this elsewhere [72, 71, 73, 74, 75]. Another example of keen current interest is PUFs devices for computer security, made from amorphous silicon suboxide materials, as we discuss on more detail in Sec. 2.6.4. Another example of interest is conductance fluctuation in amorphous systems [76].

With this tool in hand, the idea might also be pushed in an “engineering direction” as a common inverse problems of materials science: “what is the structure that I need to have a particular conductivity?”, or “what is the structure required to have a particular absorption of light of frequency ω , eg. for the design of waveguides?” The inverse problem is always challenging: a robust tool of the form $\mathbf{R} \rightarrow \varphi$ (given coordinates what is the conducting path) is required before we can handle $\varphi \rightarrow \mathbf{R}$ (given the conducting path we seek, what coordinates – structure – will yield it?).

Some existing schemes yield insight into the spatial character of conduction. A principal message of the KGF is that the DC conductivity arises from transitions between

states at or near the Fermi level. To obtain a non-zero conductivity, it is necessary that the momentum matrix element not vanish between the relevant occupied and unoccupied states (Equation 2.1). If two such states ψ_i and ψ_j do not overlap, there is no contribution to the conductivity: transitions between spatially non-overlapping orbitals are forbidden. So, to the extent that there is a large overlap between the two states, there is likely to be a larger momentum matrix element too. This is the idea behind a primitive approximation, the “ $q_i - q_j$ ” method that we use in reference [73]. An even simpler scheme is to compute the charge density around the Fermi level [77] – it must be that the spatial conductivity involves those parts of space where this charge density is large, but this totally ignores the momentum matrix elements which lie at the heart of the KGF – these matrix elements are a legacy of the current-current correlation function, and it is not desirable to neglect these contributions. Other ideas related to spatial decomposition of conductivity have emerged in the literature before, including a computation of current densities for a randomly disordered system [78], using the methods of Baranger and Stone [79]. Also, within a Landauer picture, the concept of transmission eigen-channels was introduced and later implemented with non-equilibrium Green’s functions [80].

2.4 Theory

2.4.1 Spatially Projected Conductivity (SPC)

The KGF (Equation 1) gives the conductivity as a weighted sum of the modulus squared momentum matrix elements. The sums on Latin indices are over single-particle, for this paper, Kohn-Sham orbitals. The spatial dependence of the states is obviously important, but only insofar as this modulates the momentum matrix elements. Thus, it is desirable to rewrite the KGF expressing the matrix element quadratures as sums on a real space grid to find a spatial decomposition. Suppressing the explicit dependence of σ on \mathbf{k}

and ω , we write

$$\sigma = \sum_{ij\alpha} \int d^3x \int d^3x' g_{ij} [\psi_i^*(\mathbf{x}) p^\alpha \psi_j(\mathbf{x})] [\psi_i^*(\mathbf{x}') p^\alpha \psi_j(\mathbf{x}')]^* \quad (2.2)$$

Next, define complex-valued functions

$$\xi_{ij}^\alpha(\mathbf{x}) = \psi_i^*(\mathbf{x}) p^\alpha \psi_j(\mathbf{x}) \quad (2.3)$$

on a discrete real-space grid (call the grid points \mathbf{x}), and suppose, for simplicity, that the grid is uniformly spaced in three-dimensional space with spacing h . Approximating the integrals as sums on the grid, and obtaining the operation of p^α from centered finite-differences, we easily arrive at:

$$\sigma \approx h^6 \sum_{\mathbf{x}, \mathbf{x}'} \sum_{ij\alpha} g_{ij} \xi_{ij}^\alpha(\mathbf{x}) [\xi_{ij}^\alpha(\mathbf{x}')]^* \quad (2.4)$$

We find it useful to introduce what we will call the *conduction matrix* Γ defined as:

$$\Gamma(\mathbf{x}, \mathbf{x}') = h^6 \sum_{ij\alpha} g_{ij} \xi_{ij}^\alpha(\mathbf{x}) [\xi_{ij}^\alpha(\mathbf{x}')]^* \quad (2.5)$$

Γ is Hermitian and positive semidefinite. Note that Γ has the dimension of conductivity, and we have summed out the Kohn-Sham orbitals, leaving only spatial dependence. It follows from Equation 2.4 that $\sigma = \sum_{\mathbf{x}, \mathbf{x}'} \Gamma(\mathbf{x}, \mathbf{x}')$ as $h \rightarrow 0$. We then define SPC as:

$$\zeta(\mathbf{x}) = \left| \sum_{\mathbf{x}'} \Gamma(\mathbf{x}, \mathbf{x}') \right| \quad (2.6)$$

To obtain a real value for the scalar field ζ , the modulus operation is required: while the full double sum is of course real, summing only one index of Γ yields a function that is, in general, complex. $\zeta(\mathbf{x})$ is of interest as it is positive, and by construction indicates the conduction-active parts of the system.³

³ Similar forms are possible for the SPC. If, for example only one of the matrix elements is computed on a grid, then if $\phi_{ij} = h^3 g_{ij} p_{ij}^\alpha$, then for $\tau(\mathbf{x}) = \sum_{ij\alpha} \phi_{ij} \xi_{ij}^\alpha(\mathbf{x})$, $|\tau|$ also serves as an estimate for SPC, identical to ζ as $h \rightarrow 0$.

2.4.2 Spectral Properties of the Conduction Matrix

The eigenvalue problem for Γ reads: $\Gamma|\chi_\mu\rangle = \Lambda_\mu|\chi_\mu\rangle$, for which $\mu = 1, n_g$. n_g is the number of points in the spatial grid (thus for example, $n_g = n^3$ for n points in each Cartesian direction in 3D). Diagonalization provides a spectral representation:

$\hat{\Gamma} = \sum_\mu |\chi_\mu\rangle\Lambda_\mu\langle\chi_\mu|$, from which:

$$\sigma = \sum_\mu \Lambda_\mu \left[1 + \sum_{\mathbf{x}, \mathbf{x}', \mathbf{x} \neq \mathbf{x}'} \chi_\mu(\mathbf{x})\chi_\mu^*(\mathbf{x}') \right], \quad (2.7)$$

Equation 2.7 introduces the concept of conduction eigenvalues and modes. The spectral decomposition of σ of Equation 2.7 categorizes the conductivity into a finite and, in practice, small (compared to the dimension of Γ) set of conduction channels. Because of trace invariance of Γ , $\sum_\mu \Lambda_\mu = \sum_{\mathbf{x}} \Delta(\mathbf{x})$, for $\Delta(\mathbf{x}) = \Gamma(\mathbf{x}, \mathbf{x})$. The ‘‘spectral form’’ for the SPC is thus:

$$\zeta_s(\mathbf{x}) = \left| \sum_\mu \Lambda_\mu \left\{ |\chi_\mu(\mathbf{x})|^2 + \sum_{\mathbf{x}', \mathbf{x}' \neq \mathbf{x}} \chi_\mu(\mathbf{x})\chi_\mu^*(\mathbf{x}') \right\} \right|, \quad (2.8)$$

and $\zeta(\mathbf{x}) = \zeta_s(\mathbf{x})$.⁴

It is of interest to determine the value of an approximate ζ_s (eg. computed from only a handful of the eigenvectors conjugate to the largest eigenvalues) to ζ . We discuss the density of states of Γ below. For complex mixed conducting/insulating phases, we find that the eigenvectors χ conjugate to extremal eigenvalues produce a remarkably compact and efficient description of the conduction, often reproducing the full ζ with only a few tens of eigenvectors, even though $\dim(\Gamma)$ is in the tens of thousands. For a metal (e.g., FCC Al), we again find a great accumulation of eigenvalues at $\Lambda = 0$ but with a significant spectral tail unseen in less metallic systems. Thus, the high conductivity of a metal

⁴ If we took a ‘‘diagonal approximation’’ $\Delta(\mathbf{x})$, by omitting the second term on the RHS in Equation 2.7, the eigenvalue Λ_μ would exactly give the conductance through channel μ . In such an approximation, $\sigma \sim \sum_\mu \Lambda_\mu = \text{Tr}(\Gamma)$, a form reminiscent of the transmission eigenchannels [80], but notice that our full expression for σ is *not just a trace* over Γ in contrast with the transmission matrix appearing in the Landauer expression for conductance.

accrues from integrating over this tail. The density of states of Γ is yet another way to distinguish insulators, semiconductors and metals.

So far, we have computed the eigenvectors of Γ by exact diagonalization. However, it is clear that this problem is ideal for a Lanczos technique [81]. A maximum entropy reconstruction of the density of states of Γ is also under investigation [82].

2.5 Computational Details

2.5.1 Models

We used Vienna Ab initio Simulation Package (VASP) [83] code to carry out DFT calculations. The generalized gradient approximation (GGA) of Perdew-Burke-Ernzerhof (PBE) [84] was used as the exchange-correlation functional. Brillouin zone sampling was restricted to the gamma point ($\mathbf{k} = 0$), and periodic boundary conditions were used throughout.

A model of low density amorphous carbon (a-C) was examined with density 1.5 g/cm³ and consisted of 216 atoms [85].

An amorphous silicon (a-Si) model with 216 atoms ($\rho = 2.33$ g/cm³) was taken from reference [86] and was relaxed using a conjugate gradient method. While relatively small by current standards, this model is an excellent representation of the topology of a-Si, and is 100% 4-fold, though some of the sites are strained. The a-Si model was then annealed at 2000 K for 6 ps to create representative snapshots for liquid Si (l-Si).

We modeled a-Si suboxide (a-SiO_{1.3}) in cells with 184 atoms and density 1.68 g/cm³ [87] that was obtained using a melt-quench scheme [88]. We began with a supercell with a random initial configuration at the experimental density and desired stoichiometry, which was then heated above melting point. The supercell was then cooled to room temperature in successive steps. The final model was obtained by performing a relaxation to minimize the forces acting on each atom to below ≈ 0.005 eV/Å.

A cubic model of crystalline FCC Al (*c*-Al) with 500 atoms was constructed.

We use various values of grid spacing (h) throughout this chapter. We find that the SPC is fairly insensitive to h , and have checked the results presented here by considering a few different choices for h and verifying that the predicted SPCs were consistent.

2.5.2 Methods

To carry out the calculations, we employed Kohn-Sham orbitals computed with VASP [89]. The ξ (of Equation 2.4) was obtained using finite central differences with $\delta r = 0.05 \text{ \AA}$. To estimate the SPC (ζ), we adopted a discrete grid with variable dimensions depending upon the supercell employed. We selected a temperature of $T = 1000 \text{ K}$ for the Fermi-Dirac distribution and approximated the delta function in g_{ij} by a Gaussian distribution with width 0.05 eV . The numerical value of the conductivity is sensitive to these choices, the SPC plots far less so.

The extent of the localization of eigenvectors were quantitatively gauged by calculating the IPR.

$$\mathcal{I}_\mu = \frac{\sum_x (\chi_\mu(x))^4}{\left(\sum_x (\chi_\mu(x))^2\right)^2} \quad (2.9)$$

The value of \mathcal{I} lies between 0 and 1. Higher \mathcal{I}_μ signifies that the eigenvector χ_μ is more spatially localized.

2.6 Results and Discussion

2.6.1 Low Density Amorphous Carbon (a-C)

Carbon materials have produced two Nobel prizes in the last quarter century. a-C has applications including protective coatings, radiation protection, electronic circuits and bio-medical [90, 91, 92]. Carbon-based electronics is a major field of research in materials science [93, 94, 95, 96]. Carbon in different forms such as carbon nano tubes (CNTs) are

being studied for PUF applications [97]. Carbon-based electrodes are used as electrochemical sensors for biological applications [98].

Amorphous carbon (a-C) at low densities ($<2 \text{ g/cm}^3$) consists primarily of sp^2 sites, with some sp and sp^3 sites. Bhattarai *et al.* have shown that a-C at low densities ($\rho = 0.92\text{-}1.6 \text{ g/cm}^3$) exhibits sp^2 configurations with $\approx 66\text{-}81\%$, sp chains with $\approx 14\text{-}33\%$ and sp^3 configurations with $\approx 0\text{-}9\%$ [85]. The presence of sp^2 and sp configurations may render the materials electrically conductive and optically absorbing. Intuitively, it is clear that the connectivity between the sp , sp^2 and sp^3 subnetworks might also play a role in conduction. For densities below 1 g/cm^3 , it has been shown that the material consisting of warped and wrapped regions of amorphous Graphene, with considerable ring disorder [99].

In this sub-section, we discuss SPC in low density a-C (1.5 g/cm^3) and also provide spectral information from the conduction matrix by diagonalizing it. We discretized the supercell into $40 \times 40 \times 40$ grid points ($h = 0.355 \text{ \AA}$) and obtained the conduction matrix $\Gamma(\mathbf{x}, \mathbf{x}')$ which has dimension of 64000. The conductivity path was obtained by calculating space projected conductivity at each grid point as discussed in earlier section (Section. 2.4.1). The SPC is projected as an isosurface (yellow blob) in left plot of Figure 2.1. As a technical exercise, we also compare the results to the diagonal approximation $\Delta(\mathbf{x})$. The isosurface in the left plot shows that SPC is due to both sp and sp^2 configurations in the network. It reveals active participation of sp chains in the network that form a clear connected conducting path and follow sp^2 configurations to a pentagonal ring. Pentagonal and the hexagonal ring structures that are connected with sp chains form the other active sites for conduction. These rings are highlighted in the middle plot of Figure 2.1 that show only those atoms contributing significantly to conduction. The arrows indicate the continuous conduction path along the C atoms displayed in the left plot. Very few sp^3 configurations appear as SPC sites. As a consequence, they do not

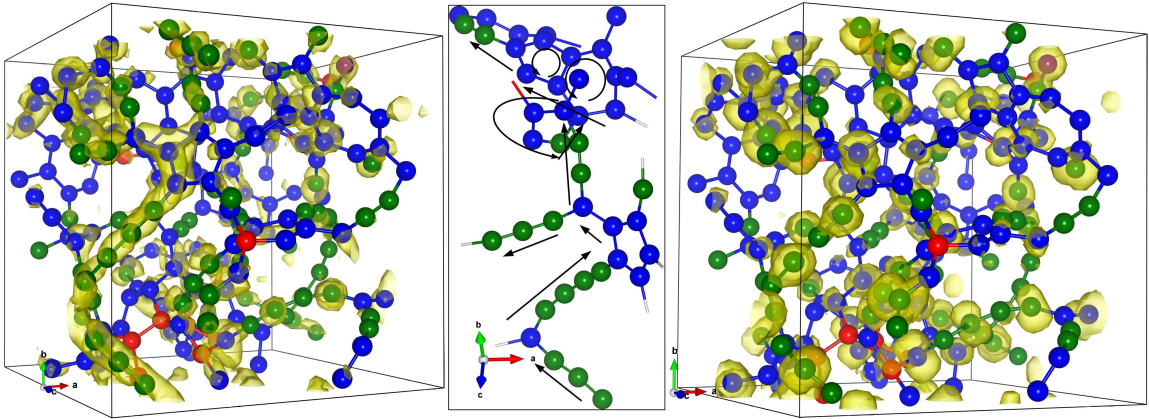


Figure 2.1: a-C: Left and right correspond to the SPC (ζ) and the diagonal approximation $\Delta(\mathbf{x})$ projected on grids as an isosurface plot (yellow blobs) respectively. The middle plot corresponds to the structural topology of the network in one region of the supercell that forms a continuous conduction path. The straight and the curved lines with arrowhead are guides to the eye to indicate the conduction path. The colored spheres represent C atoms with different configurations; Red (sp^3), blue (sp^2), green (sp) and purple (singly bonded).

contribute to charge transport, as expected. In order to provide a simpler picture of the conduction, we projected $\Delta(\mathbf{x})$, the diagonal approximation of ζ , as an isosurface in the right plot of Figure 2.1. Δ is primarily centered on the atomic sites and shows discrete path. The isosurface blobs show that Δ picks almost the same sites that are active in ζ . So, Δ qualitatively provides a similar picture of the conduction path as ζ displayed in left plot of Figure 2.1 for a-C.

Next we discuss the spectral properties of conduction matrix, $\Gamma(\mathbf{x}, \mathbf{x}')$, for a-C by diagonalizing it as discussed above (Section 2.4.2). The density of states (DOS) from the eigenvalues and the extent of the localization of the eigenvectors measured by IPR (\mathcal{I}) were calculated and are displayed in Figure 2.2.

The DOS in Figure 2.2 reveals an overwhelming fraction of eigenvalues very near $\Lambda = 0$. These states are mostly localized as represented by the values of \mathcal{I} shown by the scattered red dots. We find a few eigenvalues significantly shifted from $\Lambda = 0$ in the spectrum; only eigenvectors corresponding to these extreme eigenvalues are important to

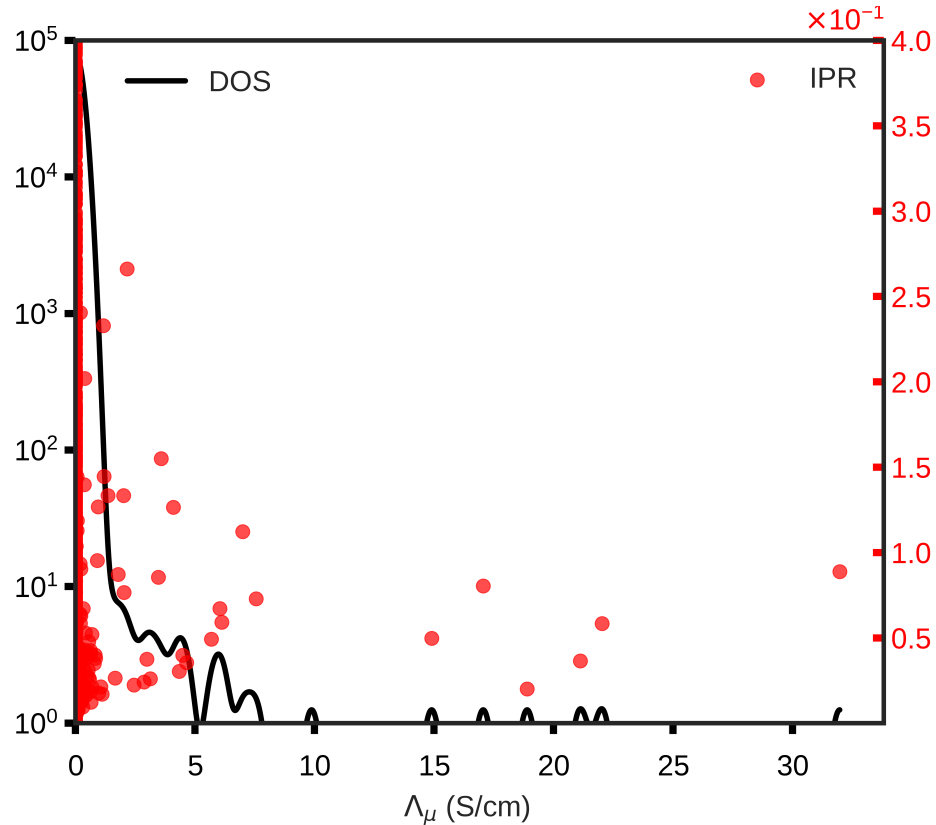


Figure 2.2: a-C: Logarithmic spectral density of states of Γ -matrix. The left scale represents the DOS of the eigenvalues displayed in a log scale (solid black line) and the right scale corresponds to the extent of localization of eigenvectors measured as IPR (\mathcal{I}) (red circles). Large \mathcal{I} implies a spatially localized eigenvector of Γ .

the DC conductivity. To better have an estimate of the number of such eigenvectors, we calculated the spectral form of SPC, (ζ_s) , defined in Equation 2.8, from the largest 75 and 100 eigenvectors, and these are displayed in Figure 2.3. Both isosurface plots in Figure 2.3 show almost the same path as ζ that is displayed in left plot of Figure 2.1. This shows that 75-100 eigenvectors suffice to obtain the conduction path in a-C.

To see how a few eigenvectors conjugate to the largest eigenvalues contribute to transport see Figure 2.4. We see that from $\Lambda_\mu |\chi_\mu|^2$, these extremal eigenvectors either form a short channel or lie within spatially separated parts of the network. The eigenvector corresponding to the second largest eigenvalue (left plot in Figure 2.4) picks out mostly

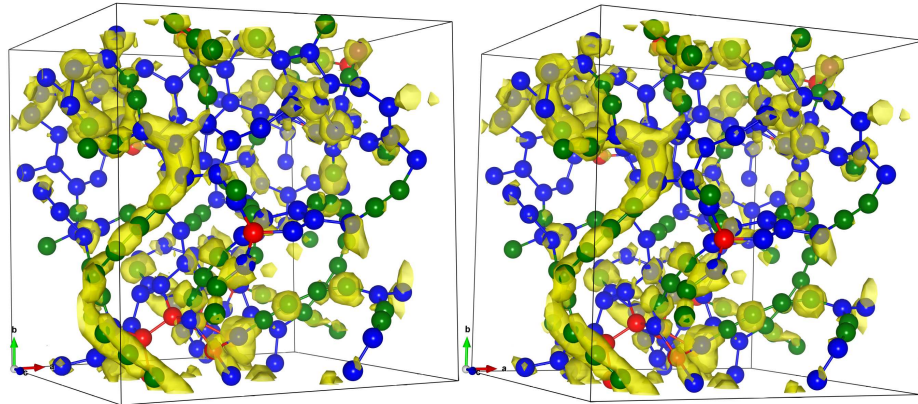


Figure 2.3: a-C: Spectral form for SPC (ζ_s) projected on grids as an isosurface plot (yellow blobs). Left and right plots correspond to the ζ_s from the sum of last 75 and 100 eigenvectors respectively. Same cutoff for the isosurface has been used in both plots and the left plot in Figure 2.1. Same color code is used to describe atoms as in Figure 2.1. ζ_s from extreme 75-100 eigenvectors is equivalent to ζ and is sufficient to essentially exactly determine the SPC in a-C.

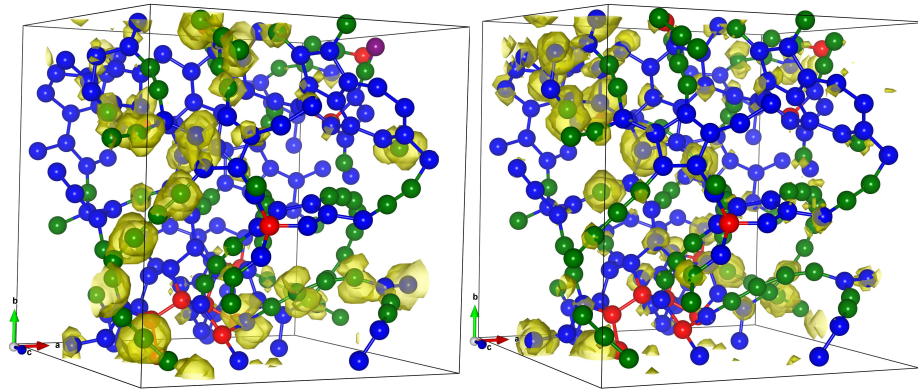


Figure 2.4: a-C: Eigenvectors projected on grids as an isosurface plot (yellow blobs). Left and right plots correspond to the second largest ($\Lambda_\mu = 22.04$ S/cm) and the largest ($\Lambda_\mu = 31.98$ S/cm) eigenvalues respectively (ref Figure 2.2). Same color code is used to describe atoms as in Figure 2.1.

the sp sites. The sp^2 configurations which are adjacent to the sp configurations are other active sites for this eigenvalue. The extremal eigenvector selects both sp^2 and sp sites.

Both eigenvectors pick more or less the same sp^2 sites in the network that are the active sites for the conduction as shown by ζ displayed in left plot of Figure 2.1.

The physical conclusion is that sp chains play an important role in electronic transport in phases of carbon that possess them. The SPC that emerges reveals charge transport through interconnected sp -chains and sp^2 rings. It is expected that the relative fraction of these conducting constituents is strongly density, impurity and sample preparation dependent.

2.6.2 Amorphous Silicon

Amorphous silicon (a-Si) plays an important role in technological applications, such as thin-film transistors, photovoltaics, infrared imaging devices, and active-matrix displays [100]. Being an electronic material, understanding the conduction mechanisms is of obvious importance. In this sub-section, we discuss the conduction-active sites in the material and also discuss the spectral properties of the conduction matrix Γ . The supercell was partitioned into $42 \times 42 \times 42$ grid points ($h = 0.39 \text{ \AA}$) and the Γ -matrix was obtained. The SPC at each grid was then calculated and is displayed as a heat map plot in Figure 2.5.

Earlier works on the electronic bandtails (Urbach tails) of a-Si have shown that the valence tail states are built from chains or clusters of Si atoms with bonds shorter than average and conduction tail states are due to chains of Si atoms with longer bonds [101, 102, 103, 104]. It is therefore to be expected that these tail states (and gap states due to badly strained fourfold sites or coordination defects) will play a role in conduction.

Figure 2.5 displays the SPC for a-Si. Analysis of the SPC shows special weight for atoms with bonds shorter than 2.32 \AA , and longer than 2.43 \AA (the average bond length is about 2.35 \AA). The heat map shows that the SPC also sits at strain defects (4-fold atoms with large variation in bond angles or bond lengths from tetrahedral symmetry). The

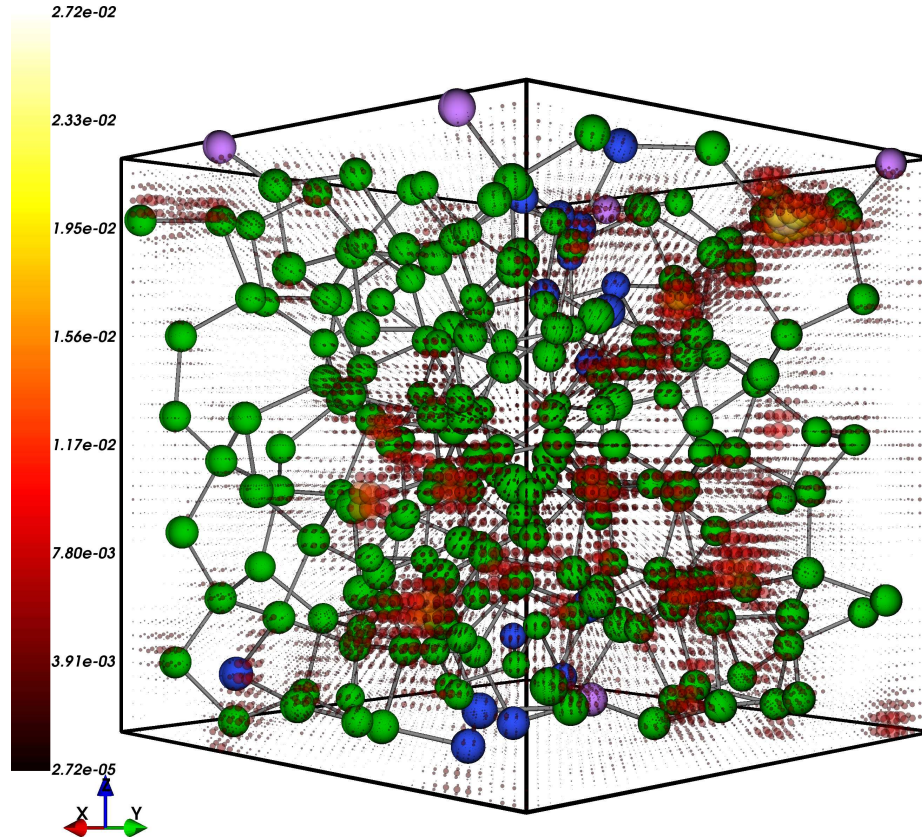


Figure 2.5: a-Si: SPC (ζ) projected on grids as heat map plot (labeled by colorbars on left of the plot) scaled with maximum value in each plot. The size of the hot spheres is scaled with the magnitude of the SPC value. The colored spheres represent Si atoms with different bonding environment; The blue and heliotrope colored spheres represent 4-fold coordinated Si atoms with one and two very long Si-Si bonds respectively. The green colored spheres represent typical Si atoms with “normal” bond lengths. The bond cutoff distance of 2.72 Å was chosen.

conduction involves all the states near the Fermi level (ϵ_F), thus involving tail states (of long and short bond structures) and of course defect states near ϵ_F . We diagonalized Γ to understand the spectral information of the conduction eigenvalues and the eigenvectors. The DOS of the eigenvalues and the extent of localization (\mathcal{I}) of the eigenvectors were calculated and are displayed in Figure 2.6.

Figure 2.6 shows a very large accumulation of eigenvalues near $\Lambda = 0$. Much about the transport can be obtained from only a few extremal eigenvalues and conjugate

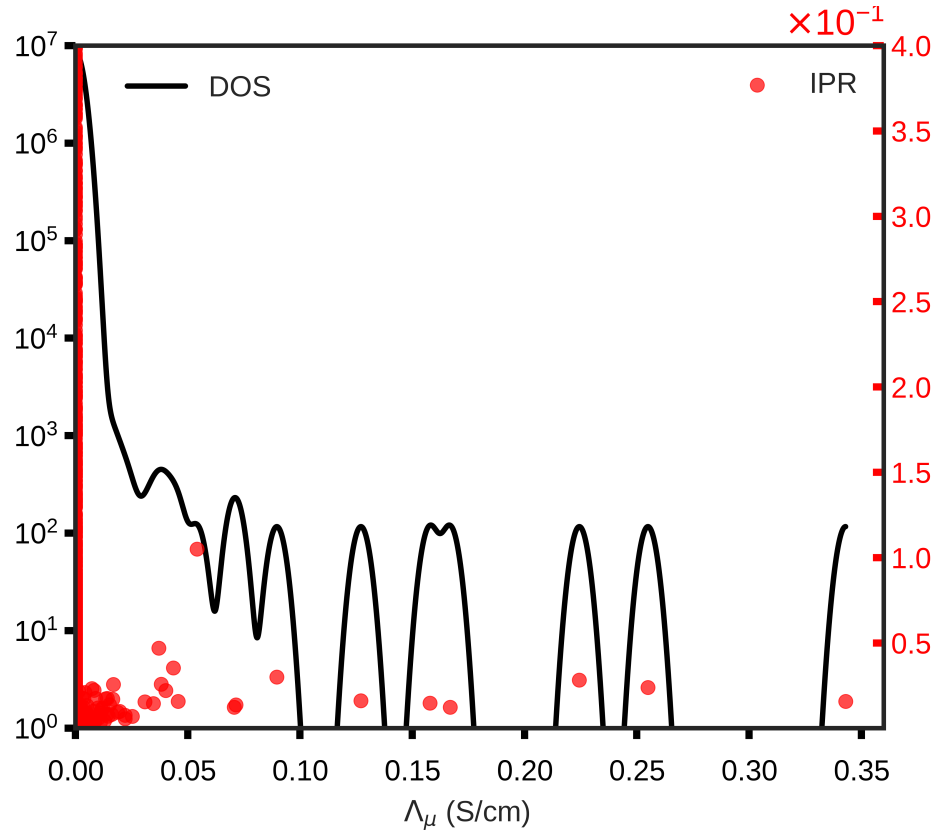


Figure 2.6: a-Si: Logarithmic spectral density of states of Γ -matrix. The left scale corresponds to density of states (DOS) of the eigenvalues displayed in a log scale (solid black line) and the right scale corresponds to the extent of localization measured as IPR (\mathcal{I}) (red circles).

eigenvectors of Γ to approximate the SPC of the material. We plot $|\chi|^2$ for the largest two eigenvalues in Figure 2.7. We find that these eigenvectors select out specific sites in the network. The eigenvector corresponding to the second largest eigenvalue (left plot in Figure 2.7) picks the atomic sites with short-bonded Si atoms with maximum bond length of 2.32 Å. The eigenvector corresponding to the largest eigenvalue picks entirely different parts of the network. This eigenvector follows a path among those atoms that form adjacent strain defect sites [105], nominally 4-fold but with one or two long bonds shown in blue and heliotrope respectively), and also involves filaments of slightly long Si-Si bonds with minimum bond length of 2.43 Å. This calculation reinforces the predicted

short-bond (long-bond) association with valence (conduction) tails, and shows an interesting “conduction mixing” of the defects and tail structures (long and short bond subnetworks). In a system with dangling (3-fold) or floating (5-fold) configurations, yielding states near ϵ_F , we would expect these sites to also participate in the resulting $\zeta(\mathbf{x})$.

The defect-rich phases including dangling and floating bonds (as well as nominally 4-fold structures “strain defects”) are present in a-Si and it is important to explore the role of defects in conduction. There is no doubt that such defects will play a role, as their electronic energies are well known to be in the gap, and for dangling bonds especially, near the middle of the gap. We speculate that there may be interesting SPC linkages between such defects and the filamentary structures associated with the Urbach tails [102], perhaps reminiscent of the sp-ring “mixing” of a-C. Conductivity will certainly depend on delocalization that accrues from mixing/banding between defect state: such effects are included in our computations.

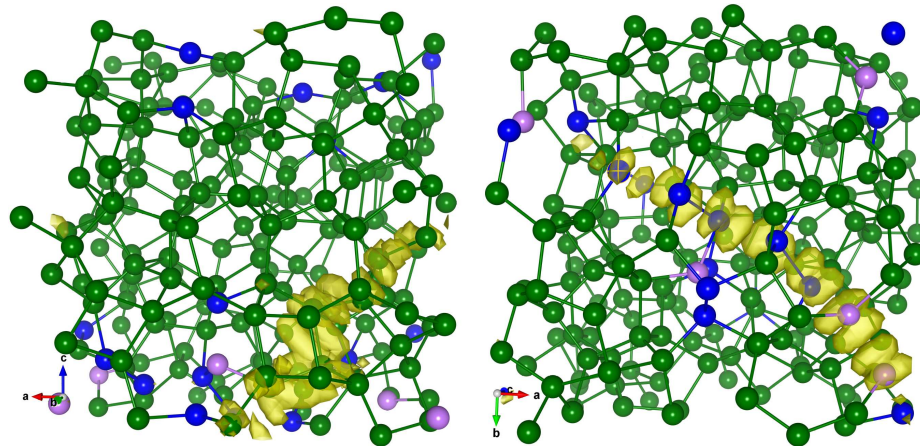


Figure 2.7: a-Si: Eigenvectors projected on grids as an isosurface plot (yellow blobs). Left and right plots correspond to the second largest ($\Lambda_\mu = 0.26$ S/cm) and the largest ($\Lambda_\mu = 0.34$ S/cm) eigenvalues respectively. For atoms, the color code is same as used in Figure 2.5. Since the atoms picked by the eigenvectors that are adjacent to each other are separated by the periodic box, we shifted the coordinates to make these atoms include in the same side of the box to make the connectivity clear. The left panel emphasizes short bonds, right panel long bonds and defects.

2.6.3 Conductivity Fluctuations in Liquid Silicon

Liquid silicon (l-Si) is a metal in contrast to a-Si or c-Si which are tetrahedral semiconductors. Although it is metallic, the first neighbor atomic coordination number is between 5-6 [106], hinting at a prevalence of covalent bonds in the liquid state of Si and differentiating it from other metals in terms of structural topology [107]. In the liquid state, thermal fluctuations cause the structure to continuously change and so too the SPC in the network. To model the liquid metal, we annealed the a-Si model at 2000 K for 6 ps. The thermal fluctuations induce fluctuations in the Fermi-level (ϵ_F) and also the electronic gap associated with it. The fluctuation of the frontier of highest occupied molecular orbital (HOMO), lowest unoccupied molecular orbital (LUMO) and the Fermi-level with simulation time is provided in Figure 2.8 for a brief time interval.

From Figure 2.8, we see that the minute gamma-point gap opens and closes with time due to the thermal fluctuations. We chose four configurations as shown by different markers in the inset plot of Figure 2.8 where such feature exists. For these snapshots, we find that the coordination environment does not drastically change within the network for this short time interval. A majority of the Si atoms are 5-fold and 6-fold coordinated ($\approx 56-57\%$); 4-fold and 7-fold coordinated Si atoms account for $\approx 33-35\%$ of the total coordination. 8-fold coordinated Si atoms account for 5.1% - 9.7% of the network. For each of these configurations, we obtained the SPC on a $40 \times 40 \times 40$ grids ($h = 0.41 \text{ \AA}$) and these are displayed as heat-map plots in Figure 2.9.

The heat-map plot of SPC shows that the fluctuation in the energy levels results in slight variation in the SPC. For all models, we find that the SPC is quite extended indicating the metallic character of the material. All coordinations seem involved in the conduction, suggesting a truly delocalized metallic form of conduction. We also picked four temporally separated snapshots at simulation times 1.95, 3.15, 4.35 and 5.55 ps to capture the variation of the conduction path on longer time scales. The SPC for each of

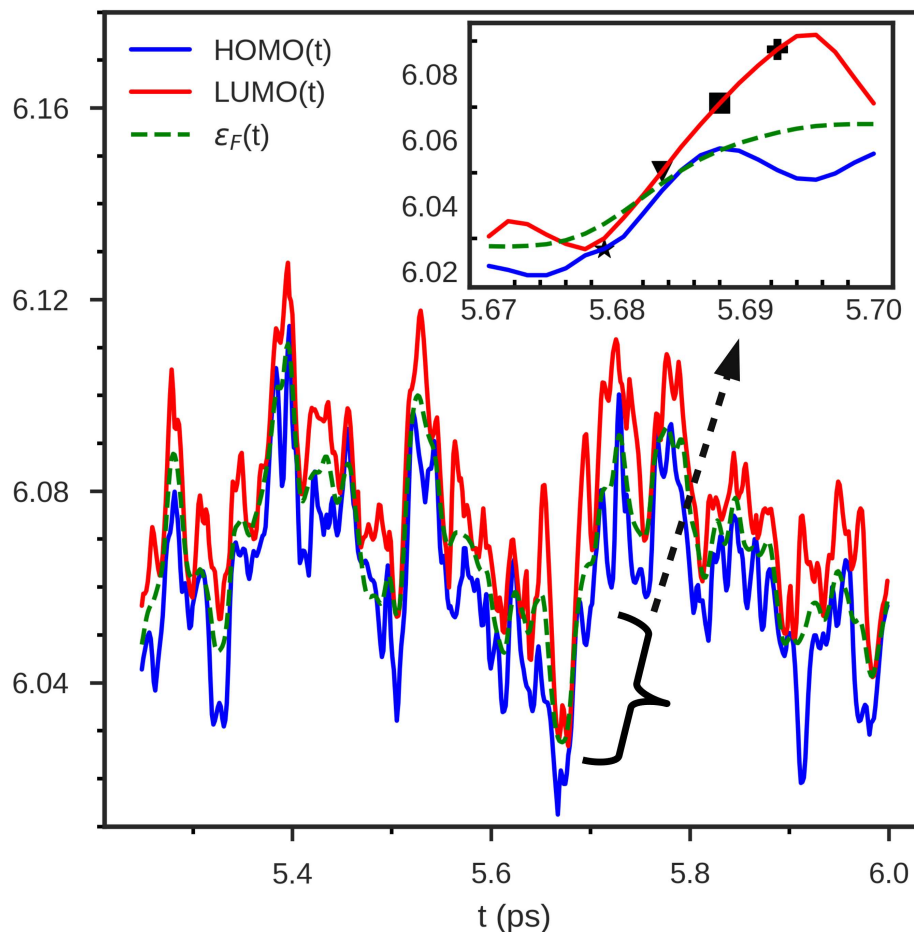


Figure 2.8: 1-Si: A snapshot showing fluctuations of energy levels near the Fermi-level (units in eV) plotted against simulation time. The inset plot shows a specific region (shown by the curly brace) with closing and opening of the electronic gap. The markers correspond to the time step for the atomic configurations that were selected for the SPC calculations.

these snapshots is displayed on grids as a heat map in Figure 2.10. The dominating regions appear in different parts of the cell for these snapshots, an expected kind of “local conductance fluctuation” as the Si atoms diffuse in the liquid state and continuously change their local bonding and thus local electronic structure. The variation in the conduction path is displayed, and colored spheres in each plot of Figure 2.10 indicate the fluctuation in the local atomic environments. We find that, within the top 6% of SPC values in Figure 2.10(a), one of the conduction paths is along the chain with 4-fold, 5-fold,

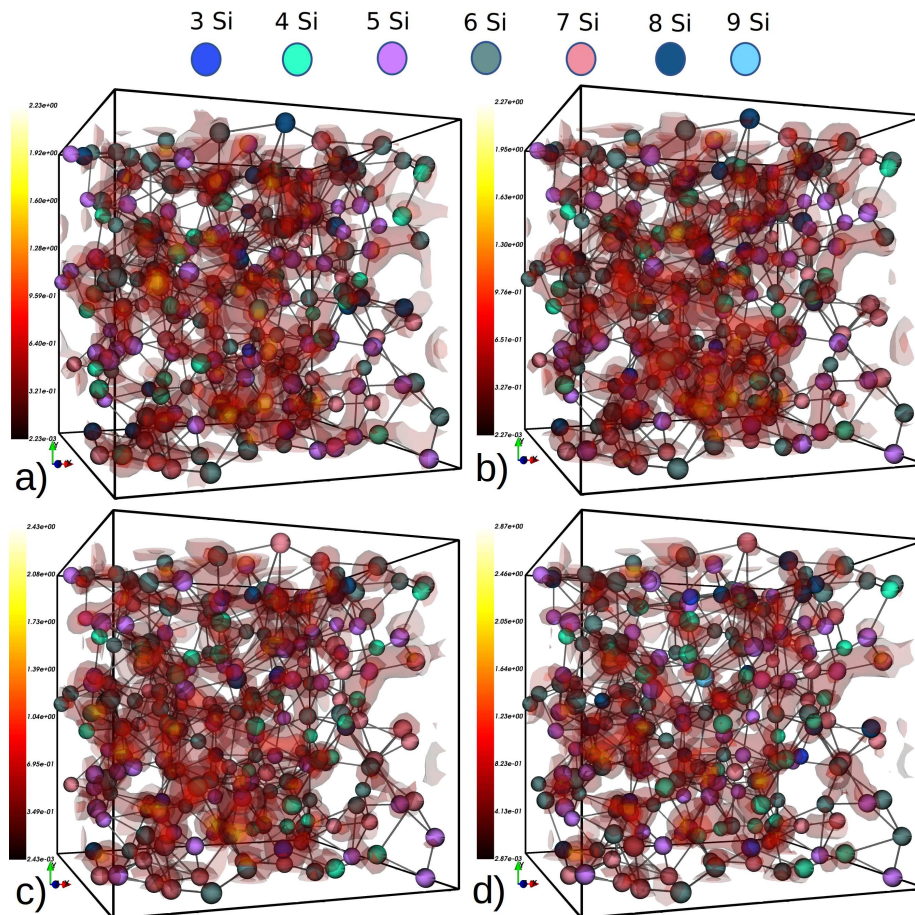


Figure 2.9: 1-Si: SPC (ζ) projected on grids as a heat map (labeled by colorbars on left of each subplots) for atomic configurations at that are temporally close to each other shown by the marker signs in the inset plot of Figure 2.8. a), b), c) and d) correspond to the atomic configurations shown by star, triangle, square and the plus signs in the inset plots of Figure 2.8 respectively. Atom color represent Si with different instantaneous coordination as labeled as shown at the top of the figure. The cutoff distance of 3.10 \AA is used to define the coordination.

6-fold, 7-fold coordinated Si atoms in the middle region of the network. Similarly, in Figure 2.10(b), we find a continuous path along 4-fold, 5-fold, 6-fold, 7-fold, 8-fold Si atoms where four of such 6-fold coordinated atoms contributing to the path. In Figure 2.10(c), there exists a conduction path along a chain of five Si atoms that are all 6-fold coordinated. We also find the conduction path along the chain of 4-fold, 5-fold,

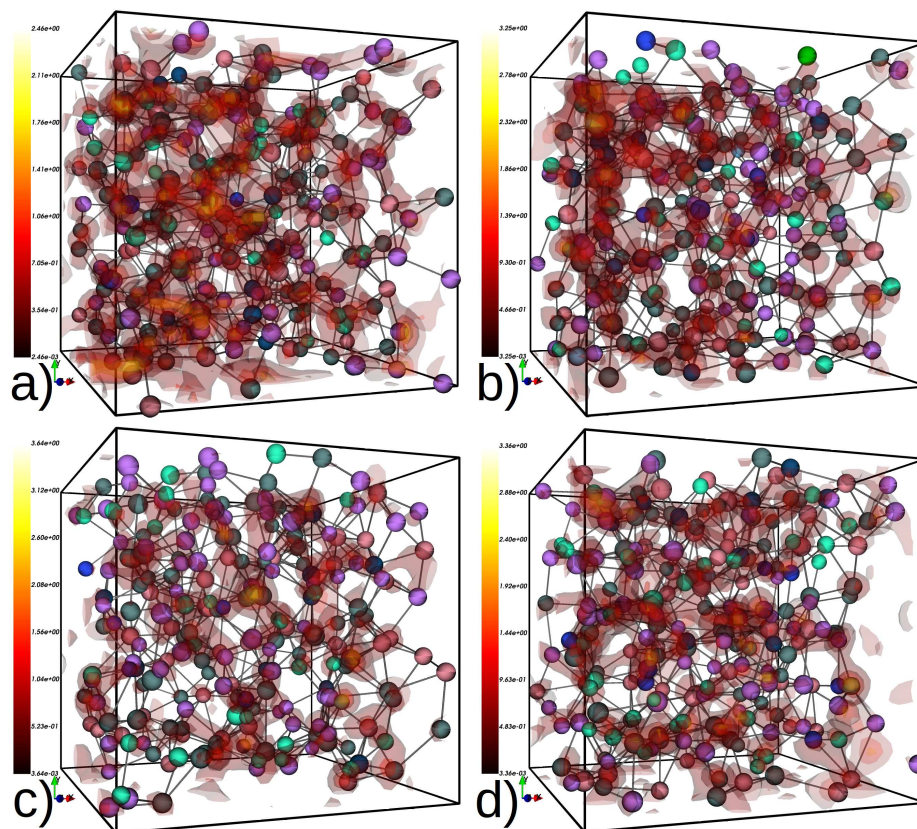


Figure 2.10: 1-Si: SPC (ζ) projected on grids as a heat map plot (labeled by colorbars on left of each subplots) for configurations at intervals of 1.2 ps. a), b), c) and d) correspond to the SPC plot at simulation time 1.95, 3.15, 4.35 and 5.55 ps respectively. Atoms color represent Si with different coordination environment and we adopt the same convention as in Figure. 2.9. The cutoff distance of 3.10 Å is used to define the coordination. Note the spatial fluctuation in the heat maps over these snapshots.

6-fold coordinated Si atoms where three of such 5-fold coordinated Si exist in the chain.

In Figure 2.10(d), we find one of the conduction paths along six Si atoms with 5-fold, 6-fold, 7-fold, 8-fold coordinated Si atoms forming a chain where three of them are 5-fold coordinated. So, the SPC calculations from these snapshots show that the most conduction-active sites in 1-Si are 5-fold and 6-fold coordinated. We also find Si atoms with 4-fold, 7-fold and 8-fold coordinated forming the other sites of conduction. It would

be of interest to properly analyze these fluctuations with suitable space-time correlation functions.

2.6.4 Amorphous Silicon Suboxide: Application for Finite ω

Optical materials are critically important, and there is always a demand for novel optically functional and transparent materials. Electromagnetic waves of different frequencies may be absorbed by different parts of the inhomogeneous material. Having *a priori* information on the absorption-active sites/regions in the material could be helpful to engineers, for example, to design wave-guides or other optical devices. Optical PUFs are an ongoing research topic for computer security applications [108].

Silicon suboxides, $a\text{-SiO}_x$ ($0 < x < 2$), have complex structures and two different pictures of suboxide structure are mainly discussed: “random mixture” [109] and “random bonding” [110]. The former model suggests the segregation of Si in silica separated by the interfacial boundary and the latter model suggests a continuous random network of tetrahedral units of $\text{SiSi}_y\text{O}_{4-y}$ where $y = 0$ to 4. The complexity of the network makes the material electronically interesting and of course span amorphous silicon to amorphous silica.

If one imagines starting in $a\text{-SiO}_2$, a superb insulator, one can imagine a process of randomly depleting O atoms from the network. If x is close to 2, O-vacancies will be widely separated with little conduction. As O depletion proceeds, more and more hopping will accrue and the conduction paths will be determined by the locations and electronic structure associated with the O-vacancy sub-network. The electrical conductivity therefore has a stochastic character depending on the existence and details of a hopping pathway involving the vacancies.

In this chapter we look very briefly at an “AC version” of this, and show that light absorption is very sensitive to wavelength, and in particular, show that different “vacancy

subnetworks” contribute to the absorption. This suggests that an “optical PUF” might be possible for the silicon suboxide materials. We limit the discussion to a qualitative indication of how different parts of the network participate for two different wavelengths, and we note for completeness that to really carry out such calculations realistically better excited states should be computed with more intricate methods.

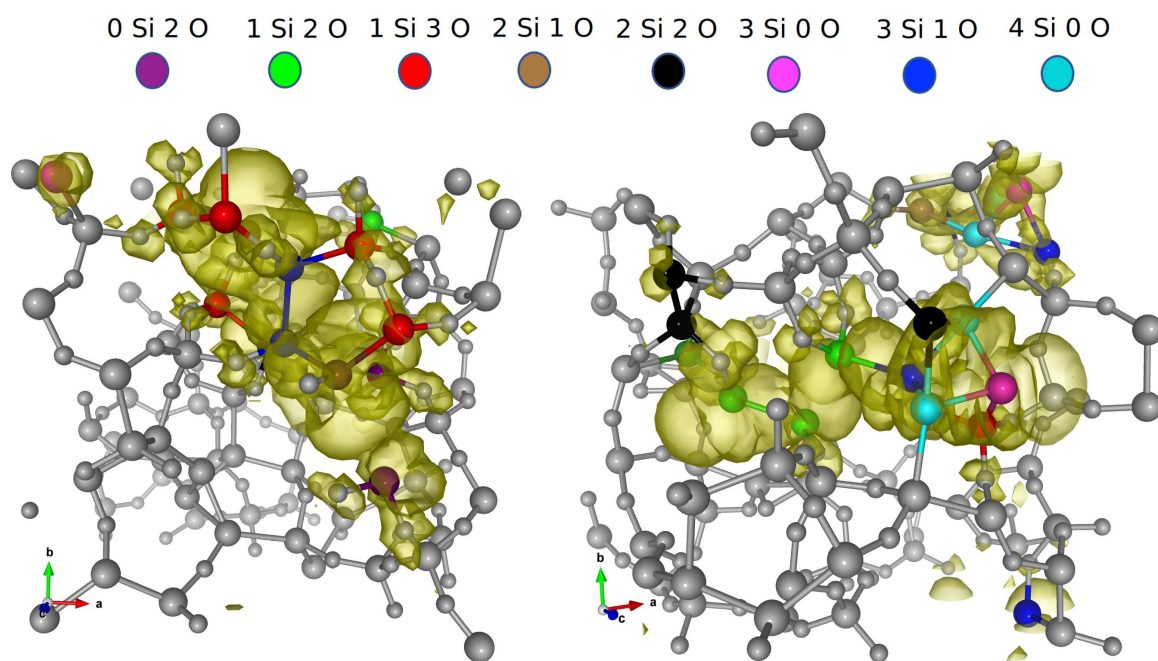


Figure 2.11: a-SiO_{1.3}: SPC (ζ) projected on grids as isosurface (yellow blobs) plots. Left and right plots correspond to $\hbar\omega = 0.62$ eV and 0.76 eV respectively. Multicolored spheres refer to Si atoms within the conduction-active region having different coordination environment shown as legends at the top of the figure. Top 3.7% SPC values are included in both plots. The gray colored spheres represent Si and O atoms that lie outside the conduction active region for the given cutoff. The small size spheres represent O atoms.

In this subsection, we discuss light absorption in a-SiO_{1.3} at two frequencies. To enable this, we calculated the space projected conductivity on $40 \times 40 \times 40$ grids ($h = 0.39$ Å) for two different wavelengths with $\lambda = 2000$ nm and $\lambda = 1600$ nm. The SPC for both cases are displayed in Figure 2.11. It is of interest that the absorbing parts of the models are *qualitatively* different, and more to the point, the computation predicts *which*

parts of the matrix will absorb light of a specified wavelength. The isosurface plots in Figure 2.11 show that the absorption meanders along adjacent O-vacancy sites in the network since different frequencies pick out different paths φ in the network. As such, changing the frequency and changing the path makes it likely that external observables such as absorption, will also change, making the system potentially attractive for PUF applications.

2.6.5 FCC Aluminum

So far we have discussed conduction in non-crystalline semiconductor materials. In this sub-section, we consider FCC aluminum (c-Al), a metal, with a focus on the spectral properties of the conduction matrix Γ . $\Gamma(\mathbf{x}, \mathbf{x}')$ for the 500 atoms Al cell was obtained on a $42 \times 42 \times 42$ grids ($h = 0.48 \text{ \AA}$) so that $\dim(\Gamma) = 74088$. Γ was exactly diagonalized to obtain eigenvalues (Λ_μ) and the eigenvectors (χ_μ).

Figure 2.12 shows the density of the states (DOS) of the conduction eigenvalues and the extent of the localization of the conjugate eigenvectors (J). The DOS in Figure 2.12 shows that a majority of the eigenvalues lie near $\Lambda = 0$. This is clear from the inset that shows the evolution of the conduction eigenvalues in increasing magnitude where only the last 24088 among 74088 eigenvalues have magnitude greater than 10^{-9} S/cm. Even in a metal, most eigenvalues of Γ are effectively zero. In contrast with our previous examples, the spectrum shows the presence of an extended tail in the DOS that reveals a signature of metallic conduction in Al. This is supported by the inset plot where the eigenvalue increases in a linear fashion at different regimes. The inset also provides a tentative picture of the transition from an insulating to conducting spectral character near the high- Λ end of the spectrum between indices 60000-67000. Beyond index 67000, we observe that the density of eigenvalues increases in a more quadratic manner. The presence of the tail in the DOS requires many eigenvectors to be considered to obtain the conduction path in Al

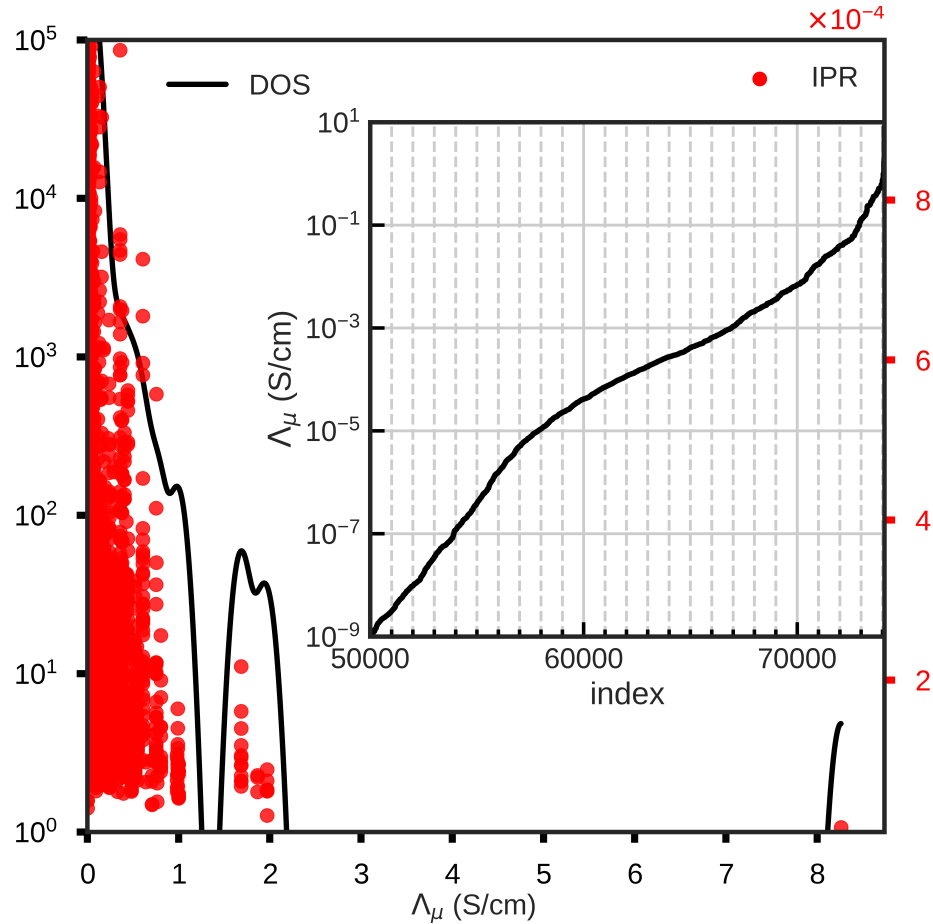


Figure 2.12: c-Al: Logarithmic spectral density of states of Γ -matrix. The left scale corresponds to density of states (DOS) of the eigenvalues displayed in a log scale (solid black line) and the right scale corresponds to the extent of localization measured as IPR (\mathcal{I}) (solid red circles). The inset shows the magnitude of conduction eigenvalues in ascending order.

(which is of course fully delocalized through the cell). A small spectral gap appears near $\Lambda_\mu = 1.3$ S/cm from a physical origin that we have not yet determined. The other difference we find is the localization of the conduction eigenvectors where the modes are more extended for Al compared to what was observed in a-Si and the low density a-C model.

Figure 2.13 shows the conduction eigenvalues (Λ_μ) plotted against IPR (\mathcal{I}). We see that for small IPR, there exists a fairly clear inverse relation between eigenvalues and the

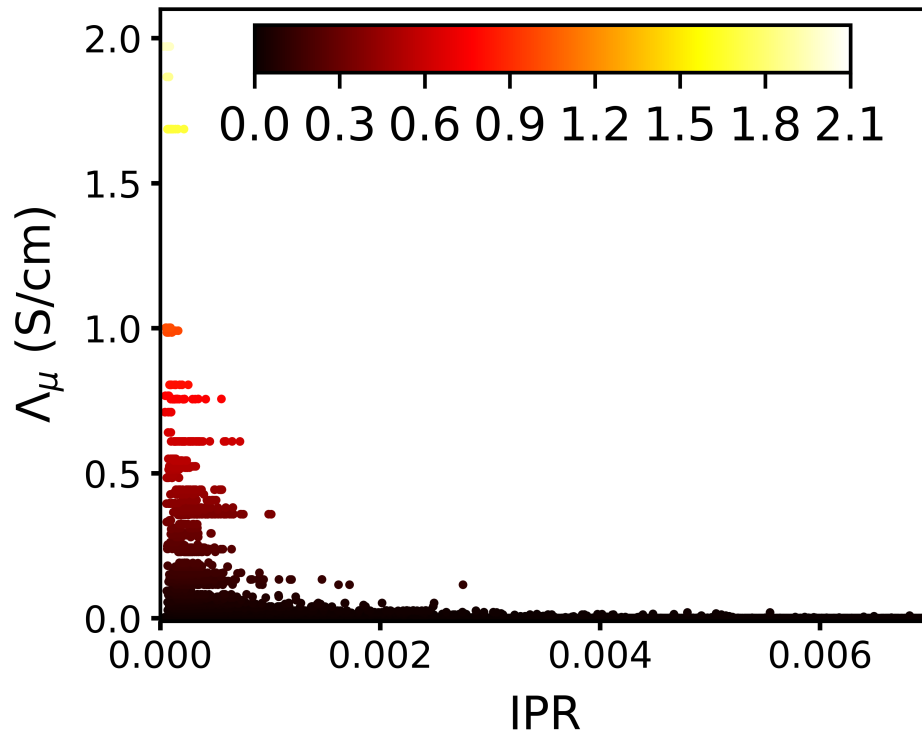


Figure 2.13: c-Al: The correlations of the eigenvalues with IPR (\mathcal{I}) shown by the scattered plots as heatmap. The colorbar at the central top of the figure refers to the magnitude of eigenvalues.

IPR. We also see Λ_μ near zero for low IPR. The eigenvectors corresponding to such eigenvalues can involve many sites, but always without forming any connected pattern and therefore corresponds to the non-conductive structures.

To visualize the conduction (really to see how a metallic conducting continuum emerges from this theory), we projected the conductivity from all the eigenvectors weighted by their eigenvalues and this is displayed as a heat map plot in Figure 2.14. The electrons in c-Al are highly delocalized, as a result, the projected values are essentially the same throughout the cell as shown in Figure 2.14. This is, of course, quite different from the semiconductors like a-Si and low density a-C where only some parts of the material serve as the conduction-active sites in the network that we discussed in the earlier subsection.

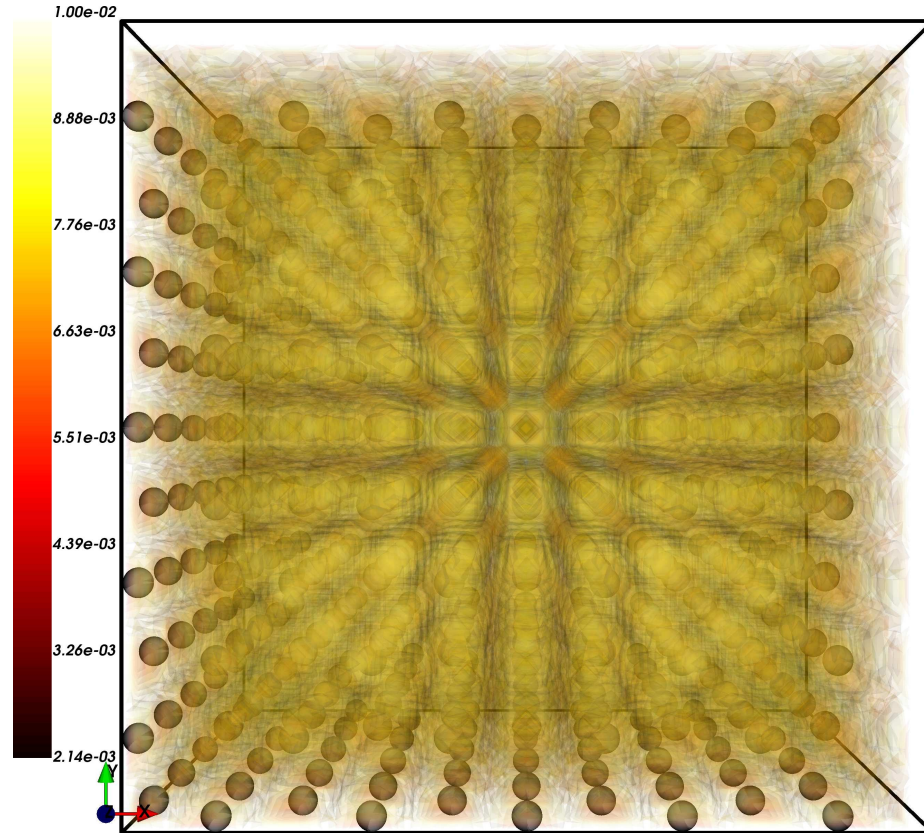


Figure 2.14: c-Al: Conductivity projected on grids weighted by the eigenvalues from all eigenvectors as a heat map plot (labeled by colorbars on the left) scaled with maximum value. The spheres represent Al atoms.

The other interesting property we find in the spectrum of the DOS in c-Al (refer Figure 2.12) is the presence of the degenerate eigenvalues towards the large Λ end of the spectrum. This is absent in the spectrum of a-Si and even the low density a-C. The degeneracy is surely a manifestation of the degeneracy present in the electronic levels, accruing in turn from the crystalline symmetry⁵. To visualize the conduction channel formed by the family of such degenerate eigenvalues, we projected the eigenvectors onto real space grids. Figure 2.15 shows the projection of eigenvectors for one of such family of the degenerate eigenvalues as a heatmap plot. The left plot shows that the eigenvectors

⁵ Only the $\mathbf{k} = 0$ point is used to sample the Brillouin zone, perhaps reasonable for a 500-atoms cell for this application, though in general this would be a doubtful approximation for a metal with its Fermi surface

split into four conduction channels within the supercell. The diagonal channels possess an inversion symmetry at the center of the supercell. The middle and the right heat maps correspond to the eigenvectors for other two eigenvalues in the family which direct along different directions, namely along x and y direction.

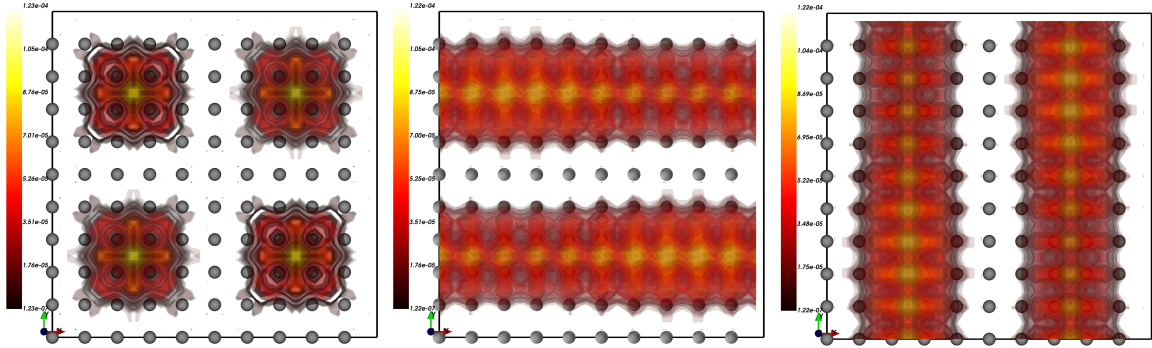


Figure 2.15: c-Al: Isosurface plots for eigenvectors corresponding to the degenerate eigenvalues ($\Lambda_\mu = 1.0013$ S/cm). The isosurface plot displayed as a heat map (labeled by the colorbars on left of each subplots) includes the values within 0.001 times the maximum value on the grids. Al atoms are represented by gray spheres in each plot.

2.7 Conclusions

We presented a method to compute a conductivity projected onto real space grids and we analyzed the spectral properties of the conduction matrix for a representative systems. For low density a-C, we find that the sp^2 and sp configurations form active conduction sites. The conduction path is formed between the sp chains and the pentagonal or hexagonal graphene rings in the network. For a-Si, we find SPC is distributed at nearby atomic sites at different parts in the network suggesting the possibility of hopping mechanisms for the electronic conduction. For a-Si, we find that the extreme eigenvectors pick atomic sites with different topology, involving tail states and strain defects for this 4-fold WWW model. We also studied fluctuations in the energy levels in liquid Si and provided the conduction path for few configurations. We showed that the 4-fold, 5-fold,

6-fold and 7-fold Si atoms form the conduction sites in the l-Si. We showed that diagonalization of $\Gamma(\mathbf{x}, \mathbf{x}')$ provides essential information about the nature of the conduction eigenmodes in different materials and helpfully categorizes the “paths” according to eigenvalue. From the spectrum of DOS of conduction eigenvalues, we always find a very large weight near $\Lambda = 0$. So, for materials like a-Si and a-C, only a few eigenvectors are sufficient to define the conduction path. For c-Al, we find that despite a significant accumulation of eigenvalues near $\Lambda = 0$, there is a spectral tail in the density of states and the channels corresponding to these states are extended. So, for metals, many eigenvectors are necessary to describe the conduction. We also observe a degeneracy in the conduction eigenvalues in the DOS of c-Al absent in the amorphous systems. We analyzed eigenvectors for one such degenerate eigenvalue near the extreme side of the spectrum and showed that these eigenvectors form a well defined conduction channel. We also provided an example of a silicon suboxide (a-SiO_{1.3}), where we projected the SPC for ($\omega > 0$) and showed that the O-vacancy sites form the major sites of conduction in such material.

It is not easy to extract quantitative conductivities for amorphous solids. Electron-phonon couplings are not included in static lattice computations and such temperature dependence is hardly a small effect. This is probably one reason why there are more computations of electrical conductivity in liquid metals, where dynamical effects (changes in electronic structure and therefore conduction due to atomic motion) are treated with Born-Oppenheimer dynamics. Also, in principle, methods producing accurate excited states perhaps employing hybrid functionals should be employed, and doubtless make a significant difference in the numerical value of the conductivity. However, we emphasize that the qualitative character of the SPC is far less sensitive to these effects than the numerical value of the conductivity, and the method offers a fairly robust picture of conduction activity in complex materials.

3 STRUCTURAL ORIGINS OF ELECTRONIC CONDUCTION IN AMORPHOUS COPPER-DOPED ALUMINA

The work presented in this chapter has been published as **Subedi, K. N., Prasai, K., Kozicki, M. N. and Drabold, D. A.** *Structural origins of electronic conduction in amorphous copper-doped alumina*, Phys. Rev. Materials 3, 065605 (2019)

3.1 Introduction

Non-volatile memory devices based on resistive switching characteristics have been studied since the late 1960s [111]. In these devices, application of an external bias potential across an electrolyte changes the electrical conductivity of the electrolyte by changing its structure. This process is reversible and can be performed in the time scale of nanoseconds. Three types of resistive random access memory (RRAM) devices have been studied in detail [10] and these include RRAM based on oxygen vacancies, RRAM based on thermo-chemical effects and RRAM based on the electro-chemical metallization. The later class of devices are also called conducting bridge random access memory or CBRAM. The CBRAM devices are composed of a thin solid electrolyte layer placed between an oxidizable anode (*eg.* Cu, Ag or TiN) and an inert cathode (*eg.* W or Pt). The Cu, in its ionic state, is converted into the conducting “filament” by the applied field: the ions are reduced by electrons flowing from the cathode to leave them in their metallic form, although other counter ions (*e.g.*, OH⁻) may also be involved in this process [112]. With the application of a reverse bias, the connectivity of the cluster can be destroyed, and the device is put into a highly electronically resistive state. The details of the mechanism of CBRAMs have been described elsewhere [113, 114]. The performance of CBRAM devices has been studied with several materials as the solid electrolyte which include chalcogenides [18, 19], insulating metal oxides [8, 11, 12, 14, 15, 115, 116] and bilayer

materials [117, 118]. CBRAM devices have demonstrated excellent performance in terms of operational voltage, read/write speed, endurance and data retention. Among the host materials reviewed for CBRAM devices, alumina (Al_2O_3) shows particular promise. It has a high dielectric constant, large band gap, and its amorphous phase is highly stable [119, 120]. The experimental results for CBRAM devices based on Cu alloyed with Al_2O_3 have shown that the cell exhibits highly controlled set and reset operations, fast pulse programming (10 ns) at low voltage (<3 V) and low-current (10 μA) with 10^6 cycles per second for the writing speed [8].

In this chapter, we use AIMD to generate atomic models of a- Al_2O_3 :Cu and investigate the microscopic origin of electronic conduction in this material. The work presented in this chapter shows that an increase in local Cu-concentration can result in stable conducting pathways due to the strong tendency of Cu atoms to cluster in the ionic host. This would lead to a highly stable low resistance state (LRS) for high copper concentration, which does indeed seem to be the case for copper-alumina devices [8]. We study the electronic properties for these models and are able to crudely estimate the local concentration of Cu above which CBRAM device switch to the LRS. We present the numerical computation of conduction-active parts of the network by computing the space-projected conductivity and show that the strong electron-lattice coupling for electron states near the gap leads to interesting and substantial thermally induced conductivity fluctuations on a picosecond time scale.

The rest of the chapter is organized as follows. Section 3.2 describes computational details used to create the structures and also the details of our method to obtain the SPC. Section 3.3 includes results where we discuss structural, electronic and vibrational properties of the models in different subsections. Section 3.4 provides the conclusions.

3.2 Computations

3.2.1 Model Generation

In this work, we use AIMD to generate four atomic models with the composition of $(\text{a-Al}_2\text{O}_3)_{1-n}\text{Cu}_n$ with $n = 0, 0.1, 0.2$ and 0.3 . We used a density of 3.175 g/cm^3 for $\text{a-Al}_2\text{O}_3$ [121, 122]. For the Cu-doped models, we referred to the literature [123] to make an initial guess, then carried out a zero-pressure relaxation to correct/optimize the result. For each model, we began by taking a cubic supercell of 200 atoms with randomly initialized positions of the atoms. Plane wave density functional calculations were performed using the VASP package and PAW [124, 125] potentials within the local density approximation (LDA) [126] using periodic boundary conditions. We used a kinetic energy cutoff of 420 eV and the Γ -point to sample the Brillouin zone. A time step of 1.5 fs was used and the temperature was controlled by a Nosé-Hoover thermostat throughout.

We performed a melt-quench simulation with a starting temperature of 3500 K. After annealing the “hot liquid” for 7.5 ps at 3500 K, we cooled each model to 2600 K at a rate of 0.27 K/fs as discussed in reference [127] followed by equilibrating it for 10 ps. Each model was then quenched to 300 K at the same cooling rate 0.27 K/fs and further equilibrated for another 10 ps. Zero pressure relaxations were used to determine the final densities for Cu-doped models. The final force on each atom is no more than 0.01 eV/\AA . The initial and final densities are provided in table 3.1.

3.2.2 Spatial Projection of Electronic Conductivity

To compute the SPC, we use equation 2.6 in chapter 2. We used VASP [83] and associated Kohn-Sham orbitals $\psi_{i,\mathbf{k}}$. We divided the supercell into $36 \times 36 \times 36$ ($\text{dim}\Gamma = 46656$) with grid-spacing of width $\approx 0.4 \text{ \AA}$. We used an electronic temperature of $T = 1000 \text{ K}$ for the Fermi-Dirac distribution. We approximated the δ

Table 3.1: Initial and Final Densities of a-Al₂O₃:Cu Models

Cu content	Mol. Formula	ρ_{in} (g/cc)	ρ_f (g/cc)
0%	(Al ₂ O ₃) _{1.00} Cu _{0.00}	3.175	3.175
10%	(Al ₂ O ₃) _{0.90} Cu _{0.10}	3.58	3.75
20%	(Al ₂ O ₃) _{0.80} Cu _{0.20}	3.78	3.99
30%	(Al ₂ O ₃) _{0.70} Cu _{0.30}	4.53	4.82

function in the expression of g_{ij} (of Equation 2.1) by Gaussian distribution of width 0.05 eV.

3.3 Results and Discussion

3.3.1 Bonding and Topology of the Models

As a test of validity of our models, we compute the total radial distribution function, $g(r)$, on a-Al₂O₃ models and compare with experimentally measured neutron scattering $g(r)$ from reference [128]. A plot showing these two $g(r)$ is presented in Figure 3.1 and shows that the models capture the structural order upto 6 Å reasonably well. We also compute the structure factor, $S(q)$, on our models at 2600 K and compare it with $S(q)$ measured on l-Al₂O₃ [129]. The plot shows that these two $S(q)$ show a satisfactory agreement, especially on the positions of peaks at 1.8 Å⁻¹, 2.8 Å⁻¹, 4.7 Å⁻¹. The bottom left plot in Figure 3.1 presents the partial $g(r)$ computed on models of a-Al₂O₃. The peaks at 1.81 Å, 2.78 Å and 3.17 Å correspond to the geometrical bond distances for Al-O, O-O and Al-Al pairs respectively; these results are in agreement with similar earlier works [130, 131, 132]. The bottom right plot in Figure 3.1 shows the partial $S(q)$ corresponding to Al-Al, Al-O and O-O pairs computed on a-Al₂O₃ models. We see that the first peak in the total $S(q)$ occurs at 2.8 Å⁻¹ due to the partial cancellation arising from Al-O

correlations. For doped models, the computed $g(r)$ are plotted in Figure 3.2 and shows

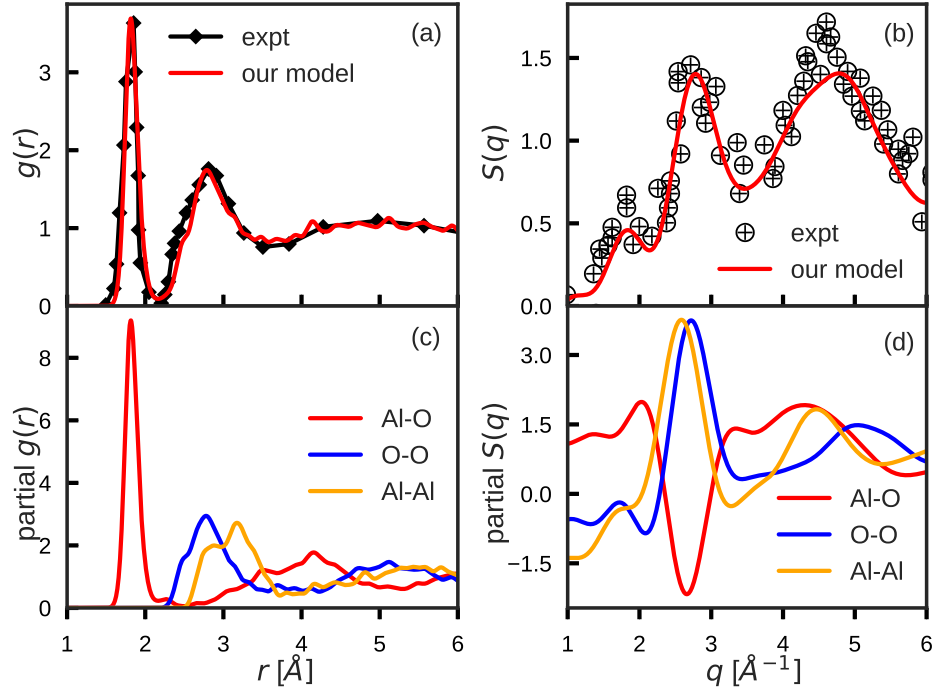


Figure 3.1: $g(r)$ and $S(q)$ of a- Al_2O_3 : (a) $g(r)$ computed on models are compared with measured $g(r)$. (b) $S(q)$ computed on models are compared with measured $S(q)$. (c) and (d) partial $g(r)$ and partial $S(q)$ respectively for Al-O, O-O and Al-Al pairs

that the position of first peak remains largely the same as undoped a- Al_2O_3 suggesting that Al-O bond remains unaltered. As the concentration of Cu increases, a hump corresponding to Cu-Cu correlation appears and grows at $r \approx 2.44 \text{ \AA}$. The relative sharpness of Cu-Cu hump, even for the lowest concentration of Cu, provides a hint that Cu atoms are probably clustered. Indeed, a visual inspection of the models, shown here in Figure 3.3, clearly shows the strong tendency of Cu-atoms to cluster.

It is significant that Cu strongly tends to cluster. A study by Dawson and Robertson [133] asserts that the Cu-Cu interactions become more favorable with increasing Cu content. We study the average coordination number around Cu atom at different

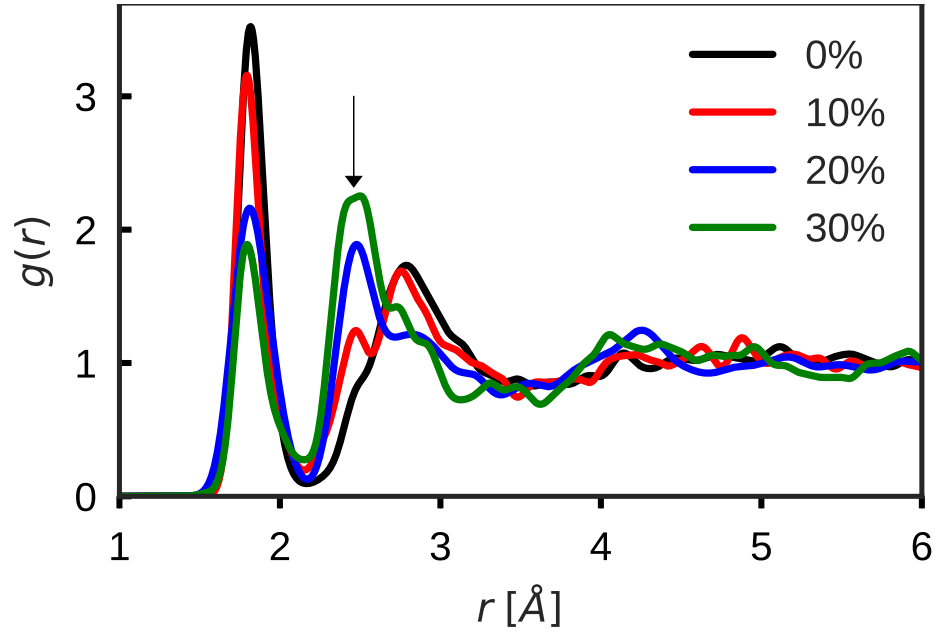


Figure 3.2: Total $g(r)$ computed from the models of $\alpha\text{-Al}_2\text{O}_3\text{:Cu}$ at various concentrations of Cu. The hump appearing in Cu-doped models, indicated by arrow, originates from Cu-Cu correlation.

Cu-concentrations as shown in table 5.1. We take the first minima in partial $g(r)$ as the cutoff distance to define the coordination number. The increase in Cu-coordination by Cu and the decrease in Cu-coordination by Al and O supports the segregation of Cu from the host and formation of cluster.

Table 3.2: Average Coordination Numbers around Cu Atoms for 10%, 20% and 30% Cu Models.

Cu content(%)	Cu-O	Cu-Cu	Cu-Al
10	1.15	5.1	3.0
20	0.68	6.85	2.45
30	0.48	8.27	1.78

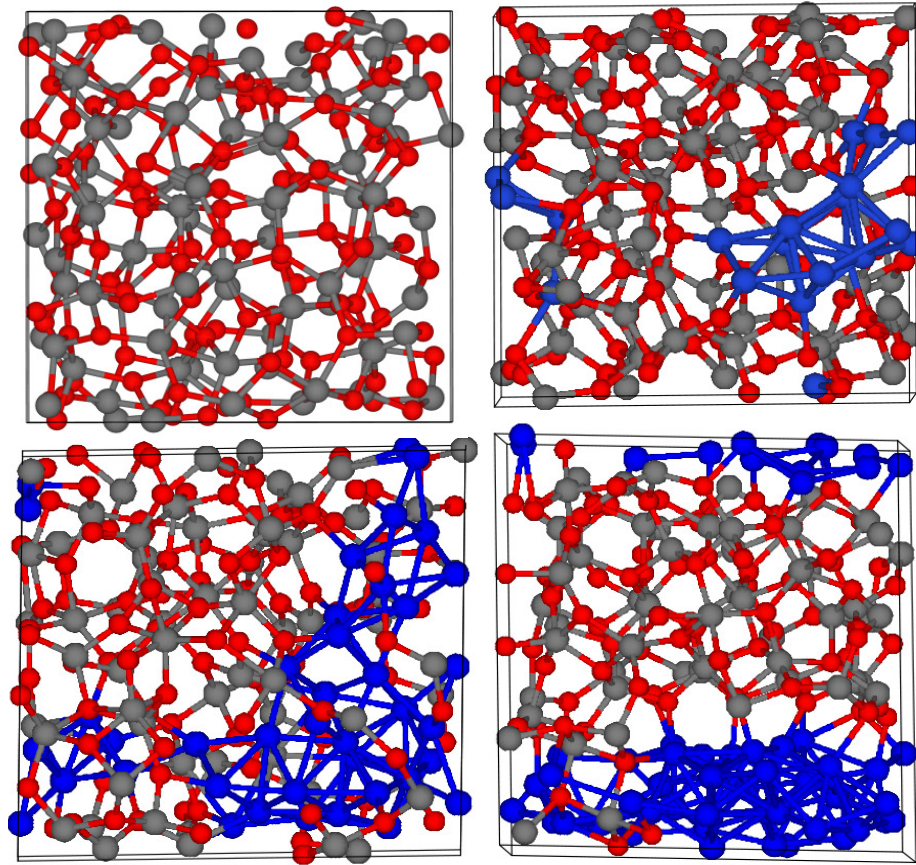


Figure 3.3: Final relaxed α - Al_2O_3 :Cu models. Top plots (from left) represent for 0%, 10% Cu and bottom plots (from left) represent for 20% and 30% Cu. Atoms color: Al (gray), Cu (blue) and O (red).

3.3.2 Electronic Structure

3.3.2.1 Density of States and the Localization

Alloying with copper in α - Al_2O_3 is expected to have effects on electronic properties which are of interest for applications of these materials in CBRAM devices. We investigate these effects by examining the density of Kohn-Sham eigenstates (EDOS) and their spatial localization. The localization is gauged by computing the inverse participation ratio (IPR) using Equation 1.9. Figure 3.4 shows the computed EDOS and

IPR as a function of Cu-concentration. We find a decrease in HOMO-LUMO gap with increasing Cu-concentration; at Cu-concentration 20% and 30%, The EDOS is continuous across the Fermi level. The states that fill-in the band gap are quite extended as indicated by small values of IPR around the Fermi level in Figure 3.4. The mean IPR values around the gap declines monotonically with Cu-concentration. To physically interpret the

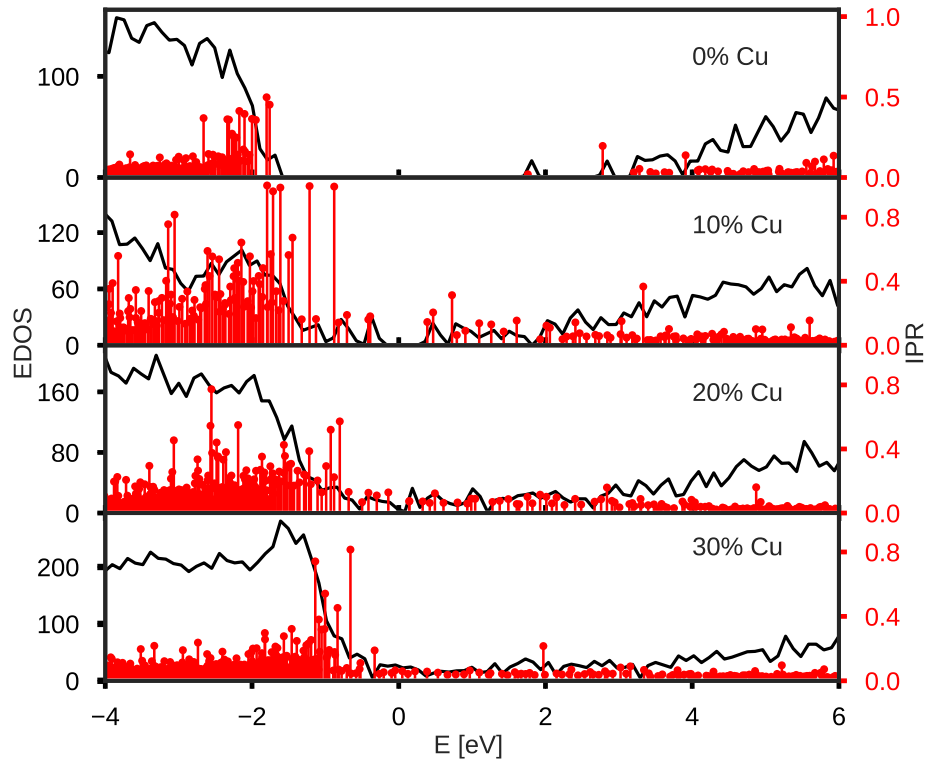


Figure 3.4: Electronic density of states (EDOS) and the inverse participation ratio (IPR) computed from $a\text{-Al}_2\text{O}_3\text{:Cu}$ models for different concentrations of Cu. The black curve represents EDOS and red vertical lines show IPR. The Fermi level is shifted to zero in all plots.

connection of the HOMO-LUMO gap and the extent of localization with electronic conductivity (σ), let us rewrite Equation 2.1 for the dc conductivity ($T = 0$ K) in the form of Mott and Davis [53]:

$$\sigma_{dc} = \frac{2\pi e^2 \hbar \Omega}{m^2} |D_{\epsilon_f}|^2 N^2(\epsilon_f) \quad (3.1)$$

where D_{ϵ_f} is a matrix element of ∇_{α} between Kohn-Sham states near the Fermi level and $N(\epsilon_f)$ is the density of states. For small gap, one expects more states near the Fermi level. The magnitude of matrix elements D_{ϵ_f} for extended states would be higher than the localized states. So, the conductivity could be crudely linked with the HOMO-LUMO gap of the material and the extent of localization of the Kohn-Sham states.

By projecting the electronic states onto atomic sites, we observe that the states near the Fermi level for the doped models consist of Cu-orbitals. An example of the site projected EDOS, for 20% Cu, is plotted in Figure 3.5. It is quite interesting that at 20% and 30% Cu-concentrations, Cu levels almost *uniformly* fill the host a-Al₂O₃ gap. The Cu does not form an impurity band, as one might naively suppose from experience on heavily-doped semiconductors. We see that models with higher Cu-concentration produce states near Fermi level that yield an essentially metallic form of conduction. This is qualitatively different than the case of Ag in GeSe₃ [134], wherein the Ag atoms do not cluster and do not introduce states in the optical gap of the host. We observe that electron states in the gap are filled mostly by 3d, 4s and 4p orbitals of Cu.

3.3.2.2 Charge Analysis on Cu Atoms

The formation of Cu-cluster in a-Al₂O₃ matrix leaves the Cu atoms in different charge states depending on the local environment of these Cu atoms with O and/or Al atoms. We performed Bader charge analysis [135] to calculate net charge on these atoms and an analysis for 20% Cu-doped model is shown in Figure 3.6. The charge state of the Cu atoms (shown in color in Figure 3.6) can be explained by a simple analysis of the first neighbors around the Cu atoms. Among all the Cu-atoms shown in the figure, only five Cu atoms have exclusively Cu neighbors and are neutral in nature; the rest of the Cu are neighbors with at least one Al or O atoms. When a Cu atom is a neighbor with Al or O atoms, bonding or charge transfer occurs. A Cu atom bonded with O atoms is positively

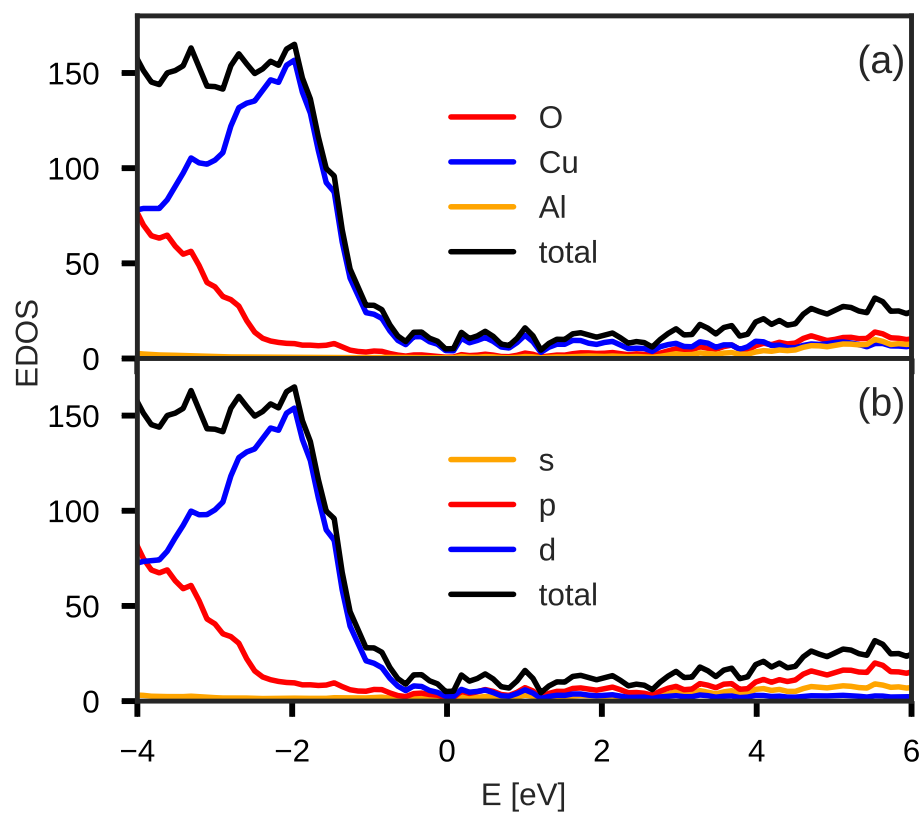


Figure 3.5: Projected electronic density of states (EDOS) computed from $a\text{-Al}_2\text{O}_3\text{:Cu}$ models with 20% Cu. (a) Site projected EDOS (b) Orbital projected EDOS. The Fermi energy is shifted to zero.

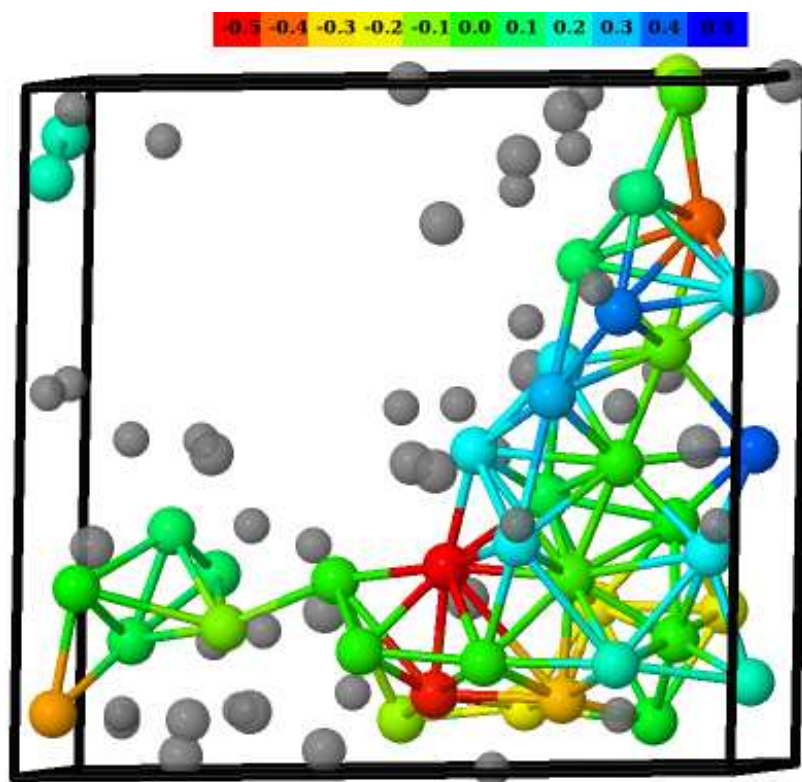


Figure 3.6: Net Bader charge on Cu atoms calculated from $\alpha\text{-Al}_2\text{O}_3\text{:Cu}$ models with 20% Cu-concentration. A color code displayed on top is used to represent the charge state. Charge state of zero, shown by green, represents a neutral Cu atom; the charge values are in units of electronic charge. All Cu-atoms are shown in color. Light gray atoms represent Al and O atoms within the first cutoff distance of Cu atoms

charged, whereas a Cu atom bonded with Al atoms is slightly negatively charged and can be understood in terms of difference in electronegativities of Cu and Al. When a Cu atom is bonded with both O and Al atoms, it is charge neutral. The charge compensation likely to happen in such bonding. The Cu atoms shown in green are therefore almost metallic in nature and are likely to form a conducting channel for the current to flow in the network.

3.3.2.3 Thermally Driven Conduction Fluctuations

In this section, we discuss relatively dramatic thermally-induced fluctuations in the HOMO-LUMO splitting and consider the electronic conduction mechanisms⁶. We illustrate with one of the conducting models (including 20% Cu) and performed MD at 1000 K for 24 ps. The fluctuation of the frontier HOMO and LUMO levels with time is provided in Figure 3.7. $\eta(t)$ is the HOMO-LUMO splitting through the course of the MD. The model reveals a large thermally driven fluctuation in the value of the HOMO-LUMO gap with time. As we discussed earlier in Section 3.3.2.1

So, for dc conduction to occur, there needs to be finite density of states at the Fermi level (to enable electronic transitions, as from Fermi's Golden Rule) and non-vanishing matrix elements $|D_{\epsilon_f}|^2$ as in Equation 2.1. We expect more available states near the Fermi level for the system with small gap, thus the conductivity $\sigma(t)$ can be very crudely linked to $\eta(t)$ (small $\eta \implies$ large σ) in the spirit of Landau-Zener tunneling [136, 137]. We provisionally interpret the small gap (small η) instantaneous configurations as low resistance states, and the large gap configurations as high resistance states.

It is therefore interesting to visualize the conduction-active parts of the network for these different states. We selected two snapshots (shown by orange arrows in Figure 3.7), one representing a small gap (low η) and the other large gap (high η) from the simulation and obtained the SPC. The variation of the HOMO-LUMO gap due to thermal fluctuations has also been studied in Boron-doped *a*-Si at 600 K, where it was observed that with addition of hydrogen to the network, there occurs a thermal modulation of HOMO and LUMO states causing the HOMO and LUMO states to be overlapped at a certain interval of the thermal simulation representing highly conducting configuration [138]. This computation makes it clear that the DC conductivity is difficult to accurately estimate,

⁶ Here and elsewhere in this chapter, electronic time evolution refers only to variation in Kohn-Sham eigenvalues/states on the Born-Oppenheimer surface – no attempt is made to solve a time-dependent Kohn-Sham equation

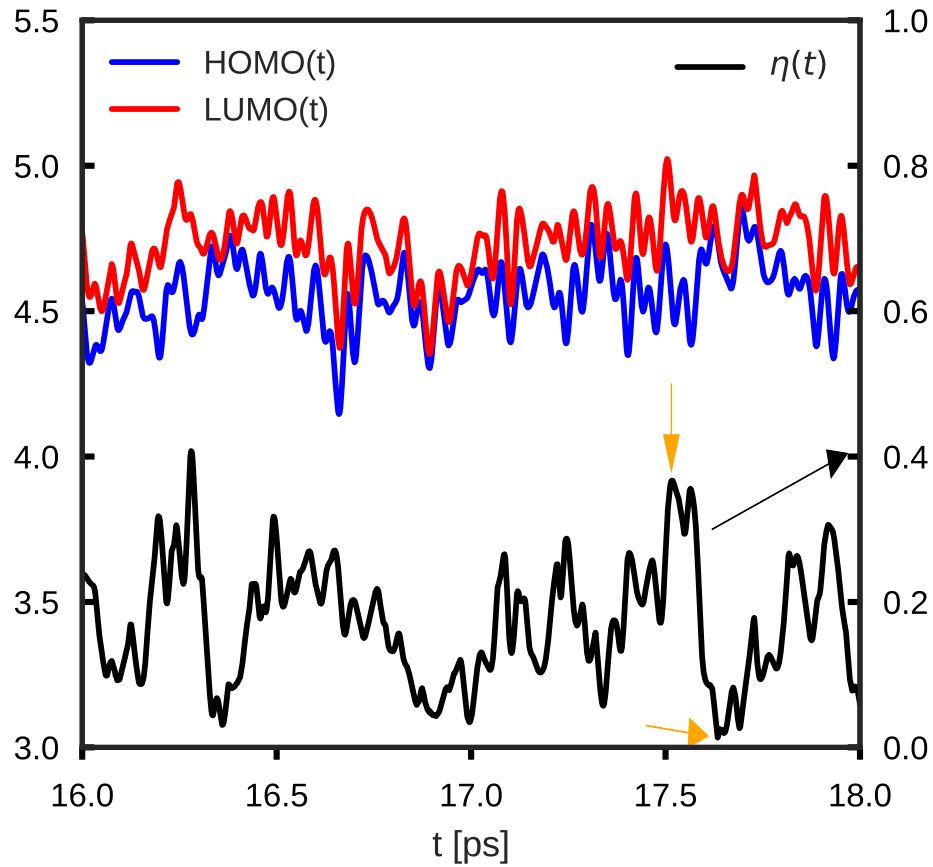


Figure 3.7: Fluctuation of HOMO, LUMO and HOMO-LUMO gap (η) with time for 20% model at 1000 K. $\eta(t)$ is represented by black line with its values given by right axis of the plot as shown by arrowhead in the plot.

since to handle the large electron-phonon coupling for states near the Fermi level, long MD averages at constant temperature would be required (within an adiabatic picture for which one simply averages the Kubo formula over a trajectory).

3.3.2.4 Space-Projected Conductivity

We investigated SPC by computing $\zeta(x)$ as described in section 2.4 in chapter 2 in our models. SPC values are evaluated at coarse 3D grid points inside the supercells. A graphical representation of SPC values in 3D grid points overlaid with the atomic

configuration is shown in Figure 3.8. This figure shows the SPC computed on two models: one with large η and the other with and small η . We include 12% of the highest local contributions to SPC in each plot. The SPC reveals that the conduction path is primarily along interconnected Cu atoms. A few O atoms in the vicinity of Cu atoms also participate in the conduction whereas Al atoms do not show any role in the conduction. We see that the SPC for the large gap snapshot is disconnected so that $\zeta(x)$ appears to be localized in certain region whereas the SPC with small gap forms an interconnected chain for the conduction. For these two particular structures, we observed the local configurations as shown by the enclosed circles of Figure 3.8 where the Cu atoms come closer to form short bonds and form a closed network. This shows that the connectivity among Cu atoms determines the conductivity of the system. Besides the structural difference, the type and the number of clusters also affect the HOMO-LUMO gap. It has been shown that an alternation of the HOMO-LUMO gap occurs between even and odd numbered isolated clusters due to electron-pairing effects and particularly large gap for cluster size 2, 8, 18, 20, 34 and 40 which are also called as magic clusters [139]. At this temperature, the diffusion of Cu atoms may cause the change in the bonding environment of Cu atoms resulting in the variation of the gap with time.

3.3.3 Ion and Lattice Dynamics

Since the ion and lattice dynamics are of key importance for applications, we discuss these in this section.

3.3.3.1 Ionic Motion

As a representative example, the 20% model was annealed at different temperatures 800 K and 1000 K for 15 ps, and the resulting ion dynamics were studied by calculating the mean-squared displacement (MSD) for each atomic species as:

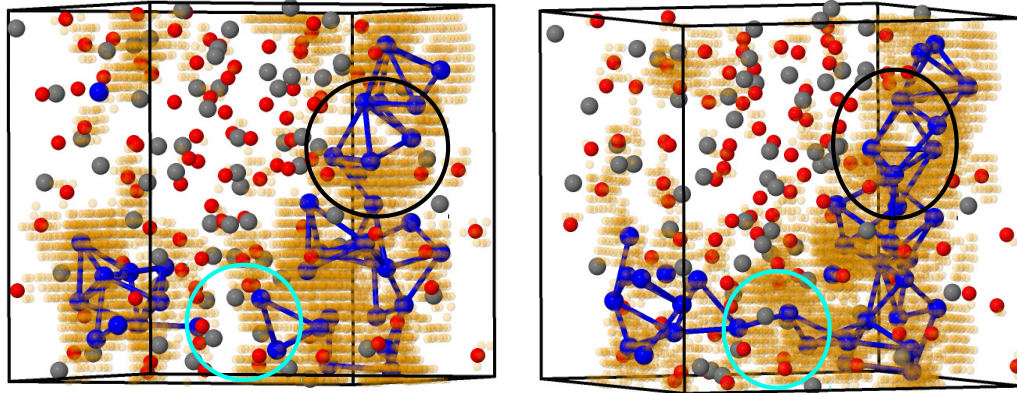


Figure 3.8: Overlaying SPC values (orange transparent spheres) with atomic configuration: On the left, large gap (high resistance) state of a-Al₂O₃:Cu model with 20% Cu. On the right, small gap (low resistance) state of the same system. Color nomenclature: blue- Cu atom, red- O atom and gray- Al atom. The bond length of cutoff 2.6 Å is chosen. Circles with same color represent same part of local configurations. There is a factor of about 10⁴ between the conductivities of the two conformations.

$$\langle r^2(t) \rangle_\alpha = \frac{1}{N_\alpha} \sum_i^{N_\alpha} \langle |\vec{r}_i(t) - \vec{r}_i(0)|^2 \rangle \quad (3.2)$$

where N_α represents the number of atoms of species α , $r_i(t)$ represents the position of atom i at time t , and the $\langle \rangle$ represents an average on the time steps and/or the particles.

The connection between mean-squared displacement and the self-diffusion coefficient is given by Einstein's relation

$$\langle r^2(t) \rangle = A + 6Dt \quad (3.3)$$

where D is the self-diffusion coefficient, A is a constant and t is the simulation time.

Figure 3.9 shows the mean-squared displacement for the corresponding species. Clearly, Cu atoms are more diffusive than Al and O atoms. On taking the snapshots of the position of atoms (figures not shown here), we find that the Cu atoms do not diffuse into the host matrix but diffuse within the Cu clusters and thus the Cu clusters become stable at these range of temperatures. We then calculated the self-diffusion coefficient for each species using Equation 3.3. The diffusion coefficient for Cu at 800 K and 1000 K are obtained to

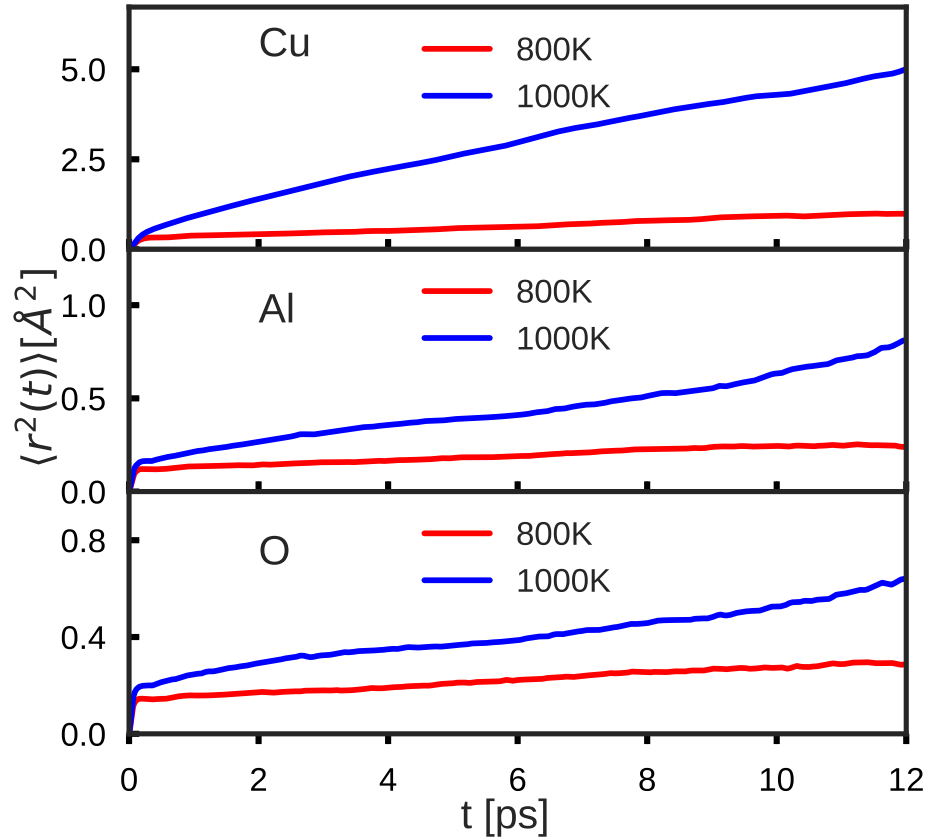


Figure 3.9: Mean-squared displacement at 800 K and 1000 K for 20% Cu model.

be $9.95 \times 10^{-7} \text{cm}^2/\text{s}$ and $6.248 \times 10^{-6} \text{cm}^2/\text{s}$ respectively. Cu is relatively static in a- Al_2O_3 compared to chalcogenides [140].

3.3.3.2 Lattice Dynamics

Here, we study the lattice dynamics of these Cu-doped systems by the means of VDOS, species projected VDOS and the vibrational IPR. The dynamical matrix is obtained by displacing each atoms by 0.015\AA along $\pm x$, $\pm y$ and $\pm z$ directions. The VDOS and partial VDOS are obtained by using Equations 1.10 and 1.11 respectively. We approximate the δ function in VDOS expression by a Gaussian distribution function of

width 10 cm^{-1} . Among the $3N$ eigenmodes, we neglect the first three translational modes with frequency very close to zero..

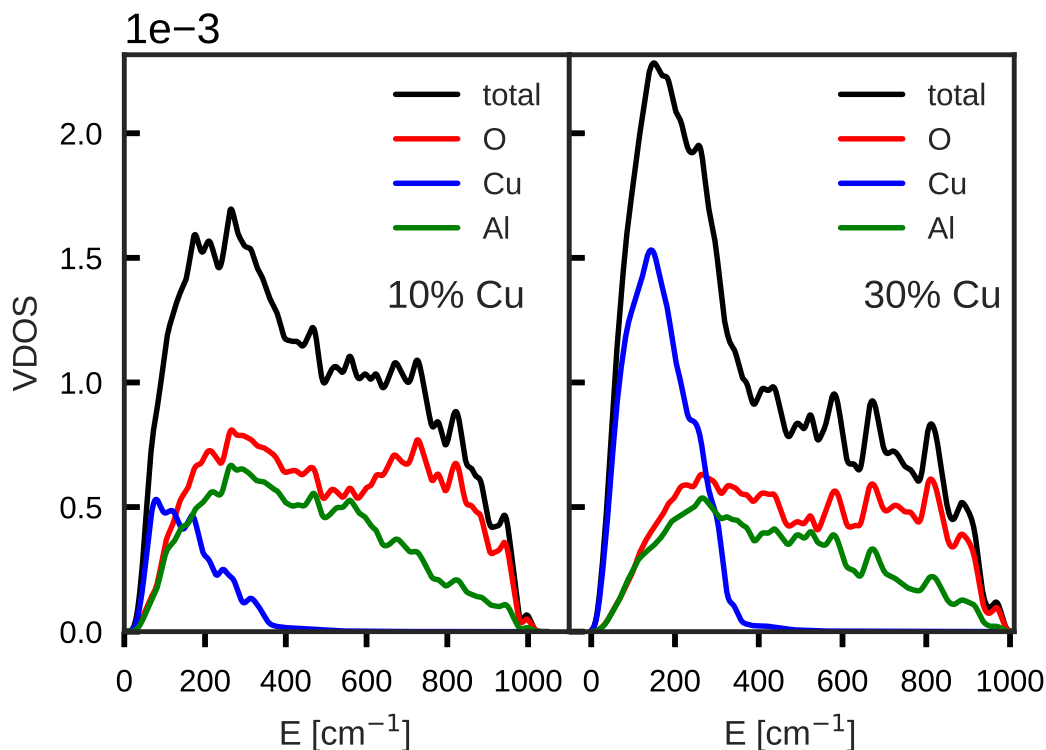


Figure 3.10: Normalized total and partial vibrational density of states for 10% and 30% of Cu models.

Figure 3.10 shows the total and partial VDOS for 10% and 30% Cu content. The lower vibrational modes correspond to the Cu atoms. The higher frequency modes are unsurprisingly dominated by O atoms. To study the localization of the vibrational eigenstates, we calculated the vibrational IPR for each species. From Figure 3.11, we see that the higher modes corresponding to the O atoms are more localized compared to the lower modes for both concentrations of Cu. The lower eigenstates corresponding to Cu for 10% Cu model are quite localized compared to the 30% Cu model. The vibrational states for aluminum are mostly extended for both models.

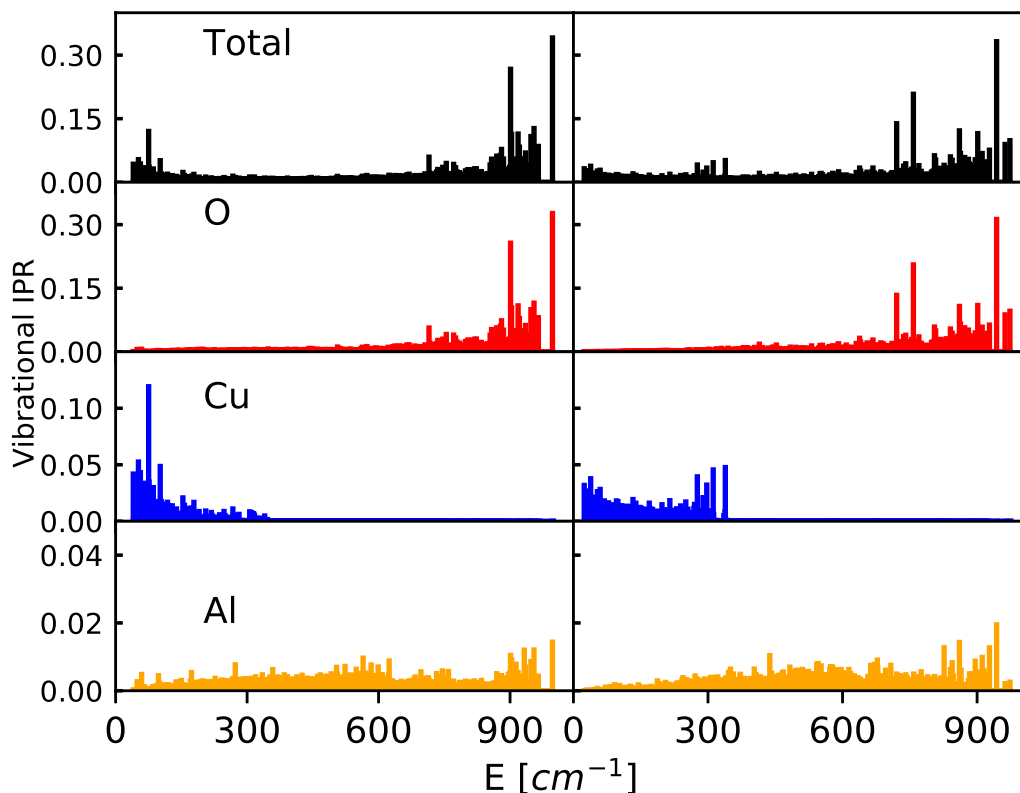


Figure 3.11: Vibrational IPR different models. Left column for 10% model and the right column for 30% model.

3.4 Conclusions

In this chapter, we studied realistic models of $\alpha\text{-Al}_2\text{O}_3\text{:Cu}$, and showed that the Cu atoms have a strong propensity to cluster in the ionic $\alpha\text{-Al}_2\text{O}_3$ host. We observed a continuous filling of the optical gap by Cu levels, especially at 20% and 30% models. As the Cu-concentration increases (and Cu-Cu connectivity increases), the Cu levels band to enable metallic conduction. We observed the opening and closing of the HOMO-LUMO gap at an elevated temperature, and projected electronic conductivity into real space and visualized the conduction-active parts of the network. We showed that the connectivity of Cu atoms play a significant role in the electronic conduction. We studied the diffusion of Cu atoms in $\alpha\text{-Al}_2\text{O}_3$ at different temperatures and observed that the Cu atoms do not

diffuse easily into the $a\text{-Al}_2\text{O}_3$ in contrast with relatively covalent chalcogenides like GeSe_3 [140]. We discussed the harmonic lattice dynamics of the models by calculating vibrational density of states and the vibrational IPR and showed that the lower vibrational modes correspond to Cu atoms and the higher modes correspond to O atoms.

The results presented in this chapter on $a\text{-Al}_2\text{O}_3\text{:Cu}$ show an interesting contrast with similar study performed on $\text{GeSe}_3\text{:Ag}$ [141]. We find that the properties of Cu in the oxide host (in this case, $a\text{-Al}_2\text{O}_3$) contrast with that of Ag in chalcogenide (in case of [141], GeSe_3). The Ag atoms do not form a cluster in the GeSe_3 and no uniform filling of the optical gap is observed. In other words, one has to electrochemically work hard to draw Ag atoms together to form a cluster in GeSe_3 . So, the electronic conduction is likely to occur by hopping process in $\text{GeSe}_3\text{:Ag}$ whereas the conduction in Al_2O_3 is most likely through the interconnected Cu atoms in the network. We observed that Cu in $a\text{-Al}_2\text{O}_3$ exhibits different charge states (negative, neutral and positive) whereas the charge state of Ag in GeSe_3 changes from neutral when isolated to ionic (positive) near the trapping center sites (host atoms) [142].

4 ELECTRONIC CONDUCTION IN AMORPHOUS SILICON SUBOXIDES

The work presented in this chapter is in preparation for submission **Subedi, K., Kozicki, M. N. and Drabold, D. A.** *Ab initio study of structural and transport properties in silicon suboxides*

4.1 Introduction

Silicon suboxide ($a\text{-SiO}_x$) is a desirable electronic material because it can be cheaply produced, has great physical and chemical stability and natural compatibility with modern CMOS technology. $a\text{-SiO}_x$ thin films are also used for fabricating light-emitting silicon-based structures [143]. The structure of silicon sub-oxide is complex and the experimental evidence mostly supports two different structural models: “random mixture” [109] and “random bonding” [110]. The former model proposes regions of pure Si and silica (SiO_2), separated by small interfacial boundaries whereas the latter model suggests a continuous random network of tetrahedral units of $\text{SiSi}_y\text{O}_{4-y}$ where $y = 0$ to 4. SiO_x is extensively studied intrinsic material for resistive devices [144, 145, 146]. Two different approaches to conduction mechanisms in SiO_x resistive devices have been discussed: field-driven diffusion of the metal ions from metal contacts into the material [147, 148] and formation of conduction pathways by silicon-rich regions in the material [149, 150]. The devices have been understood at the macroscopic level but the fundamental microscopic aspects of conduction mechanisms in bulk SiO_x is unclear. The actual mechanisms of how oxygen vacancies affect the electronic properties of the material is still not fully understood. Beside memory storage, the security of the data is important. As we introduced in Chapter 1, PUF is a promising concept of securing the data without using any expensive hardware. The performance of the PUF device depends critically on the merits of the material employed. For better PUF quality, a significant variation in the structure is required. The inherent randomness in the structure of $a\text{-SiO}_x$

makes it a promising candidate for PUF devices. To improve these devices, understanding the structure, stability, electronic and transport property is needed. More specifically, visualization of the conduction-active parts of the network within the bulk material is of central importance.

In this chapter, we aim to understand the underlying complexity in the structural topology and the associated microscopic properties of a-SiO_x. We propose that the inherent complexity of this material has its possibility for the ideal PUFs application along with the resistive devices. The rest of the chapter is organized as follows: We first use *ab initio* methods to simulate silicon-suboxide models with varying stoichiometry and identify the structural topology. We then provide detail study on electronic properties and visualize the most probable conduction sites in the material for a selected models.

4.2 Computational Details

4.2.1 Generation of Atomistic Models

Our calculations are based on AIMD simulations performed using VASP [83]. We generated three atomic models of a-SiO_x with $x = 1.7, 1.5$ and 1.3 . For each model, we constructed a cubic supercell with random initial atomic positions, fixing the volume and the number of atoms to reproduce experimental density [151] according to desired stoichiometry (summarized in Table 4.1). The generalized gradient approximations (GGA) of Perdew-Burke-Ernzerhof (PBE) [84] was used as the exchange-correlation functional. A plane-wave basis set was used with a kinetic energy up to 400 eV to expand electronic wave-functions during MD simulations. For static calculations, larger cutoff of 520 eV was used. The calculations were performed using a single k -point (Γ) and periodic boundary conditions were employed through out.

We followed the quench-from-melt scheme [88] to generate our models. For each model, the initial configuration was heated at 4000 K for 10 ps. After annealing, we

cooled this “hot liquid” to 2000 K at a rate of 0.20 K/fs and then equilibrated at 2000 K for 6 ps. We further cooled each model to 1000 K at the same rate and equilibrated it for next 4.5 ps. Each model was then quenched to 300 K followed by equilibrating it for another 6 ps. The temperature was controlled by a Nose-Hoover thermostat [152, 153, 154] and timestep of 1.5 fs was used during all MD runs. We fully relaxed each model using the conjugate gradient method as implemented in VASP to obtain low energy structures. We used the force tolerance of 0.005 eV/Å during the relaxation.

Table 4.1: System Stoichiometries and Densities for SiO_x Models

Mol. Formula	N_{Si}, N_O	ρ (g/cc)	L (Å)
SiO _{1.7}	70, 119	1.99	14.78
SiO _{1.5}	74, 111	1.87	15.07
SiO _{1.3}	80, 104	1.68	15.69

4.3 Results and Discussion

4.3.1 Structural Topology

We study the structural topology of the models by calculating the pair-correlation functions and local-coordination environment of atoms. To our knowledge, the total pair correlation function, $g(r)$ for a-SiO_x has not been determined experimentally.

The left plot in Figure 4.1 shows $g(r)$ for the obtained a-SiO_x models. The first well-defined peak at ≈ 1.64 Å corresponds to Si-O correlations. There is a hump at ≈ 2.39 Å that grows with decrease in x . This growing hump corresponds to Si-Si correlations that is shown by the inset in left plot of Figure 4.1. The second major peak at ≈ 2.66 Å mainly comes from O-O partial correlations. The first peak in $g(r)$ shows that the intensity of Si-O correlations decreases with decrease in x which causes reduction of SiO₄ tetrahedral

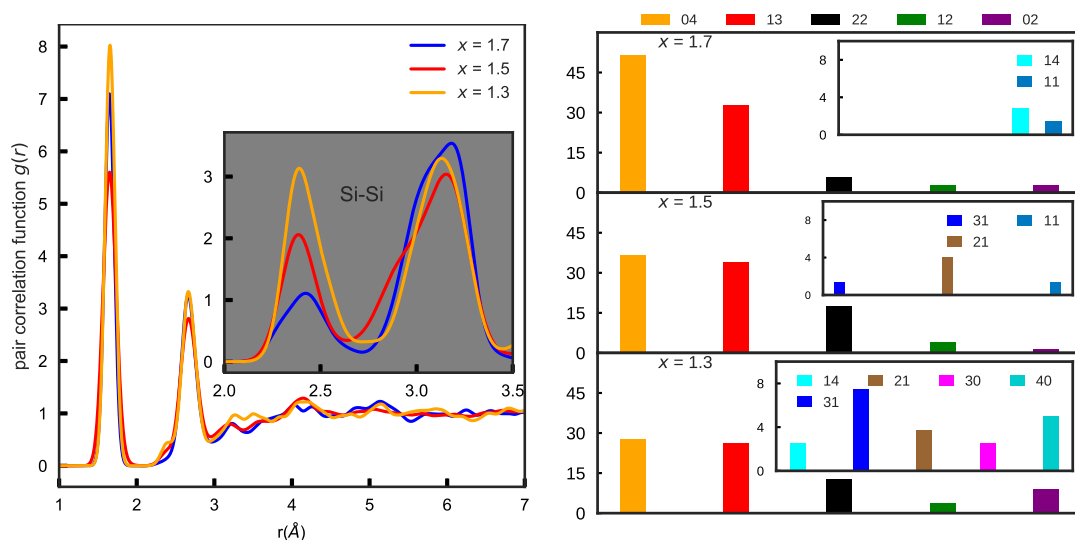


Figure 4.1: LEFT: Pair correlation function $g(r)$ with inset showing the partial $g(r)$ due to Si-Si bonding. RIGHT: Local coordination environment for Si atoms (frequencies expressed in percentage). The inset plots correspond to the correlations that belong only to that model. The first index of the label represents Si and the second index represents O atom.

structure. To gain further insight into the topology of the models, we performed local coordination analysis around Si atoms based on the nearest distance for each atomic pairs displayed as histogram bars (frequency in percentage) in the right plot of Figure 4.1. The histogram bars in the right plot of Figure 4.1 show that the continuous random tetrahedral units of SiO_4 , SiSiO_3 , SiSi_2O_2 are present in all models. The dominant SiO_4 and SiSi_3O units decrease with decrease in x . The SiSi_3 and SiSi_4 are observed only with small x shown as inset plot in the right plot of Figure 4.1. This provides a signature of Si rich regions in the network with low x . These non-stoichiometric oxides possess large number of O-deficient sites in the network which are well known defects in metal oxides as O-vacancy sites. The formation of O-vacancy sites in a- SiO_2 has been studied in earlier works [155, 156, 157]. In these calculations, O-vacancies were created by removing one or more O atoms from a- SiO_2 . The stable O-vacancies after relaxation are shown with different shapes; Y-structure, member ring or a chain for di-vacancy or tri-vacancy sites.

Figure 4.2 provides visual representation of distribution of these sites in the network for a-SiO_x models with low x (here $x = 1.3$). The inherent randomness in the structural topology of the SiO_x, (here for eg. with $x = 1.3$) can have potential applications for the PUF devices. Figure 4.2 shows that O-vacancy sites which are closer to each other form a

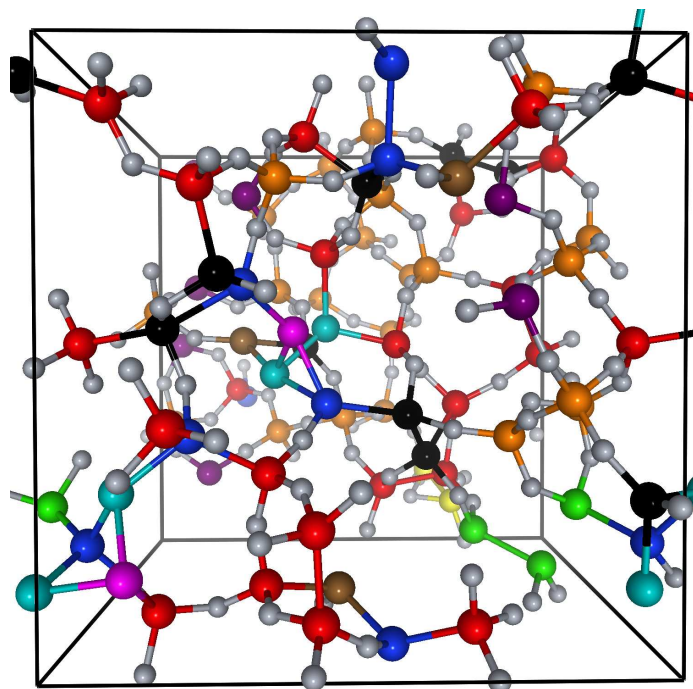


Figure 4.2: Relaxed structure for a-SiO_x model with $x = 1.3$. The color of Si atoms correspond to the coordination of Si in the network within the first nearest distance for each atom pairs. The color code is same as the right plot of Fig. 4.1. The O atoms are colored gray.

member ring or a chain in some parts of the network. With further decrease in x , one expects more Si-rich regions in the network. The previous work by Hirata *et al.* [158] has shown the phase separation between Si and SiO₂ for $x = 1.0$. The Si-rich regions in the network for low x could significantly impact on electronic conduction in the material and are of obvious importance to any device applications.

4.3.2 Electronic Structure

The electronic properties of the models are studied by detailed understanding of electronic structure in a material. We discuss the properties in different subsections.

4.3.2.1 Density of States and Localization

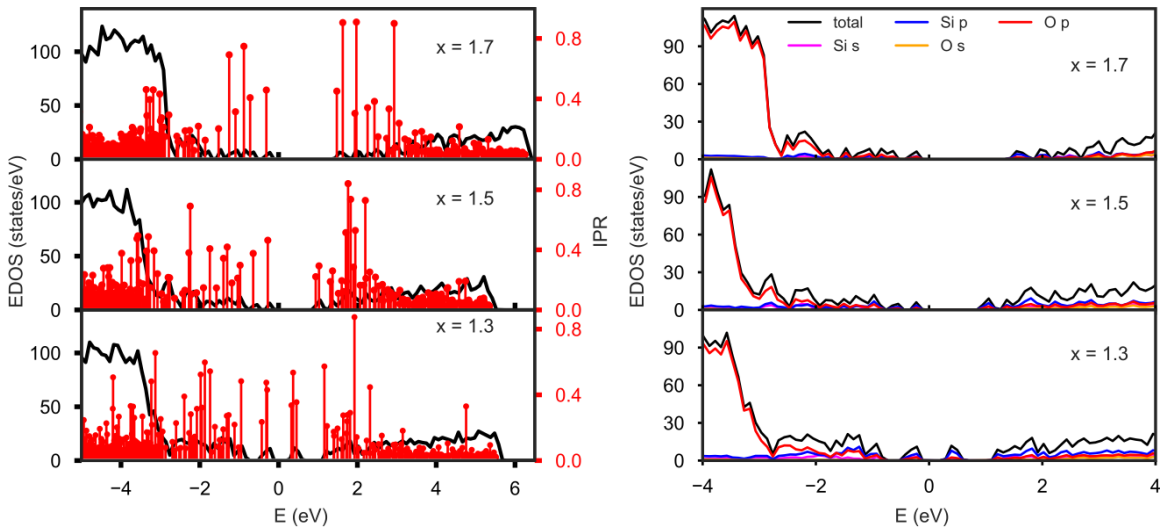


Figure 4.3: LEFT: Electronic density of states (EDOS) and the inverse participation ratio (IPR) for a-SiO_x models. RIGHT: Electronic density of states projected on to each orbital of each atomic species for a-SiO_x models.

The states near the Fermi-level are analyzed by calculating the total electronic density of states (EDOS) and projected EDOS due to each atomic species as shown by left axis in each plot of Figure 4.3. It is apparent that the EDOS near Fermi-level increases with decrease in x . The models with $x = 1.7$ and 1.5 show clear band gaps indicating that these sub-oxides are non-conducting. The further decrease in x (here $x = 1.3$) shows the presence of defect states pinned very close to the Fermi level. The EDOS projected on atomic sites (*refer* to right plot in Figure 4.3) shows that electronic states from Si atoms (shown by blue lines) in each plot pile up near the Fermi-level with decrease in x . So, the electronic states from under-coordinated Si (with O atoms) atoms play crucial role to

enhance the conductivity in a-SiO_x models. The extent of localization of these electronic states is further gauged by calculating IPR. The IPR is shown by red colored vertical dropped lines labeled on right axis in each plot in Figure 4.3. For all models, the states in the valence and conduction tail regions are localized. The defect states pinned very close to Fermi-level for $x = 1.3$ are also localized, so one would predict electronic conduction primarily by hopping mechanisms between these localized states.

4.3.3 Conduction Active Parts of the Network

The electronic conductivity of a-SiO_x is influenced by the variation of its structural topology. In order to correlate conduction with the structure, we computed SPC for the obtained models. Figure 4.4 shows iso-surface plots of SPC (yellow colored blobs) for a-SiO_x models where the SPC values up to 0.04 times the highest SPC value are displayed in each plot. The occupancy of the states was estimated assuming that the Fermi-level lies at the midpoint of HOMO and LUMO levels (intrinsic case). From Figure 4.4, one can see that the O-vacancy sites play a key role for electronic conduction. We also find that a few Si atoms with strained SiO₄ tetrahedral structure also form active sites for charge trapping and hence contribute to SPC (orange colored spheres in left and middle plot of Figure 3). However, such sites are rare compared to the O-vacancy sites. For $x = 1.7$, majority of O-vacancy sites are far from the Fermi-level, and they do not contribute to the conduction. The conductivity is localized within a few O-vacancy sites and is scattered without forming any connected pattern. For $x = 1.5$, we find the Si atoms with dangling bonds are other charge trapping sites. With reduced x (here $x = 1.3$), the O-vacancy sites form a member ring and are connected as a chain (although short) as seen at the bottom right and top right regions (periodic boundary conditions) in the right plot of Figure 4.4. This connected network appears to form a conducting channel where the conduction is likely to occur by the trap-assisted tunneling (TAT) mechanisms, thereby enhancing the

conductivity. It should be noted that the electronic states that are considered in the calculations are few (refer to Figure 4.4) due to finite size effects. So, the SPC is mostly qualitative, nevertheless, it clearly shows that the conductivity sites are the O-vacancy sites connected to form a member ring or a chain. To crudely model doping, we then shifted the Fermi-level towards the valence and conduction tail-regions where comparatively more states are available than the intrinsic case. We chose the model with $x = 1.3$ where we find more Si-rich regions. Figure 4.5, shows iso-surface plots for this model showing SPC values where values up to 0.04 times the highest values are displayed. The left and right plot corresponds to the valence-tail and the conduction-tail region respectively. Because the density of deep states is relatively low in the mid-gap region, the conduction zones are not well connected. By this “poor man’s doping” (moving the Fermi-level into tail states), we see enhanced conductivity.

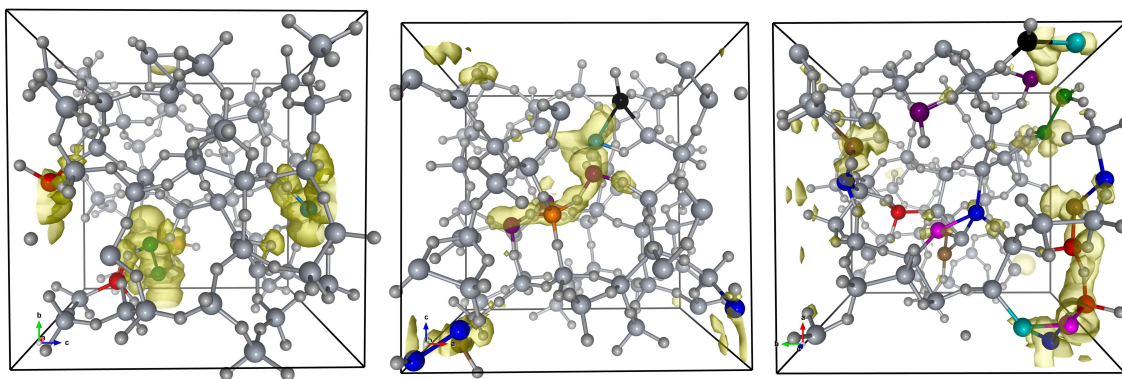


Figure 4.4: Iso-surface plots showing SPC (yellow colored blobs) for intrinsic $a\text{-SiO}_x$ models. From left to right representing for $x = 1.7, 1.5$ and 1.3 respectively. The Si atoms within the conduction-active region are color coded same as in right plot of Fig. ???. The conductivity values up to 0.04 times the highest value are considered in each plot. The remaining Si and O atoms are shown by gray color, O atom being represented by small spheres. The order of the magnitude of SPC is different in each plot.

The iso-surface plots (LEFT and RIGHT) in Figure 4.5 show that conduction-active path is primarily along the connected O-vacancy sites. It is apparently clear that not all

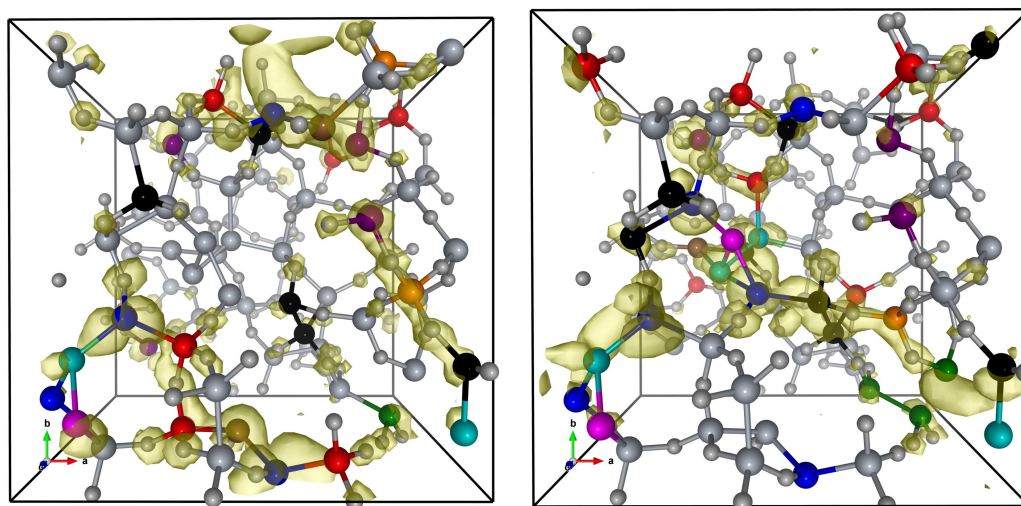


Figure 4.5: Iso-surface plots (yellow-colored blob) showing SPC for $x = 1.3$ model with shifted Fermi-level. LEFT: Valence-tail region (Fermi-level at ≈ -2.0 eV) and RIGHT: Conduction-tail region (Fermi-level at ≈ 2 eV). The cutoff up to 0.04 times the highest value is considered. Same color code description used in Figure 4.4.

O-vacancy sites form a connecting path, and therefore may only serve as charge trapping centers for electrons in the material. We observe the conduction through different vacancy clusters in the network for both p-doped and n-doped regions. The formation of di-vacancy and tri-vacancy clusters have been studied for silica where these vacancies exist in different forms as a member ring or as a vacancy chain [157]. Similar types of vacancy-sites have been observed in models where the conduction happens to be primarily through these vacancy cluster sites. The connected SPC path also follows Si atom with SiO_4 tetrahedral structure. This atom has distorted bond angle where the electrons could be trapped towards the wide angle side. For p-doped region(left plot in Figure 4.5), the distorted bond angle is 112° and for the n-doped region (right plot in Figure 4.5), the angle is 119° . As we have many O-vacancy sites in the network and these sites produce defect states in a wide range of energy in the band-gap, the conduction path is not unique. It depends upon choice of the Fermi-level which changes an occupancy of the electronic state, and therefore the conduction path. Figure 4.5 clearly shows that p-doping and

n-doping select out different parts of the network through which the conduction proceeds. The ability of switching the conduction path in the material due to the availability of O-vacancy sites in the network makes this material useful for creating PUFs.

4.4 Conclusions

In this chapter, we obtained atomistic models of a-SiO_x and showed that a-SiO_x models have complex bonding topology and the complexity increases with decreasing x . We find different tetrahedral structures in the models that represent different O-vacancy sites. We studied the electronic structure of the models by calculating electronic density of states and inverse participation ratio. We find that the electronic states near the Fermi-level are mostly attributed to Si-atoms, and these states are highly localized. We computed space projected conductivity and showed that the O-vacancy sites form major sites for electronic conduction. We also shifted the Fermi-level towards the valence and conduction-tail regions and showed that the conduction then follows different O-vacancy sites. This property also makes this material as a promising candidate for PUF devices.

5 ATOMIC PROPERTIES OF SODIUM SILICATE GLASSES USING BUILDING-BLOCK METHOD

The work presented in this chapter has been published as **Subedi, K. N., Botu, V., and Drabold, D. A.** *Atomic properties of sodium silicate glasses using building block method*, Phys. Rev. B 103, 134202 (2021)

5.1 Introduction

Sodium silicates $((\text{Na}_2\text{O})_x(\text{SiO}_2)_{1-x})$ are widely studied glasses that have established and potential applications for photonics, and bio-material engineering [159, 160, 161]. Despite these applications, the atomic structure of these glasses is still not well understood, owing to the large number of possible local bonding environments because of the complex composition. To fully exploit these glasses for practical applications, fundamental insight about the atomic structure is needed. Experimental work such as extended X-ray absorption fine structure (EXAFS) [162], magic angle spinning NMR (MAS-NMR) [163, 164], X-ray Photoelectron Spectroscopy (XPS) [165] and neutron diffraction [166] have determined many fingerprints of the structure. However the fingerprints alone are insufficient to determine the microstructure. Computer simulations have become the preferred route to understanding these materials at the nano-scale. Most classical molecular dynamics (MD) and *ab initio* molecular dynamics (AIMD) studies have used the quench-from-melt scheme [88] to obtain the $(\text{Na}_2\text{O})_x(\text{SiO}_2)_{1-x}$ structures. Within this method, properties of densified silicates and the impact of the cooling rates on structure of the silicates glasses have been discussed [167, 168]. With *a priori* experimental information available, methods like Force Enhancement Atomic Refinement (FEAR) [169] can be used which integrates experimental constraints with the classical MD or AIMD to obtain more realistic models.

A recent work by Zhou *et al.* [170] has employed the method to study $(\text{Na}_2\text{O})_{0.3}(\text{SiO}_2)_{0.7}$ glasses using classical MD. The study shows that FEAR models capture the medium range order particularly well. Most of the earlier and contemporary works on $(\text{Na}_2\text{O})_x(\text{SiO}_2)_{1-x}$ [171, 172, 173, 174] are primarily focused on the structural character of the materials, and have been successful when compared to experiments. Limited literature is available on electronic, optical, and mechanical properties [175, 176]. One interesting recent study of diffusion of the sodium silicate melt has been offered by Hung *et al.* [177] revealing that two different diffusion mechanisms could occur in such glasses. However to our knowledge, there are no studies on the thermal properties, especially thermal expansion coefficient (TEC), a key quantity for applications.

All amorphous materials have significant short range order, some form of medium-range order and ultimately no long range order. Thus, amorphous silicon has local order very reminiscent of diamond – bond angles are that are clustered around the tetrahedral angle and the great preponderance of bond lengths near the diamond nearest neighbor distance. Similarly, glassy phases of SiO_2 consist of interconnected Si-O tetrahedra that nevertheless have bond angle disorder in both Si-O-Si and O-Si-O angles (the latter again distributed around the tetrahedral angle). Other examples come to mind, such as the pyramidal units of As_2Se_3 . As the stoichiometry of the glass becomes complex including several elements, the building blocks are not necessarily so simple. It is with this background that we motivate the “building block” method [178]. Essentially, we try to identify the complex units, and perform a melt-quench simulation with that local order already built in. To enable this, a small cell (here, 30 atoms) of the correct stoichiometry of the glass and low energy is obtained by a thorough and extensive annealing/quenching process (easy to carry out because the cell is so small). The idea is that the actual glass is likely to exhibit such local order. The small cell is then used to build a larger cell from eight copies of the small cell formed into a cube with 240 atoms. A melt-quench method

is then carried out with this larger cell and remnants of this local order will persist even after a melt-quench process. This scheme has worked quite well in multinary glasses with complex ordering, and in particular seems to match or sometimes outperform conventional melt-quench method starting from random initial conditions, even for fairly extended simulations. The pair-correlation functions for the ternary glasses $\text{AsGe}_{0.8}\text{Se}_{0.8}$ and $\text{Ge}_2\text{As}_4\text{Se}_4$ have shown pleasing agreement with experiment [178]. A conceptually related but different version of the idea was presented by Ouyang and Ching, applied to amorphous Si_3N_4 glasses [179].

The rest of the chapter is organized as follows. In Section 5.2, we discuss the computational methodology for obtaining the models and the quasi-harmonic approximation. In Section 5.3, we describe structural, electronic, thermal and elastic properties in various subsections.

5.2 Methodology and Computational Details

5.2.1 Generation of Models using Building Block Method

We performed AIMD simulations using the VASP [83]. Three atomic models of $(\text{Na}_2\text{O})_x(\text{SiO}_2)_{1-x}$ were made with $x = 0.0, 0.1$ and 0.3 . For each model, we built a small “sub-unit cell” with 30 atoms at the known experimental density [180] and desired stoichiometry. The atoms were randomly placed with minimum separation of 2.1 \AA from each other. The temperature of the sub-unit cell was then increased to 3500 K in 4.5 ps and equilibrated at this temperature for 6 ps. The “hot liquid” was then cooled in successive steps followed by equilibration for a few ps to make the model representative of that temperature. Then it was cooled to 2000 K at a cooling rate of $2 \times 10^{14} \text{ K/s}$ followed by equilibration for 7.5 ps at the same temperature. The equilibrated sub-unit cell was further cooled to 1000 K at the same cooling rate followed by another equilibration for 7.5 ps. The sub-unit cell was then quenched to 300 K and equilibrated for

another 7.5 ps. The conjugate gradient (CG) method as implemented in VASP was then used to relax the sub-unit cell to optimize its energy. We obtained at least four such relaxed sub-unit cells by repeating the process and considered the sub-unit cell corresponding to the lowest energy termed as building block (BB) for the further calculations. Eight copies of the BB were used to prepare the starting configuration of the supercell that consists of 240 atoms. Following a similar scheme as used for the sub-unit cell, the super-cell was annealed at 2500 K⁷ for 7.5 ps and quenched to 300 K. The model was then equilibrated at 300 K for 7.5 ps. The equilibrated model at 300 K was finally optimized by performing zero-pressure relaxation. This resulted a non orthogonal cell and thus the density of the super-cell changes slightly (A variation in density was less than 3% for all models). A direct melt-quench model with $x = 0.3$ consisting of 240 atoms was also obtained for comparison. The initial structure was annealed from 300K to 3500 K in 4.0 ps and was equilibrated at 3500 K for 6ps. It was then cooled to 2000 K at the same cooling rate of 2×10^{14} K/s followed by equilibration for 6 ps at 2000 K. The model was further cooled to 1000 K at the same cooling rate and was equilibrated for next 4 ps. It was then quenched to 300 K followed by another equilibration for 4 ps. The model was finally optimized by performing zero-pressure relaxation. The direct melt-quench model was generated in ≈ 40 ps in terms of simulation time scale. The BB model took ≈ 65 percent of the time taken to generate the direct melt-quench model starting from the supercell of 240 atoms. This excludes simulation time to prepare the optimized BB of 30 atoms cell that is very cheap for computation. In all the above calculations, plane-wave basis sets were used with a kinetic energy cutoff of 400 eV. For CG and the zero-pressure relaxation steps, a cutoff of 520 eV was used. The generalized gradient approximations (GGA) of Perdew-Burke-Ernzerhof (PBE) [84] was used as the exchange-correlation functional. A single k-point (Γ) was used to sample the Brillouin zone. In all MD calculations, a time

⁷ α -SiO₂ model was annealed at 3000 K due to higher melting point compared to silicate models.

step of 1.5 fs was used and the temperature was controlled by a Nose-Hose thermostat [152, 153, 154]. Gaussian smearing with a width of 0.05 eV was used to represent the partial occupancies of the energy levels near the Fermi-level. Periodic boundary conditions were used throughout the calculations. The flow chart for the above discussed method is depicted in Figure 5.1.

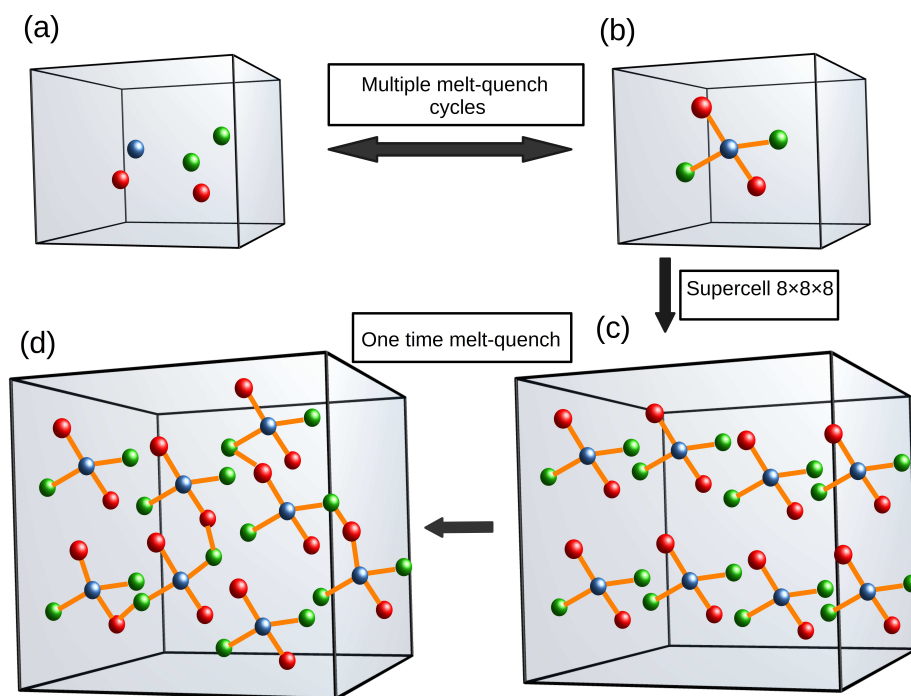


Figure 5.1: Schematic “flow chart” for building-block (BB) method. (a) Initial configurations of atoms in the sub-unit cell. (b) The sub-unit cell with minimum energy from several melt-quench cycles. (c) $8 \times 8 \times 8$ supercell formed from the optimized sub-unit cell. (d) The final model formed after one melt-quench cycle followed by relaxation.

5.2.2 Quasi-Harmonic Approximation

The thermal properties of the materials can be calculated within the framework of the quasi-harmonic approximation (QHA). In this approach, the volume dependence is used

to compute the approximate free energy $F(V, T)$ expressed as:

$$F(V, T) = E_0(V) + F_{vib}(T, V) \quad (5.1)$$

where E_0 is the ground state energy for a given volume V . In the DFT framework, E_0 is due to all electronic contributions to the Coulomb energy, and atomic energy contributions, according to the supplied PAW potentials. F_{vib} represents the vibrational contribution to the free energy. Once the phonon frequencies over Brillouin zone are known, F_{vib} is given by:

$$F_{vib} = \sum_{qj} \hbar\omega_{qj} \left[\frac{1}{2} + \frac{1}{\exp(\hbar\omega_{qj}/k_B T) - 1} \right] \quad (5.2)$$

where ω_{qj} is the phonon frequency for a given wave-vector q and the band index j . T , k_B and \hbar are the temperature, Boltzmann constant and Planck's constant.

To implement this, the relaxed supercell vectors were gradually scaled by factors from 0.97 to 1.03 with a step of 0.01 to obtain seven different configurations for both doped models. Structural optimization was then performed for each model at fixed volume with the convergence criteria of 10^{-6} eV and force 0.004 eV/Å for energy and force on each atom respectively. Static calculations were performed for each configuration to obtain $E_0(V)$ for both models. To obtain the phonon frequencies, the displacement of atomic coordinates by 0.015 Å was made along $\pm x$, $\pm y$ and $\pm z$ directions for each configuration. This led to several supercells slightly distorted from equilibrium geometry. Every such displacement configurations was then treated by a single-point computation and the force calculation was performed in VASP. The force-sets were collected from each displacement and the phonon frequencies were calculated on $31 \times 31 \times 31$ mesh grids. The contribution of the phonon frequencies was then included to obtain $F(V, T)$. The Helmholtz free energy was fitted with the Birch-Murnaghan equation of state (EOS) [181, 182]. Additional calculations were performed using phonopy [183], a convenient open source package for phonon-related computations.

5.3 Results and Discussion

5.3.1 Structural Properties

The structural topology of $(\text{Na}_2\text{O})_x(\text{SiO}_2)_{1-x}$ models were analyzed by calculating pair-correlation functions, structure factors, bond angle distribution functions, Q^n distributions and the coordination environment of each atomic species. The obtained results are compared with experiment and also with other available AIMD and classical MD results. The left subplot in Figure 5.2 displays total distribution function ($T(r)$)

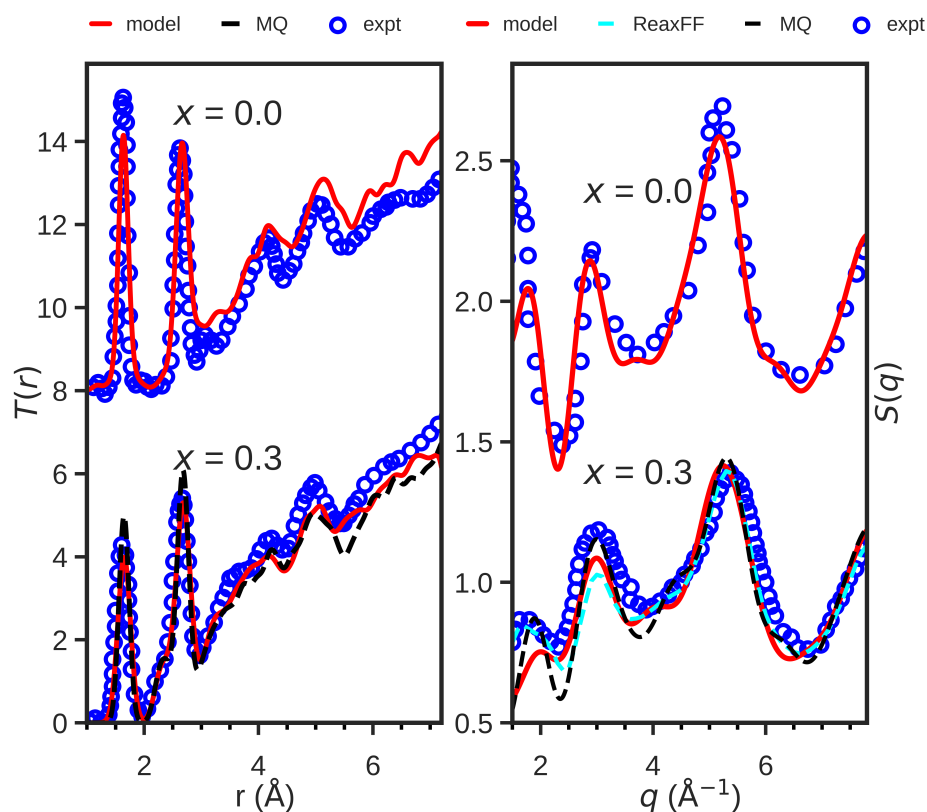


Figure 5.2: Total distribution function $T(r)$ and the Structure factor $S(q)$ for sodium silicate models with $x = 0.0$ and 0.3 respectively. The left and right subplots correspond to $T(r)$ and $S(q)$ respectively.

calculated from the models and obtained from the experiments for the undoped ($x = 0.0$)

and the “fully” doped case ($x = 0.3$). The experimental data for the undoped and the doped models were taken from reference [184, 185] respectively. $T(r)$ for the doped model with $x = 0.3$ shows excellent agreement up to the local range order ($\approx 3.4 \text{ \AA}$) and in pleasing agreement up to the medium range order (5-6 \AA). $T(r)$ for the doped-model ($x = 0.3$) obtained from direct melt-quench method is also displayed for comparison, and shows almost the same local ordering as the model obtained from building-block method. $T(r)$ for the undoped model shows very good agreement with the experiment up to 3 \AA and also accurately reproduces peaks in the medium range order. The structure factor ($S(q)$) for both models (undoped and the fully doped) were also calculated from the Fourier transform of the radial distribution function ($g(r)$), and are shown in the right subplot of Fig 5.2. $S(q)$ for both models show excellent agreements with the available experiments [186, 185] other than first sharp diffraction peaks (FSDP). $S(q)$ for the direct melt-quench model and using ReaxFF potential [187] with $x = 0.3$ are also displayed in the same subplot for comparison. The BB model shows slightly better agreement of the second peak with the diffraction experiment than the model using ReaxFF potential. The direct melt-quench model captures the second peak of $S(q)$ better than the BB model, nevertheless, overall agreement with the experiment is more or less similar. The large model using ReaxFF potential captures the FSDP of the neutron diffraction experiment. The small-sized models with 240 atoms provide poor description of correlations in intermediate or extended length scales. The origin of the FSDPs in silica and alkali silicates are attributed to many factors such as system size, composition, etc, and are discussed in references [188, 189, 190].

The left subplot in Figure 5.3 depicts $g(r)$ calculated from the models. For the model with $x = 0.0$, the first peak in $g(r)$ is located at $\approx 1.63 \text{ \AA}$ and corresponds to the Si-O correlations. $g(r)$ for the model with $x = 0.1$ shows that the first peak is slightly shifted towards the right at $\approx 1.64 \text{ \AA}$. For the model with $x = 0.3$, $g(r)$ shows that the first major

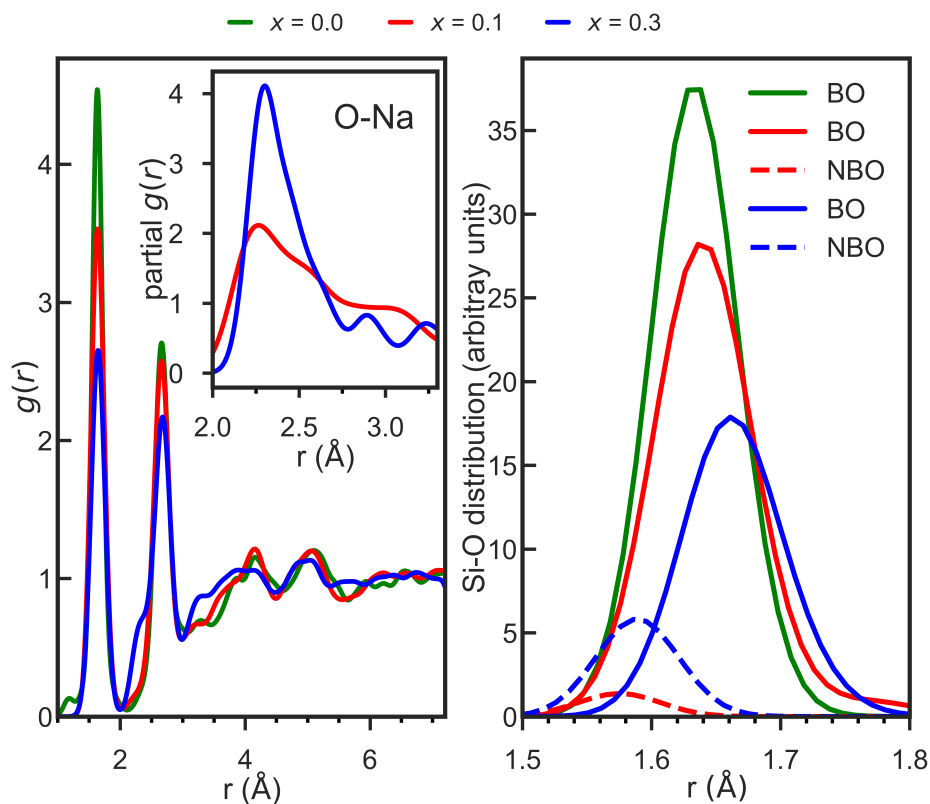


Figure 5.3: Radial distribution function $g(r)$ (left subplot) and bond length distribution of Si and O atoms (right subplot) for $(\text{Na}_2\text{O})_x(\text{SiO}_2)_{1-x}$ models. The inset in left subplot shows partial $g(r)$ attributed to Na-O correlations for the doped models. Solid and dashed lines in legends in right subplot correspond to bonding of Si with bridging oxygen (BO) and non-bridging oxygen (NBO) atoms respectively. NBO atoms here refer to O atoms that are linked to only one Si atom. BO atoms refer to O atoms that are not NBO atoms.

peak is further shifted to ≈ 1.65 Å. The calculated bond length for this model is closer to Si-O bond length obtained from EXAFS measurement ($1.66 \text{ Å} \pm 0.02 \text{ Å}$) than from neutron scattering measurements (1.62 Å) [162, 185]. For the silica structure, Si tetrahedra are connected by bridging oxygen (BO) atoms. Addition of a modifier to such structure depolymerizes the silica network by breaking the Si-BO-Si bonds and forming non-bridging oxygen (NBO) atoms. The concentration of such NBO atoms in the doped models were calculated to be 7.24% (10.53) and 34.56% (35.29) with $x = 0.1$ and 0.3 respectively where numbers inside the parenthesis correspond to theoretical percentages

assuming that each Na_2O creates 2 NBO atoms. The low percentage of NBO atoms for the model with $x = 0.1$ suggests that not all Na atoms depolymerize the network to form NBO atoms. The direct melt-quench model also contains the same number of NBO atoms as BB model with $x = 0.3$ showing very similar structural topologies between the models obtained from these two different methods. Earlier studies also obtained similar percentage of NBO atoms for the model with $x = 0.3$ [191, 171]. The fraction of BO and NBO atoms in the model with $x = 0.3$ is in agreement with results obtained using Electron Spectroscopy for Chemical Analysis technique [192]. From the left subplot in Figure 5.3, the intensity of the first peak in $g(r)$ is seen to decrease with increasing x . This is attributed to formation of fewer Si-BO bonds with increase in x and can be explained from the bond distribution of Si with O atoms. The bond distribution for the $(\text{Na}_2\text{O})_x(\text{SiO}_2)_{1-x}$ models were calculated and the contribution from Si-BO and Si-NBO bonds are displayed in right subplot of Figure 5.3. It can be seen that the intensity of Si-BO distribution decreases with increase in x that results decreasing intensity of the first peak in $g(r)$. The shift in peak position of Si-BO distribution towards larger distance results overall shift of the first peak in $g(r)$ with increasing x as observed in left subplot of Figure 5.3. The study by Sakka and Matusita [193] confirmed that the addition of Na_2O weakens the Si-O bond and results increase in Si-O bond length. This is consistent with our results and with the previous studies [185, 194]. The Si-NBO bonds peak at lower bond-length $\approx 1.59 \text{ \AA}$ and the intensity of peak grows with increase in x . So, for high concentration of Na_2O content in the silicates ($x \geq 0.5$), the first peak in $g(r)$ is expected to shift closer to the Si-NBO peak. For all models, the second peak at $\approx 2.66 \text{ \AA}$ is mainly due to O-O partial correlations. The calculated Si-Si correlations show peak at $\approx 3.06 \text{ \AA}$ for the doped models. The Si-Si bond length for the models is very close to that obtained from the neutron diffraction experiments for a- SiO_2 (3.08 \AA). Most of the DFT and classical MD studies predict the bond length of $\approx (3.11-3.19 \text{ \AA})$ for these glasses [195, 196]. For both

doped models, there exists a small minor peak at $\approx 2.3 \text{ \AA}$ which is due to the partial pair correlations from Na and O atoms forming a weak ionic bond. The inset in the left subplot of Figure 5.3 shows that the intensity of this peak is large for the model with $x = 0.3$. This peak is mainly attributed to Na-NBO correlations in the network. The Na-BO correlations are found towards larger distance and form a peak at $\approx 2.42 \text{ \AA}$. The bond angle

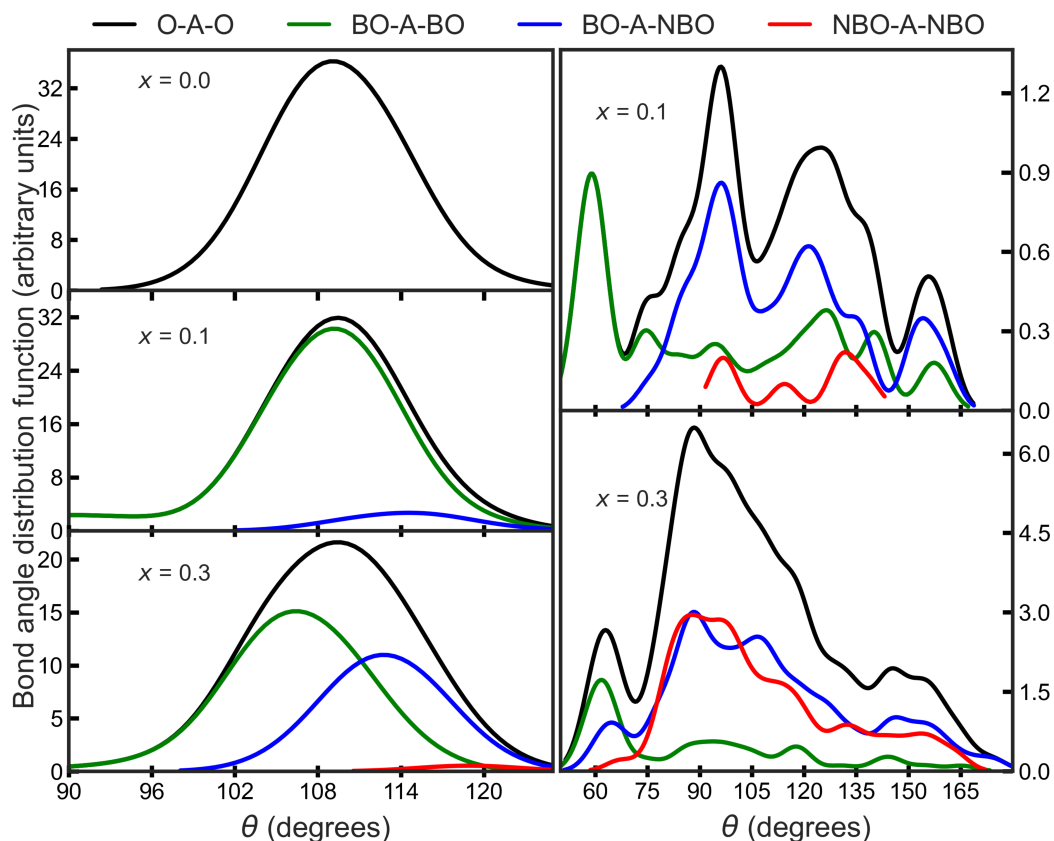


Figure 5.4: Bond angle distribution functions (BADF) for the $(\text{Na}_2\text{O})_x(\text{SiO}_2)_{1-x}$ models within the first cutoff distance for each atomic pairs showing the contribution of BO and NBO atoms. “A” in the legend refers to either Si or Na atom and black solid line corresponds to total distribution for each case. Left and right subplots correspond to O-Si-O and O-Na-O angles respectively. BO and NBO atoms used here are same as defined in Figure 5.3.

distribution function (BADF) for the models was also analyzed. Figure 5.4 displays

BADF corresponding to O-Si-O and O-Na-O angles. The left subplot in Figure 5.4 shows

BADF corresponding to O-Si-O angles. The BADF shows that O-Si-O angles for the models are approximately normally distributed. For the undoped model, O-Si-O bond angles form a peak at $\approx 108.9^\circ$ and has the full width half maximum (FWHM) of 12.5° . The neutron diffraction experiment by Grimley *et al.* found the peak at 109.7° with FWHM of 10.6° . The models obtained using potentials developed by VSL [197] and BKS [198] show that the O-Si-O angles form peak at 109.3° with FWHM of 12.2° and 108.6° with FWHM of 15.1° respectively [195]. For the doped models, it can be seen that the intensity of BO-Si-BO distribution decreases with increase in x and is attributed to formation of more NBO atoms in the network. The BO-Si-NBO angles are mostly formed towards right of the tetrahedral angle and these angles form a broader peak at $\approx 112.0^\circ$ for the model with $x = 0.3$. On the other hand, BO-Si-BO angles lie towards the left side and form a peak at $\approx 106.0^\circ$. There exists negligible contribution from NBO-Si-NBO angles to the distribution at $\approx 119.0^\circ$ for the model with $x = 0.3$. The presence of more NBO atoms in the network causes an overall shift of O-Si-O angles' peak towards high angle side. The BADF shows a peak at $\approx 109.5^\circ$ with FWHM of 12.0° and $\approx 109.7^\circ$ with FWHM of 15.0° for the models with $x = 0.1$ and 0.3 respectively. The study based on neutron diffraction experiment by Misawa *et al.* showed that the O-Si-O angle for $x = 0.0$ and 0.33 to be 109.1° and 109.3° respectively [194]. The classical MD simulations of the silicate glasses show peaks at slightly lower values for O-Si-O angles for the studied compositions [171, 191, 199, 200] The right subplot in Figure 5.4 depicts the BADF corresponding to O-Na-O angles for the doped models. The BADF for the model with $x = 0.1$ shows that there exists a first peak at $\approx 59.0^\circ$ and corresponds to BO-Na-BO angles. For the model with $x = 0.3$, the first peak in BADF lies at $\approx 62.9^\circ$ and is attributed to the BO-Na-BO, BO-Na-NBO, and NBO-Na-NBO angles with the smallest contribution from NBO-Na-NBO angles. Beyond the first peak, there exists another broad peak $\approx 88.5^\circ$ and near the far end forming a shoulder at $\approx 150.0^\circ$. The major broad angle formed at $\approx 88.5^\circ$

is attributed to almost equal contribution from NBO-Na-NBO and BO-Na-NBO angles. The shoulder formed at far side is also attributed to these angles. Such a broad peak does not exist for the model with $x = 0.1$ because of few available NBO atoms. There exists peaks $\approx 95.9^\circ$ and 121.8° that are mostly attributed to BO-Na-NBO angles. To understand

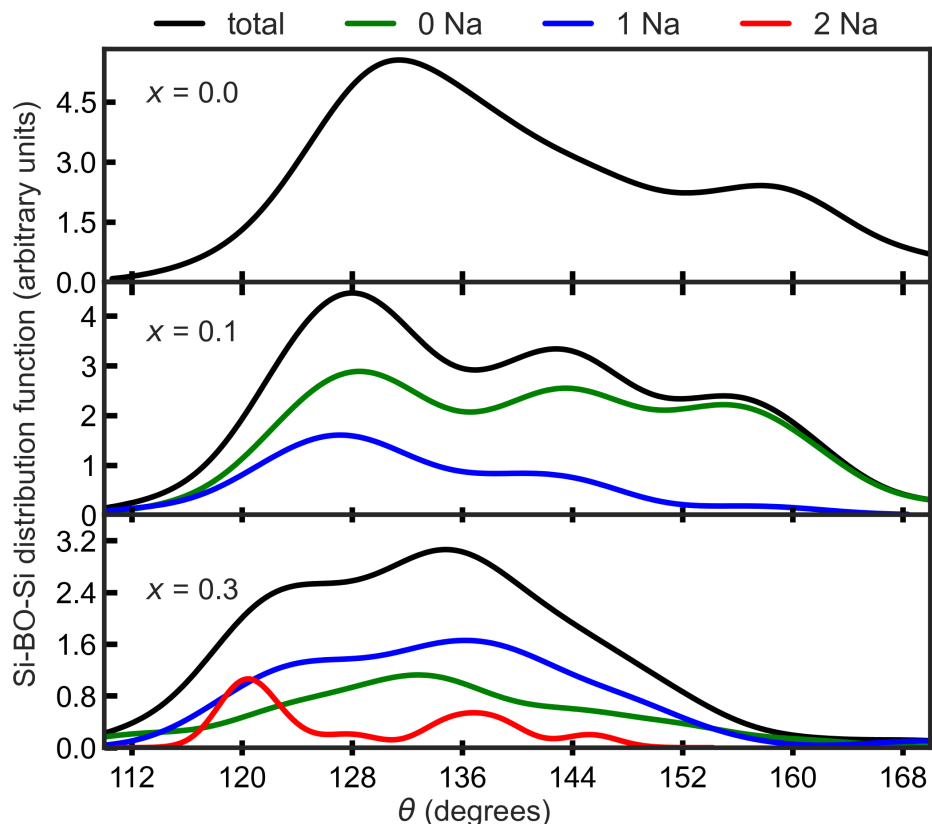


Figure 5.5: Bond angle distribution functions (BADF) corresponding to Si-BO-Si angles for the $(\text{Na}_2\text{O})_x(\text{SiO}_2)_{1-x}$ models shown by black lines in all subplots. The distribution decomposed based on number of modifier atom (Na) that are linked to BO atoms shown by the colored lines and labeled at the top of the figure for the doped models. The cutoff distance of 2.74 \AA for Na-O pairs is used.

how the tetrahedra are connected in the network, the BADF corresponding to Si-BO-Si angles were calculated and are displayed in Figure 5.5. Unlike the symmetric distribution obtained from most classical MD simulations [195, 201], our simulations show that the bond angles are more spread out with asymmetric shape of the distribution and are mostly

biased towards small angles. Donadio *et al.* [202] has also shown that for the model with $x = 0.25$, *ab initio* Car-Parrinello MD results the spread-out distribution compared to symmetric distribution from classical MD. The total BADF distribution for the undoped model shows a broad peak at $\approx 131.4^\circ$. The peak lies towards small angle compared to NMR secant model (142°) [203] and XRD model by Mozzi and Warren (144°) [204]. The latter model reproduces asymmetric distribution of Si-BO-Si angles. For the undoped and slightly doped ($x = 0.1$) models, bond angles near the extremes are observed at $\approx 158^\circ$ and 160° respectively. On the other hand, the distribution flattens in this region for the model with $x = 0.3$. Therefore, the distribution narrows and also shifts towards smaller angles with increasing x . This could be attributed to the increased Si-O lengths with addition of the modifier atoms [205]. The BADF corresponding to the doped models were decomposed based on linking of the BO atoms with neighboring Na atoms and are displayed by colored lines in Figure 5.5. It is observed that peaks at extremes are mostly attributed to the Si-BO-Si angles that are not linked to the modifier atoms. The Si-BO-Si angles with Na atoms as neighbors mostly form peaks towards small angles. For the model with $x = 0.3$, the Si-BO-Si angles linked with 2 Na atoms show a contribution to the peak very close to 120° but are absent for the model with $x = 0.1$. For the model with $x = 0.1$, there exists distinct peaks at $\approx 127.8^\circ$ and 142.8° . For the model with $x = 0.3$, there is a major peak $\approx 134.8^\circ$ and a shoulder towards the small angle side at $\approx 125.1^\circ$. It is observed that the contribution from the Si-BO-Si angles linked with 1 Na becomes higher with increase in x . A detailed analysis on Si-O-Si bond angle distribution for silica and sodium silicates can be found in reference [201]. To further understand the extent of depolymerization of the silica network due to the presence of Na_2O modifier, the Q^n distribution of Si atoms was calculated. Q^n is defined as Si atoms with n BO atoms. The NBO atoms are defined as O atoms that only form bond with one Si atom. The BO atoms here refer to O atoms that are not NBO atoms. For the model with $x = 0.0$, all O atoms

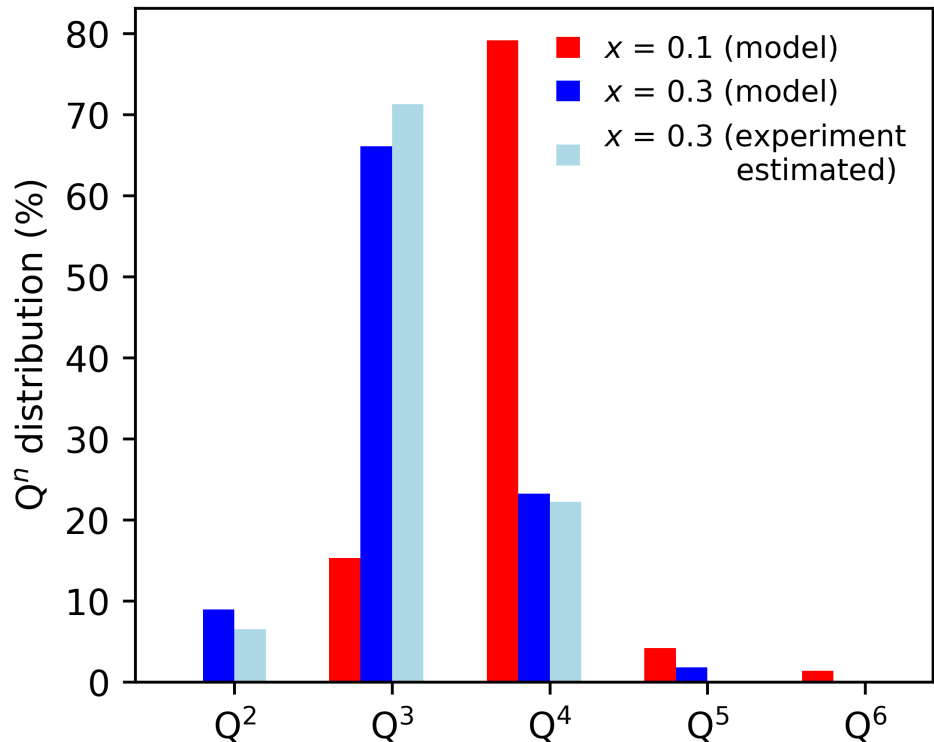


Figure 5.6: Q^n distribution for the doped models. The red and blue bars correspond to the calculated Q^n from the relaxed models with $x = 0.1$ and 0.3 respectively. The light blue bars correspond to the experimental data estimated for $x = 0.3$ from reference [1]. A cutoff distance of 1.94 \AA is used to define the bonds between Si and O atoms based on their covalent radii plus a tolerance factor of 0.10 \AA .

form BO atoms and constitute 100% of Q^4 distribution. The Q^n distribution for the doped models is displayed as histograms in Figure 5.6. The Q^n distribution obtained from the doped model with $x = 0.3$ shows agreement with estimated values obtained from the NMR experiment shown by light blue histograms [1]. For the model with $x = 0.1$, it is observed that the structure has majority of Q^4 (79.17%) and Q^3 (15.28%) and are displayed as red colored histograms in Figure 5.6. A few Q^5 are observed in both doped models and a Q^6 is observed for the model with $x = 0.1$. The contributions from Q^5 and Q^6 are very small, and could be artifacts of high cooling rate used to quench the liquid phase to obtain the glass models. These are also sensitive to the cutoff used to define bond-length between Si

and O atoms. For model with $x = 0.3$, the majority are Q^3 (66.07%) and Q^4 (23.21%). Simulated silicate glasses using classical MD or combined with DFT show similar results for the model with $x = 0.1$ whereas significant deviation of Q^3 values are observed for the model with $x = 0.3$ [171, 206, 207].

Table 5.1: Average Coordination Number (n) and its Distribution Among Each Atomic Pairs $n()$, where () is Filled by the Corresponding Atomic Species. The Coordination is Counted Only if the Distance for Each Atomic Pair is no More than the Sum of Their Covalent Radii Plus a Tolerance Factor of 0.1 \AA . Covalent Radii of 1.11 , 0.73 and 1.66 \AA was Taken for Si, O and Na Atoms Respectively.

Na ₂ O content (x)	Atom	n	$n(Si)$	$n(O)$	$n(Na)$
0.0	Si	3.93	0.00	3.93	–
	O	1.96	1.96	0.00	–
0.1	Si	4.07	0.00	4.07	0.00
	O	2.17	1.93	0.00	0.24
	Na	2.5	0.0	2.25	0.25
0.3	Si	4.11	0.00	4.02	0.09
	O	2.73	1.65	0.00	1.07
	Na	4.98	0.10	3.04	1.83

In order to understand the local bonding environments of these glasses, the average coordination number for different atomic pairs were calculated. To describe the coordination, the covalent radius for each atom was used. So, the distance between atoms which is no more than the sum of covalent radii of the atomic pairs within the tolerance of 0.1 \AA only contribute to the coordination. The detailed coordination number for the doped glasses are shown in Table 5.1.

Table 5.1 shows that the average coordination of each atom type is x -dependent. It is clear that the mean coordination of each atom increases with increase in x . For the doped

models, we find a significant increase in the average coordination of Na with increase in the Na_2O content. The coordination number was calculated to be 2.5 and 4.98 for models with $x = 0.1$ and 0.3 respectively.

5.3.2 Electronic Properties

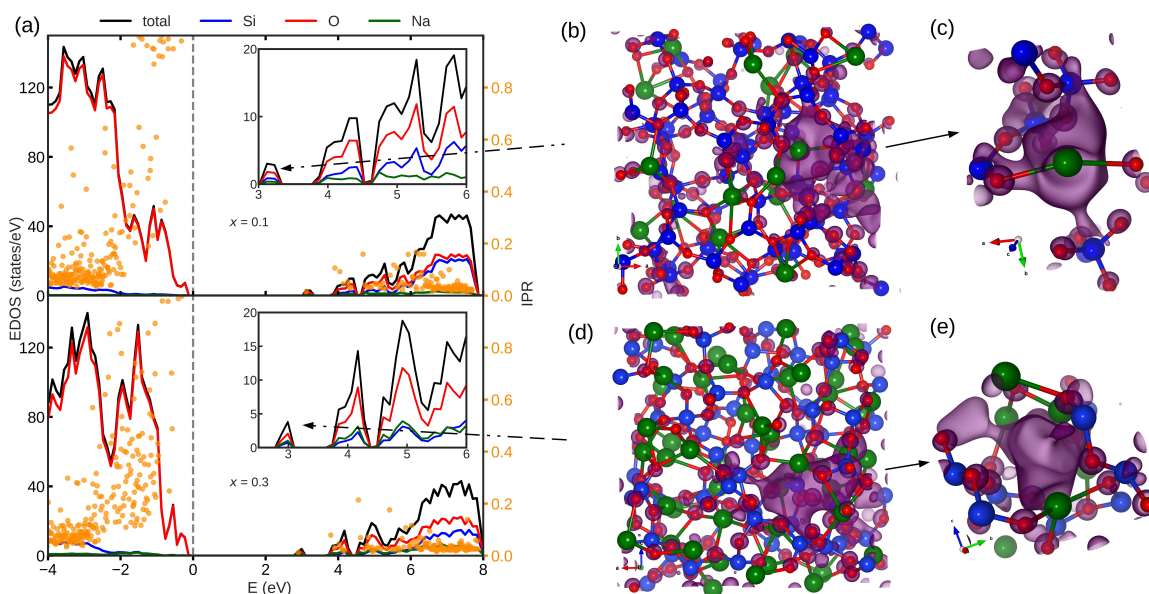


Figure 5.7: (a) Total and projected electronic density of states (EDOS), and the inverse participation ratio (IPR) for $(\text{Na}_2\text{O})_x(\text{SiO}_2)_{1-x}$ models. (b) and (d) Partial charge density for the defect state in the gap shown as iso-surface (purple colored blobs) plots for the doped models with $x = 0.1$ and 0.3 respectively. (c) and (e) show close look of the defect sites in (b) and (d) respectively. Atoms color match with the legends in (a).

For the doped models, as discussed in Section 5.3.1, the Na atoms modify the structural topology of the glass essentially by breaking the Si-BO-Si and forming NBO atoms; the effect escalates with increase in Na_2O content. This in turn induces a variation of electronic structure of the glass. To understand this, quantities like the electronic density of states (EDOS) were computed, and the localization of the states was gauged by the values of IPR.

The sub-plots in Figure 5.7a show the total EDOS and the EDOS projected on atomic sites for the doped models. An electronic Kohn-Sham band gap of ≈ 3.96 eV and ≈ 3.82 eV was observed for models with $x = 0.1$ and 0.3 respectively. Quite large band gaps for glasses with the same composition has been reported by Murray *et al.* [208] and are 5.82 and 4.61 eV for models with $x = 0.1$ and 0.3 respectively. For the doped models, the top of the valence edge derives from NBO atoms and the bottom of the conduction band is from more or less all three species. The EDOS projected on atomic sites shows that the contribution of the Na ions in the conduction band increases with x that is apparent from the inset plots in Figure 5.7a. The IPR values (labeled on right y-axis in Figure 5.7a) show that states near the valence edge are highly localized and are attributed to the non-bridging O-2p orbitals. The energy range of localization is slightly deeper into the valence band for the model with $x = 0.3$ than with $x = 0.1$ which is possibly due to comparatively more NBO atoms. For both doped models, defect states appear in the gap around 1 eV below the conduction edge and are shown by arrowheads in the inset plot in Figure 5.7a. The charge densities corresponding to these defects were then determined and are displayed as isosurface plots (purple blobs) in Figure 5.7b and Figure 5.7d for models with $x = 0.1$ and 0.3 respectively. The isosurface plots show that the charge is mostly spatially localized in few atomic sites for both models. For the model with $x = 0.1$, the maximum charge density is attributed to Na atom towards the O-deficient center as shown in Figure 5.7c. The charge density is extended towards larger angles ($\approx 113^\circ$) of SiO_4 tetrahedral unit. These sites serve as intrinsic charge carrier sites in the network. For the model with $x = 0.3$, the charge density is bounded by Na atoms towards the O-deficient sides of the network. Figure. 5.7e shows the particular region within the supercell where the charge density is localized in space surrounded by 4 Na atoms. Increase in Na_2O content in the glass could lead to more such defect states near the conduction tail and could be engineered for optical applications.

5.3.3 Thermal Properties

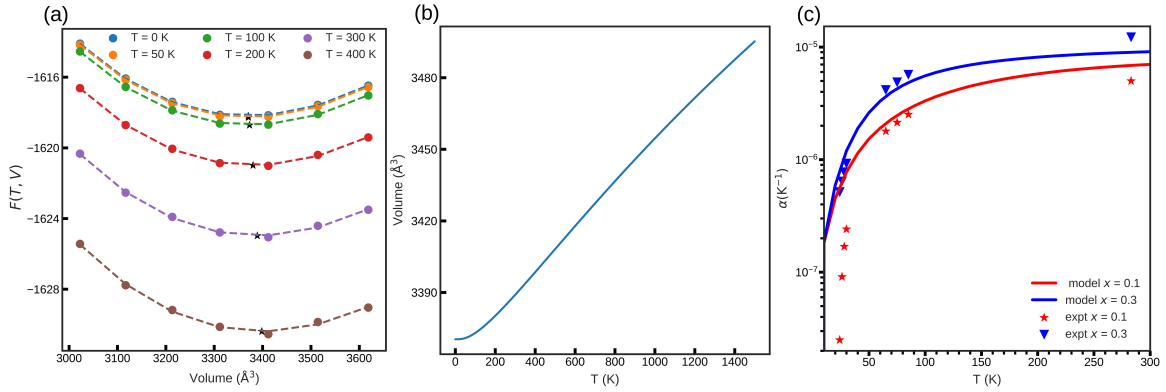


Figure 5.8: (a) Helmholtz free energy obtained for seven different volumes at selected temperatures shown by the filled circles. The dashed lines represent the fit to the EOS. The black star symbols represent the Gibb's free energy. (b) The volume vs temperature plot for the doped model with $x = 0.3$. (c) Linear thermal expansion coefficient (LTEC) for both doped models.

In this section, the thermal properties of the doped models are studied by calculating the linear thermal expansion coefficients (LTEC) and specific heat capacities at constant pressure (C_p). These properties are calculated using quasi-harmonic approximation approach discussed in section 5.2.2.

The temperature-dependent Helmholtz free energy $F(T, V)$ was obtained as discussed in section 5.2.2, and is plotted for one of the doped models with $x = 0.3$ shown by filled circles in Figure 5.8a. The dashed lines represent the fit using the Birch-Murnaghan equation. The minimum volume from each curve was determined (indicated by the star symbol in Figure 5.8a) and these volumes are plotted against the temperature in Figure 5.8b. The volume thermal expansion coefficient was obtained using the relation:

$$\beta(T) = \frac{1}{V(T)} \frac{\partial(V(T))}{\partial T} \quad (5.3)$$

The linear thermal expansion coefficient (LTEC), denoted by α , was calculated assuming $\alpha = \frac{1}{3}\beta$ and compared with the experiment [209] that are measured at low temperatures.

Figure 5.8c shows the calculated and the experimental values of α for both doped models. The calculated values of α for model with $x = 0.3$ are in excellent agreement with the experimental values. The calculated value of α was determined to be $9.0 \times 10^{-6} \text{ K}^{-1}$, close to the experimental value $1.2 \times 10^{-5} \text{ K}^{-1}$ at 283 K. For $x = 0.1$, the LTEC values are about an order smaller than the experimental values at very low temperature but are closer to the experiment from around 80 K to room temperature. The calculated value of α was found to be $6.9 \times 10^{-6} \text{ K}^{-1}$ compared with the experimental value $5.0 \times 10^{-6} \text{ K}^{-1}$ at 283 K.

From $F(T, V)$, the Gibbs free energy $G(T, p)$ at given temperature and pressure was obtained through the transformation,

$$G(T, p) = \min_V [F(T, V) + pV] \quad (5.4)$$

From $G(T, p)$, the thermal properties such as specific heat at constant pressure (C_p) can be calculated. Figure 5.9 shows the specific heat capacity at zero pressure for both doped models. The C_p for the model with $x = 0.3$ is slightly higher compared to $x = 0.1$ throughout the provided temperature range. The results for the model with $x = 0.3$ was compared with the closest available experimental results with $x = 0.33$ and are shown by scattered plots in Figure 5.9. It can be seen that the results are in close agreement. The heat capacity for the sodium silicate glasses obtained from the classical MD also shows similar result [210]. For these doped models, the calculated values of C_p at 300 K were obtained to be 51.86 and 47.38 $\text{Jmol}^{-1} \text{ K}^{-1}$ with $x = 0.3$ and 0.1 respectively. The experimental value for $x = 0.33$ at this temperature is 52.50 $\text{Jmol}^{-1} \text{ K}^{-1}$.

5.3.4 Elastic Properties

The elastic properties for the models are studied from the elastic tensor (C_{ij}). C_{ij} can be obtained by distorting the lattice vectors and relaxing all of the internal parameters to minimize the total energy. The distortion of the lattice vectors results in a change in total

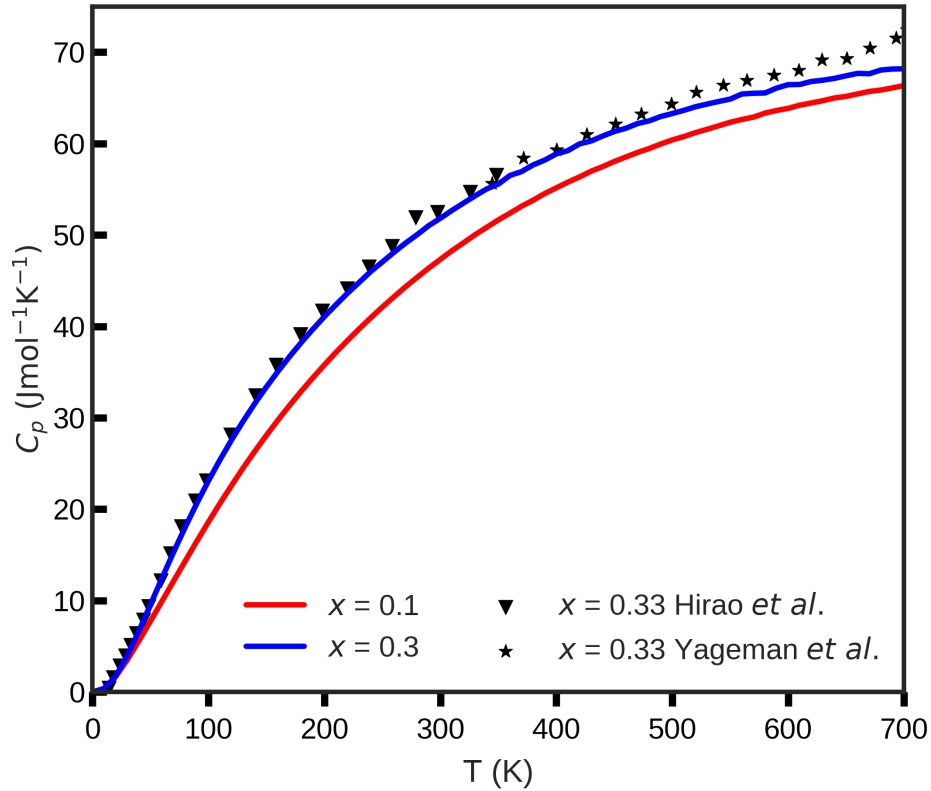


Figure 5.9: Specific heat capacity at constant pressure (C_p) for $(\text{Na}_2\text{O})_x(\text{SiO}_2)_{1-x}$ models with $x = 0.1$ and 0.3 shown by solid lines and the experimental values for $x = 0.33$. The triangle and star symbols correspond to the values taken from references [2, 3].

energy by amount [211]:

$$E(e_i) = E_0 - P(\Omega)\Delta\Omega + \Omega \sum_{i=1}^6 \sum_{j=1}^6 C_{ij}e_i e_j / 2 + O[e_i^3] \quad (5.5)$$

where Ω is the volume of the undistorted lattice, $P(\Omega)$ is the pressure of the undistorted lattice at the volume Ω , $\Delta\Omega$ is the change in the volume of the lattice due to the acting strain and the third order term of e_i has been neglected. Altogether, there are 21 independent C_{ij} in Eq. 5.5. However, symmetry reduces the number of independent C_{ij} depending upon the crystal structure. By the means of the C_{ij} and the compliance tensor, s_{ij} (C_{ij}^{-1}), the bulk modulus (K) and shear modulus (G) can be expressed as [212]:

$$9K_V = (C_{11} + C_{22} + C_{33}) + 2(C_{12} + C_{23} + C_{31}) \quad (5.6)$$

$$15G_V = (C_{11} + C_{22} + C_{33}) - (C_{12} + C_{23} + C_{31}) + 3(C_{44} + C_{55} + C_{66}) \quad (5.7)$$

$$1/K_R = (s_{11} + s_{22} + s_{33}) + 2(s_{12} + s_{23} + s_{31}) \quad (5.8)$$

$$15/G_R = 4(s_{11} + s_{22} + s_{33}) - 4(s_{12} + s_{23} + s_{31}) + 3(s_{44} + s_{55} + s_{66}) \quad (5.9)$$

where C_{ij} are being written in according to Voigt notation [213]. The expressions for K and G with subscripts V and R in Eqns. (5.6-5.9) refer to the Voigt and Reuss approaches of determining the Bulk and Shear modulus respectively. The Voigt approach provides an upper limit and the Reuss approach provides the lower limit.

The stress tensor, C_{ij} for each doped model was obtained from VASP using a strain of 0.015 Å. The diagonalization of the matrix C_{ij} was then performed that yielded positive eigenvalues satisfying the elastic stability. The calculated bulk and shear moduli are presented in table 5.2 and are compared with experiment [214].

Table 5.2: Elastic Properties Obtained From $(\text{Na}_2\text{O})_x(\text{SiO}_2)_{1-x}$ Models

Na ₂ O content	Bulk modulus (GPa)			Shear Modulus(GPa)		
	K_V	K_R	K_{avg}	G_V	G_R	G_{avg}
0.0 Model	34.02	32.25	33.18	25.28	22.81	24.05
Expt	36.10			31.25		
0.1 Model	27.92	23.48	25.70	25.53	22.28	23.91
Expt	33.95			27.68		
0.3 Model	34.56	33.75	34.16	22.62	21.37	21.99
Expt	39.03			23.80		

From table 5.2, it can be seen that the calculated values of shear and bulk moduli using the Voigt approach are closer to the experimental data for all the models. But for better comparison with the experiment, the average of the values from both Voigt and

Reuss approaches was performed. These quantities are denoted as K_{avg} and G_{avg} for bulk and shear modulus respectively in table 5.2. We see that the calculated values of G_{avg} for both doped models are close to the experimental values with maximum deviation of 3.77 GPa. For the undoped model, we find the deviation of 7.20 GPa from the experiment. The calculated K_{avg} for the undoped and $x = 0.3$ models are also closer to the experimental value (deviation < 5 GPa). For the model with $x = 0.1$, the calculated K_{avg} was found to be quite low compared with the experimental value (deviation of 8.25 GPa). The discrepancies of similar range and even higher than the tabulated values have been reported in literature [215, 216, 217, 218].

5.4 Conclusions

The realistic models of $(\text{Na}_2\text{O})_x(\text{SiO}_2)_{1-x}$ glasses were obtained using the building block method that potentially suits for predicting the structure of the homogeneous glasses. Structural properties of the models were explored by studying the correlation functions such as pair correlation functions, structure factors, bond angle distribution functions, Q^n distributions and the local coordination analysis. The pair correlation functions calculated from the obtained models show that the BB method correctly predicts the local structure of the glasses and also captures the signature of the medium range order. The Si-O bond length is found to be increased with increase in Na_2O content for the studied concentrations and is consistent with the previous studies. The bond angle distribution functions corresponding to Si-BO-Si angles are found to be narrower and O-Si-O angles shift slightly towards the higher angle with increase in modifier concentration. The Q^n distribution for the fully doped model shows good agreement with the NMR studies. The electronic density of states for the doped glasses shows the presence of defect states in the band gap towards the conduction tail and are mostly localized at under-coordinated Na atoms in the network. The thermal properties of the

doped models were computed on the basis of quasi-harmonic approximation. The calculated values of linear thermal expansion coefficient show satisfactory agreement with the experiment. The specific heat capacity for the doped models were calculated and the fully doped model shows that the results are in agreement with the experiment. The elastic properties of the doped models were also studied by calculating the bulk and shear moduli, and these values also satisfactorily agree with the experimental values.

6 CONCLUSIONS

In this dissertation, we provided a novel method to project electronic conductivity onto real-space grids using the Kubo-Greenwood formula. We also improved the understanding of the method by diagonalizing the conduction matrix and expressing the total conductivity and conduction path in terms of conduction-matrix eigenvalues and eigenvectors. In the second chapter, we implemented the method from outputs of DFT calculations and studied transport in different electronic materials (insulating to mixed systems). For a low density a-carbon, we showed that both sp and sp^2 sites form major conduction pathways for electronic conduction. For a-silicon, we find that the SPC shows a special weight for atoms with bond lengths shorter than 2.32 Å and longer than 2.43 Å. For l-Si, we find that the SPC is mostly uniform throughout the cell representing its metallic nature. We reveal that the majority of conduction sites in l-Si are Si atoms with 4-fold, 5-fold, 6-fold and 7-fold coordinated. We provided spectral representation of conduction eigenvalues for insulating/conducting (a-Si/a-C) and the metallic (c-Al) systems. We find that the conduction matrix always has a huge null space with a large weight of conduction eigenvalues is close to zero, and only handful of eigenvectors are sufficient to determine the conductivity path for insulating/semi-conducting systems. On the other hand, for metallic systems, there exists a spectral tail in the density of states and more eigenvectors are needed to accurately obtain the conductivity path.

In the third chapter, we described atomistic modeling of one of the promising CBRAM materials: copper doped aluminum oxide. In this work, we varied Cu concentration in aluminum oxide and studied the variation in atomic properties. Our study reveals that Cu atoms segregate and form cluster in such ionic host. From the electronic structure of $Al_2O_3:Cu$ models, we find that the mid-gap states within the band-gap of a- Al_2O_3 correspond to Cu atoms and the gap fills uniformly as Cu concentration increases. The Bader-charge analysis of the model with 20% Cu shows that majority of Cu atoms

that form a cluster/chain like structure in the network carry net charge close to zero. We also find a few Cu atoms in different charge states depending upon their local environment. We reveal that the connectivity of Cu atoms plays crucial role in closing and opening of HOMO-LUMO gap and have direct consequence in electronic conductivity. Besides electronic structure, we studied lattice dynamics of the models by computing vibrational DOS and vibrational IPR. We find that lower vibrational modes are mostly due to Cu atoms. On the other hand, the higher vibrational modes are localized on O-atoms.

In the fourth chapter, we simulated a-SiO_x (a promising resistive memory material) with $x = 1.7, 1.5$ and 1.3 . Our study shows that the material has complex structural topology with decreasing x . In other words, there exists different structures other than SiO₄ and results in more O-deficient sites in the network. We find that the transport in a-SiO_x is mainly along the connected O-vacancy sites. We showed that one can switch the conductivity path in this material by either shifting the Fermi-level or switching the frequency. We therefore suggest that this material as a promising candidate for PUF applications.

In the last chapter, we implemented a building-block method to model sodium silicate glasses. The method is computationally less expensive and also provides the correct local chemistry of these glasses. We computed pair distribution functions and structure factors for the models and compared with experiments. The detailed analysis of the structure of these glasses show that Si-O bond length increases with increase in modifier (Na₂O) content in the glass. From the bond angle distribution functions, we find that Si-BO-Si angles become narrower and O-Si-O angles are shifted towards higher angles with increasing modifier content. From the electronic structure, we find that the localized defect states near the conduction tail region in the EDOS is due to under coordinated Na atoms in the network. We studied thermal properties of the models by calculating linear thermal expansion coefficients within quasi-harmonic approximation

and compared with the experiments. Our results yield a good agreement with experiment making the method a suitable tool to model such kinds of multi-component glasses.

6.1 Future Work

The SPC method is a general tool to explore materials. So far, we have applied it to only few materials. In one of the ongoing projects, we are studying the effect of lattice defects to conduction in metals. For this, we have considered vacancies and grain boundaries in crystalline Al and Cu. Subplots a), b) and c) in Figure 6.1 show 2D gray-scale images of SPC with a single vacancy in 500 atom cell of c-Al projected along 010, 110 and 111 crystallographic planes respectively. One can see that the spatial distribution of conduction around the vacancy is slightly anisotropic and its reduction has a characteristic range. To estimate the recovery length of conduction, we obtained the SPC as a function of distance away from the vacancy along different directions (shown by colored lines in subplots a), b) and c) in Figure 6.1) and are displayed as subplots d), e) and f) in Figure 6.1. For most of the orientations, we find that the conduction is most likely recovered within 4 Å from the vacancy. We also find that the recovery length can be as long as up to 6 Å along the directions with $(\theta, \phi) = (45^\circ, 125^\circ)$ and $(45^\circ, 145^\circ)$ shown by green and magenta colored lines in subplots d) and e) of Figure 6.1 respectively.

In the other project, we are collaborating with Dr. Keerti Kappagantula and her experimental group at Pacific Northwest National Laboratory to explore conduction mechanisms in copper-Graphene composites. Experimental evidences have shown that the conductivity of these materials can exceed good quality Cu itself [219, 220]. In this work, we have obtained the initial representative models of copper-Graphene composite in two different ways: first inserting a small bit of Graphene (up to 7 rings) into a single FCC Cu and second placing an infinite Graphene sheet along selected grain boundaries. In the former case, we are studying the structural topology and transport properties for these

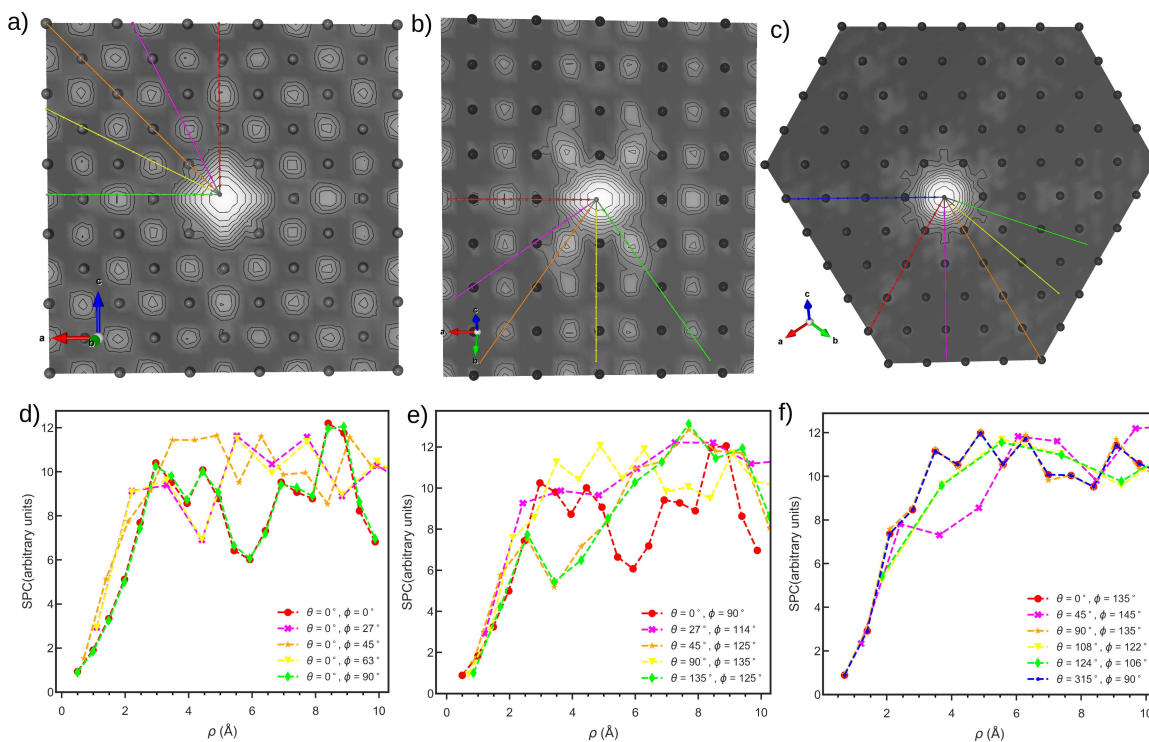


Figure 6.1: a), b), c): Conductivity projected on grids closest to crystallographic planes 010, 011 and 111 containing a vacancy as a 2D gray scale plot. The magnitude of conductivity increases from white to black. The colored lines with small spheres are just for guide to an eye representing different directions from the vacancy. d), e), f): Variation of conductivity with distance from the grid closest to the vacancy along different directions on planes 010, 011 and 111 respectively. θ and ϕ refer to the polar and azimuthal angles respectively. Color of legends in d), e) and f) match with the lines shown in a), b) and c) respectively.

models. We are also obtaining the temperature dependence of conductivity for these models. In the latter case, we are exploring the contribution of Graphene to the conductivity by varying copper-Graphene distance for a selected grain boundaries. Our preliminary results show that the conductivity calculated in the direction normal to the grain boundary improves with decreasing copper-Graphene distance from 3.2 Å to 2.2 Å. We find that the contribution of carbon atoms in Graphene to the conduction increases with decreasing the copper-Graphene distance.

Amorphous carbon and battery materials are other promising candidates where the method can be helpful. a-C can be designed with varying density that leads to different sp , sp^2 and sp^3 configuration sites [85]. So, understanding conduction pathways for different density of a-C would be important depending upon the desired application. Similarly, identifying good/bad conduction sites in the electrolyte, electrode or electrolyte/electrode interfaces in batteries would be helpful to optimize them or explore new materials for the devices.

Despite the method being successful to compute conduction pathways, extracting quantitative value of conductivity is not easy. The sparseness of the Kohn-Sham eigenvalues due to finite size effects makes precise estimate challenging. To get a better estimate, the smearing width of Gaussian distribution function has to be chosen carefully based on the splitting of the Kohn-Sham eigenvalues. The other factor that affects the conductivity is the fictitious temperature used in Fermi-Dirac distribution function to smear the occupancy. Also, there are other factors that arise from the DFT calculations rather than the method itself. For example, the static lattice computations excludes electron-phonon coupling that affect electron transport in the materials. Also, the choice of the exchange potential used during the static calculations plays role where one would expect better results when used with hybrid functionals.

REFERENCES

- [1] Maekawa, H., Maekawa, T., Kawamura, K., and Yokokawa, T. *Journal of Non-Crystalline Solids* **127**(1), 53 – 64 (1991).
- [2] Hirao, K., Soga, N., and Kunugp, M. *Journal of the American Ceramic Society* **62**(11-12), 570–573 (1979).
- [3] Yageman, V. D. and Matveev, G. M. *Fiz. Khim. Stekla* **8**(2), 238–245 (1982).
- [4] Lundstrom, M. *Science* **299**(5604), 210–211 (2003).
- [5] Jeong, M., Doris, B., Kedzierski, J., Rim, K., and Yang, M. *Science* **306**(5704), 2057–2060 (2004).
- [6] Simmons, J. G. and Verderber, R. R. *Radio and Electronic Engineer* **34**(2), 81–89 (1967).
- [7] Wang, L.-G., Qian, X., Cao, Y.-Q., Cao, Z.-Y., Fang, G.-Y., Li, A.-D., and Wu, D. *Nanoscale research letters* **10**, 135–135 (2015).
- [8] Belmonte, A., Kim, W., Chan, B., Heylen, N., Fantini, A., Houssa, M., Jurczak, M., and Goux, L. In *2013 5th IEEE International Memory Workshop*, 26–29, (2013).
- [9] Chang, T.-C., Chang, K.-C., Tsai, T.-M., Chu, T.-J., and Sze, S. M. *Materials Today* **19**(5), 254 – 264 (2016).
- [10] Waser, R., Dittmann, R., Staikov, G., and Szot, K. *Advanced Materials* **21**(25-26), 2632–2663 (2009).
- [11] Xu, X., Liu, J., and Anantram, M. P. *Journal of Applied Physics* **116**(16), 163701 (2014).
- [12] Belmonte, A., Celano, U., Degraeve, R., Fantini, A., Redolfi, A., Vandervorst, W., Houssa, M., Jurczak, M., and Goux, L. *IEEE Electron Device Letters* **36**(8), 775–777 (2015).
- [13] Chen, W., Tappertzhofen, S., Barnaby, H. J., and Kozicki, M. N. **39**(1-4), 109–131 (2017).
- [14] Chen, W., Tappertzhofen, S., Barnaby, H. J., and Kozicki, M. N. *Journal of Electroceramics* **39**(1-4), 109–131 (2017).
- [15] Gu, T., Tada, T., and Watanabe, S. *ACS Nano* **4**(11), 6477–6482 (2010).
- [16] Zaffora, A., Cho, D., Lee, K., di quarto, F., Waser, R., Santamaria, M., and Valov, I. *Advanced Materials* **29** 10 (2017).

- [17] Petzold, S., Miranda, E., Sharath, S. U., Muñoz-Gorriz, J., Vogel, T., Piros, E., Kaiser, N., Eilhardt, R., Zintler, A., Molina-Luna, L., Suñé, J., and Alff, L. *Journal of Applied Physics* **125**(23), 234503 (2019).
- [18] Kund, M., Beitel, G., Pinnow, C.-U., Rohr, T., Schumann, J., Symanczyk, R., Ufert, K., and Muller, G. In *IEEE International Electron Devices Meeting, 2005. IEDM Technical Digest.*, 754–757, (2005).
- [19] Lee, D., Oukassi, S., Molas, G., Carabasse, C., Salot, R., and Perniola, L. *IEEE Journal of the Electron Devices Society* **5**(4), 283–287 (2017).
- [20] Skorobogatov, S. *Journal of Hardware and Systems Security* **2**(4), 314–321 (2018).
- [21] Gao, Y., Al-Sarawi, S. F., and Abbot, D. *Nature Electronics* **3**(25-26), 81–91 (2020).
- [22] Grubel, B. C., Bosworth, B. T., Kossey, M. R., Sun, H., B., C. A., Foster, M. A., and Foster, A. C. *Optics express* **25**(11), 12710–12721 (2017).
- [23] Moon, D.-I., Rukhin, A., Gandhiraman, R. P., Kim, B., Kim, S., Seol, M.-L., Yoon, K. J., Lee, D., Koehne, J., Han, J.-W., and Meyyappan, M. *ACS Applied Electronic Materials* **1**(7), 1162–1168 (2019).
- [24] Kozicki, M. and Chen, W. <https://patents.google.com/patent/US11127694B2/en>, (2021).
- [25] Ferraris, M., Milanese, D., Contardi, C., Chen, Q., and Menke, Y. *Journal of Non-Crystalline Solids* **347**(1), 246–253 (2004).
- [26] Ferraris, M., Milanese, D., Menke, Y., Chen, Q., Chiesa, M., and Giamello, E. *Journal of Non-Crystalline Solids* **352**(21), 2267–2278 (2006).
- [27] Tilocca, A. *Proceedings of the Royal Society A: Mathematical, Physical and Engineering Sciences* **465**(2104), 1003–1027 (2009).
- [28] Zachariasen, W. H. *Journal of the American Chemical Society* **54**(10), 3841–3851 (1932).
- [29] Mott, N. *Contemporary Physics* **18**(3), 225–245 (1977).
- [30] Guttman, L. *AIP Conference Proceedings* **31**(1), 268–272 (1976).
- [31] Wooten, F., Winer, K., and Weaire, D. *Physical Review Letters* **54**(13), 1392 (1985).
- [32] Alder, B. J. and Wainwright, T. E. *The Journal of Chemical Physics* **27**(5), 1208–1209 (1957).

- [33] Alder, B. J. and Wainwright, T. E. *The Journal of Chemical Physics* **31**(2), 459–466 (1959).
- [34] Schlick, T. *Molecular modeling and Simulation*. Springer, New York, NY, (2002).
- [35] Ma, Q., Izaguirre, J. A., and Skeel, R. D. *SIAM Journal on Scientific Computing* **24**(6), 1951–1973 (2003).
- [36] Born, M. and Oppenheimer, R. *Annalen der Physik* **389**(20), 457–484 (1927).
- [37] Hohenberg, P. and Kohn, W. *Physical Review* **136**(3B), B864 (1964).
- [38] Kohn, W. and Sham, L. J. *Physical Review* **140**(4A), A1133 (1965).
- [39] Dirac, P. A. M. *j-MATH-PROC-CAMB-PHILOS-SOC* **26**(3), 376–385 (1930).
- [40] Slater, J. C. *Phys. Rev.* **81**, 385–390 (1951).
- [41] Martin, R. M. *Electronic structure: basic theory and practical methods*. Cambridge university press, (2004).
- [42] Elliott, S. R. *Physics of amorphous materials*. Longman Group, Longman House, Burnt Mill, Harlow, Essex CM 20 2 JE, England, (1983).
- [43] Hansen, J.-P. and McDonald, I. R. *Theory of simple liquids*. Elsevier, (1990).
- [44] Wegner, F. *Zeitschrift für Physik B Condensed Matter* **36**(3), 209–214 (1980).
- [45] Pasquarello, A., Sarnthein, J., and Car, R. *Phys. Rev. B* **57**, 14133–14140 (1998).
- [46] Allen, P. B. In *Conceptual foundations of materials : a standard model for ground- and excited-state properties*, 165–218. (2006).
- [47] Ziman, J. M. *Principles of the Theory of Solids*. Cambridge University Press, 2 edition, (1972).
- [48] Hershfield, S. and Ambegaokar, V. *Phys. Rev. B* **34**, 2147–2151 (1986).
- [49] Kubo, R. *J. Phys. Soc. Jpn.* **12**, 570–586 (1957).
- [50] Greenwood, D. A. *Proceedings of the Physical Society* **71**, 585–596 (1958).
- [51] Kubo, R., Toda, M., Hashitsume, N., and Saito, N. *Statistical physics. II: Nonequilibrium statistical mechanics*. Springer series in solid-state sciences, (1985).
- [52] Einstein, A. *Annalen der Physik* **322**(8), 549–560 (1905).

- [53] Mott, N. F. and Davis, E. A. *Electronic processes in non-crystalline materials / by N.F. Mott and E.A. Davis*. Clarendon Press ; Oxford University Press Oxford : New York, 2nd ed. edition, (1979).
- [54] Moseley, L. L. and Lukes, T. *American Journal of Physics* **46**(6), 676–677 (1978).
- [55] Zhang, M. and Drabold, D. A. *Journal of Physics: Condensed Matter* **23**(8), 085801 (2011).
- [56] Zhang, M.-L. and Drabold, D. A. *Phys. Rev. B* **81**, 085210 (2010).
- [57] Zhang, M. and Drabold, D. A. *Phys. Rev. E* **83**, 012103 (2011).
- [58] Galli, G., Martin, R. M., Car, R., and Parrinello, M. *Phys. Rev. B* **42**, 7470–7482 (1990).
- [59] Sobolev, A. N. and Mirzoev, A. A. *Journal of Physics: Conference Series* **98**(6), 062015 (2008).
- [60] Bose, S. K., Jepsen, O., and Andersen, O. K. *Phys. Rev. B* **48**, 4265–4275 (1993).
- [61] Desjarlais, M. P., Kress, J. D., and Collins, L. A. *Phys. Rev. E* **66**, 025401 (2002).
- [62] Dong, J. and Drabold, D. A. *Phys. Rev. Lett.* **80**, 1928–1931 (1998).
- [63] Landauro, C. and Solbrig, H. *Materials Science and Engineering: A* **294-296**, 600 – 603 (2000).
- [64] Hoi, B. D. and Yarmohammadi, M. *Journal of Magnetism and Magnetic Materials* **451**, 57 – 64 (2018).
- [65] Drabold, D. *Journal of Non-Crystalline Solids* **266-269**, 211 – 217 (2000).
- [66] Atta-Fynn, R., Biswas, P., and Drabold, D. A. *Phys. Rev. B* **69**, 245204 (2004).
- [67] Prasai, K., Biswas, P., and Drabold, D. A. *Semiconductor Science and Technology* **31**(7), 073002 (2016).
- [68] Drabold, D. A. and Fedders, P. A. *Phys. Rev. B* **60**, R721–R725 (1999).
- [69] Abtew, T. A., Zhang, M., and Drabold, D. A. *Phys. Rev. B* **76**, 045212 (2007).
- [70] Calderín, L., Karasiev, V., and Trickey, S. *Computer Physics Communications* **221**, 118 – 142 (2017).
- [71] Prasai, K., Chen, G., and Drabold, D. A. *Phys. Rev. Materials* **1**, 015603 (2017).
- [72] Prasai, K., Subedi, K. N., Ferris, K., Biswas, P., and Drabold, D. A. *physica status solidi (RRL) – Rapid Research Letters* **12**(9), 1800238 (2018).

- [73] Subedi, K. N., Prasai, K., and Drabold, D. A. *Modelling of Glasses: Electronic conduction mechanisms in $\text{GeSe}_3\text{:Ag}$ and $\text{Al}_2\text{O}_3\text{:Cu}$* . World Scientific Publishing; Singapore (2020).
- [74] Subedi, K. N., Prasai, K., Kozicki, M. N., and Drabold, D. A. *Phys. Rev. Materials* **3**, 065605 (2019).
- [75] Thapa, R., Bhattarai, B., Kozicki, M. N., Subedi, K. N., and Drabold, D. A. *Phys. Rev. Materials* **4**, 064603 (2020).
- [76] C. E. Parman, N. E. I. and Kakalios, J. *Phys. Rev. B* **47**, 12578–12589 (1993).
- [77] Xiao, B., Gu, T., Tada, T., and Watanabe, S. *Journal of Applied Physics* **115**(3), 034503 (2014).
- [78] Oakeshott, R. B. S. and MacKinnon, A. *Journal of Physics: Condensed Matter* **6**(8), 1513–1518 (1994).
- [79] Baranger, H. U. and Stone, A. D. *Phys. Rev. B* **40**, 8169–8193 (1989).
- [80] Paulsson, M. and Brandbyge, M. *Phys. Rev. B* **76**, 115117 (2007).
- [81] Lanczos, C. *Applied Analysis*. Prentice-Hall, Englewood Cliffs, New Jersey, (1956).
- [82] Drabold, D. A. and Sankey, O. F. *Phys. Rev. Lett.* **70**, 3631–3634 (1993).
- [83] Kresse, G. and Furthmuller, J. *Phys. Rev. B* **54**, 11169–11186 (1996).
- [84] Perdew, J. P., Burke, K., and Ernzerhof, M. *Physical Review Letters* **77**(18), 3865 (1996).
- [85] Bhattarai, B. and Drabold, D. A. *Carbon* **115**, 532 – 538 (2017).
- [86] Djordjević, B. R., Thorpe, M. F., and Wooten, F. *Phys. Rev. B* **52**, 5685–5689 (1995).
- [87] Barranco, A., Yubero, F., Espinós, J. P., Groening, P., and González-Elipe, A. R. *Journal of Applied Physics* **97**(11), 113714 (2005).
- [88] Drabold, D. A. *Eur. Phys. J. B* **68**, 1–21 (2009).
- [89] Feenstra, R. M. and Widom, M.
www.andrew.cmu.edu/user/feenstra/wavetrans/source/, (2012).
- [90] da Silva, D. S., Cortes, A. D. S., Oliveira, M. H., Motta, E. F., Viana, G. A., Mei, P. R., and Marques, F. C. *Journal of Applied Physics* **110**(4), 043510 (2011).
- [91] Grill, A. *Diamond and Related Materials* **8**(2), 428 – 434 (1999).

- [92] Park, K. and Chin, E. *Polymer Degradation and Stability* **68**(1), 93 – 96 (2000).
- [93] McEuen, P. L. *Nature* **393**, 585–596 (1998).
- [94] Nicholas, R. J., Mainwood, A., and Eaves, L. *Philosophical Transactions of the Royal Society A: Mathematical, Physical and Engineering Sciences* **366**(1863), 189–193 (2008).
- [95] Novoselov, K. S., Geim, A. K., Morozov, S. V., Jiang, D., Zhang, Y., Dubonos, S. V., Grigorieva, I. V., and Firsov, A. A. *Science* **306**(5696), 666–669 (2004).
- [96] Geim, A. K. and Novoselov, K. S. *Nature Materials* **6**, 181–191 (2007).
- [97] Konigsmark, S. T. C., Hwang, L. K., Chen, D., and Wong, M. D. F. In *2014 19th Asia and South Pacific Design Automation Conference (ASP-DAC)*, 73–78, (2014).
- [98] Wring, S. A. and Hart, J. P. *Analyst* **117**, 1215–1229 (1992).
- [99] Bhattarai, B., Biswas, P., Atta-Fynn, R., and Drabold, D. *Physical chemistry chemical physics : PCCP* **20**(29), 19546—19551 (2018).
- [100] Street, R. A. *Hydrogenated Amorphous Silicon*. Cambridge Solid State Science Series. Cambridge University Press, (1991).
- [101] Fedders, P. A., Drabold, D. A., and Nakhmanson, S. *Phys. Rev. B* **58**, 15624–15631 (1998).
- [102] Pan, Y., Inam, F., Zhang, M., and Drabold, D. A. *Phys. Rev. Lett.* **100**, 206403 (2008).
- [103] Abtew, T., Zhang, M., Pan, Y., and Drabold, D. *Journal of Non-Crystalline Solids* **354**(19), 2909–2913 (2008).
- [104] Inam, F., Lewis, J. P., and Drabold, D. A. *physica status solidi (a)* **207**(3), 599–604 (2010).
- [105] Fedders, P. A., Drabold, D. A., and Klemm, S. *Phys. Rev. B* **45**, 4048–4055 (1992).
- [106] Kim, T. H., Lee, G. W., Sieve, B., Gangopadhyay, A. K., Hyers, R. W., Rathz, T. J., Rogers, J. R., Robinson, D. S., Kelton, K. F., and Goldman, A. I. *Phys. Rev. Lett.* **95**, 085501 (2005).
- [107] Okada, J. T., Sit, P. H.-L., Watanabe, Y., Wang, Y. J., Barbiellini, B., Ishikawa, T., Itou, M., Sakurai, Y., Bansil, A., Ishikawa, R., Hamaishi, M., Masaki, T., Paradis, P.-F., Kimura, K., Ishikawa, T., and Nanao, S. *Phys. Rev. Lett.* **108**, 067402 (2012).
- [108] Mesaritakis, C., Akriotou, M., Kapsalis, A., Grivas, E., Chaintoutis, C., Nikas, T., and Syvridis, D. *Scientific Reports* **9653** (2018).

- [109] Brady, G. W. *J. Phys. Chem.* **63**(7), 1119 – 1120 (1959).
- [110] Philipp, H. R. *Journal of Non-Crystalline Solids* **8-10**, 627 – 632 (1972).
- [111] Simmons, J. G. and Verderber, R. R. *Radio and Electronic Engineer* **34**(2), 81–89 (1967).
- [112] Tappertzhofen, S., Valov, I., Tsuruoka, T., Hasegawa, T., Waser, R., and Aono, M. *ACS Nano* **7**(7), 6396–6402 (2013).
- [113] Kozicki, M. N. and Barnaby, H. J. *Semiconductor Science and Technology* **31**(11), 113001 (2016).
- [114] Dietrich, S., Angerbauer, M., Ivanov, M., Gogl, D., Hoenigschmid, H., Kund, M., Liaw, C., Markert, M., Symanczyk, R., Altimime, L., Bournat, S., and Mueller, G. *IEEE Journal of Solid-State Circuits* **42**(4), 839–845 (2007).
- [115] Tsuruoka, T., Terabe, K., Hasegawa, T., and Aono, M. *Nanotechnology* **21**(42), 425205 (2010).
- [116] Pandey, S. C., Meade, R., and Sandhu, G. S. *Journal of Applied Physics* **117**(5), 054504 (2015).
- [117] Tsai, T., Jiang, F., Ho, C., Lin, C., and Tseng, T. *IEEE Electron Device Letters* **37**(10), 1284–1287 (2016).
- [118] Barci, M., Molas, G., Cagli, C., Vianello, E., Bernard, M., Roule, A., Toffoli, A., Cluzel, J., Salvo, B. D., and Perniola, L. *IEEE Journal of the Electron Devices Society* **4**(5), 314–320 (2016).
- [119] Kittl, J., Opsomer, K., Popovici, M., Menou, N., Kaczer, B., Wang, X., Adelman, C., Pawlak, M., Tomida, K., Rothschild, A., and et al. *Microelectronic Engineering* **86**(7), 1789 – 1795 (2009).
- [120] Eklund, P., Sridharan, M., Singh, G., and Bøttiger, J. *Plasma Processes and Polymers* **6**(S1), S907–S911 (2009).
- [121] Gutiérrez, G., Belonoshko, A. B., Ahuja, R., and Johansson, B. *Physical Review E* **61**(3), 2723–2729 (2000).
- [122] Vashishta, P., Kalia, R. K., Nakano, A., and Rino, J. P. *Journal of Applied Physics* **103**(8), 083504 (2008).
- [123] Miranda Hernández J.G., Soto Guzmán, A. and Rocha-Rangel, E. *J.Ceram. Proc. Res* **7**, 311–314 (2006).
- [124] Blöchl, P. E. *Phys. Rev. B* **50**, 17953–17979 (1994).

- [125] Kresse, G. and Joubert, D. *Phys. Rev. B* **59**, 1758–1775 (1999).
- [126] Perdew, J. P. and Zunger, A. *Phys. Rev. B* **23**, 5048–5079 (1981).
- [127] Momida, H., Hamada, T., Takagi, Y., Yamamoto, T., Uda, T., and Ohno, T. *Phys. Rev. B* **73**, 054108 (2006).
- [128] Lamparter, P. and Kniep, R. *Physica B: Condensed Matter* **234-236**, 405 – 406 (1997).
- [129] Landron, C., Henet, L., Jenkins, T. E., Greaves, G. N., Coutures, J. P., and Soper, A. K. *Phys. Rev. Lett.* **86**, 4839–4842 (2001).
- [130] Chagarov, E. A. and Kummel, A. C. *The Journal of Chemical Physics* **130**(12), 124717 (2009).
- [131] Momida, H., Hamada, T., Takagi, Y., Yamamoto, T., Uda, T., and Ohno, T. *Phys. Rev. B* **73**, 054108 (2006).
- [132] Sankaran, K., Goux, L., Clima, S., Mees, M., Kittl, J., Jurczak, M., Altimime, L., Rignanese, G.-M., and Pourtois, G. volume 45, 317–330. Electrochemical Society, (2012).
- [133] Dawson, J. A. and Robertson, J. *The Journal of Physical Chemistry C* **120**(27), 14474–14483 (2016).
- [134] Prasai, K., Chen, G., and Drabold, D. A. *Phys. Rev. Materials* **1**, 015603 (2017).
- [135] Tang, W., Sanville, E., and Henkelman, G. *Journal of Physics: Condensed Matter* **21**(8), 084204 (2009).
- [136] Landau, L. D. *Phys. Z. Sowjetunion* **2**, 46 (1932).
- [137] Zener, C. *Proceedings of the Royal Society of London Series A* **137**, 696–702 (1932).
- [138] Pandey, A., Cai, B., Podraza, N., and Drabold, D. A. *Phys. Rev. Applied* **2**, 054005 (2014).
- [139] Kabir, M., Mookerjee, A., and Bhattacharya, A. K. *Phys. Rev. A* **69**, 043203 (2004).
- [140] Prasai, B. and Drabold, D. A. *Phys. Rev. B* **83**, 094202 (2011).
- [141] Subedi, K. N., Prasai, K., and Drabold, D. A. *arXiv e-prints*, arXiv:1901.04324 (2019).
- [142] Chaudhuri, I., Inam, F., and Drabold, D. A. *Phys. Rev. B* **79**, 100201(R) (2009).

- [143] Gallas, B., Kao, C.-C., Fisson, S., Vuye, G., Rivory, J., Bernard, Y., and Belouet, C. *Applied Surface Science* **185**(3), 317 – 320 (2002).
- [144] Chang, Y.-F., Chen, P.-Y., Fowler, B., Chen, Y.-T., Xue, F., Wang, Y., Zhou, F., and Lee, J. C. *Journal of Applied Physics* **112**(12), 123702 (2012).
- [145] Mehonic, A., Buckwell, M., Montesi, L., Garnett, L., Hudziak, S., Fearn, S., Chater, R., McPhail, D., and Kenyon, A. J. *Journal of Applied Physics* **117**(12), 124505 (2015).
- [146] Mehonic, A., Munde, M., Ng, W., Buckwell, M., Montesi, L., Bosman, M., Shluger, A., and Kenyon, A. *Microelectronic Engineering* **178**, 98 – 103 (2017). Special issue of Insulating Films on Semiconductors (INFOS 2017).
- [147] Jo, S. H., Kim, K.-H., and Lu, W. *Nano Letters* **9**(1), 496–500 (2009).
- [148] Jo, S. H. and Lu, W. *Nano Letters* **8**(2), 392–397 (2008).
- [149] Yao, J., Sun, Z., Zhong, L., Natelson, D., and Tour, J. M. *Nano Letters* **10**(10), 4105–4110 (2010).
- [150] Mehonic, A., Cueff, S., Wojdak, M., Hudziak, S., Jambois, O., Labbé, C., Garrido, B., Rizk, R., and Kenyon, A. J. *Journal of Applied Physics* **111**(7), 074507 (2012).
- [151] Barranco, A., Yubero, F., Espinós, J. P., Groening, P., and González-Elipe, A. R. *Journal of Applied Physics* **97**(11), 113714 (2005).
- [152] Nosé, S. *The Journal of Chemical Physics* **81**(1), 511–519 (1984).
- [153] Shuichi, N. *Progress of Theoretical Physics Supplement* **103**, 1–46 (1991).
- [154] Bylander, D. M. and Kleinman, L. *Phys. Rev. B* **46**, 13756–13761 (1992).
- [155] Yue, Y., Song, Y., and Zuo, X. *AIP Advances* **7**(1), 015309 (2017).
- [156] Munde, M. S., Gao, D. Z., and Shluger, A. L. *Journal of Physics: Condensed Matter* **29**(24), 245701 (2017).
- [157] Gao, D. Z., Strand, J., Munde, M. S., and Shluger, A. L. *Frontiers in Physics* **7**, 43 (2019).
- [158] Hirata, A., Kohara, S., Asada, T., Arao, M., Yogi, C., Imai, H., Tan, Y., Fujita, T., and Chen, M. *Nature Communications* **7**, 11591 (2016).
- [159] Lopes, M. and Shelby, J. E. *Introduction to Glass Science and Technology*. The Royal Society of Chemistry, (2005).
- [160] Vogel, E. M. *Journal of the American Ceramic Society* **72**(5), 719–724 (1989).

- [161] Oliveira, A., Malafaya, P., and Reis, R. *Biomaterials* **24**(15), 2575 – 2584 (2003).
- [162] Henderson, G. *Journal of Non-Crystalline Solids* **183**(1), 43 – 50 (1995).
- [163] Dupree, R., Holland, D., McMillan, P., and Pettifer, R. *Journal of Non-Crystalline Solids* **68**(2), 399 – 410 (1984).
- [164] Emerson, J., Stallworth, P., and Bray, P. *Journal of Non-Crystalline Solids* **113**(2), 253 – 259 (1989).
- [165] Nesbitt, H., Henderson, G., Bancroft, G., and Ho, R. *Journal of Non-Crystalline Solids* **409**, 139 – 148 (2015).
- [166] Fábíán, M., Jóvári, P., Sváb, E., Mészáros, G., Proffen, T., and Veress, E. *Journal of Physics: Condensed Matter* **19**(33), 335209 (2007).
- [167] Bauchy, M. *The Journal of Chemical Physics* **137**(4), 044510 (2012).
- [168] Li, X., Song, W., Yang, K., Krishnan, N. M. A., Wang, B., Smedskjaer, M. M., Mauro, J. C., Sant, G., Balonis, M., and Bauchy, M. *The Journal of Chemical Physics* **147**(7), 074501 (2017).
- [169] Pandey, A., Biswas, P., and Drabold, D. A. *Phys. Rev. B* **92**, 155205 (2015).
- [170] Zhou, Q., Du, T., Guo, L., Smedskjaer, M. M., and Bauchy, M. *Journal of Non-Crystalline Solids* **536**, 120006 (2020).
- [171] Du, J. and Cormack, A. *Journal of Non-Crystalline Solids* **349**, 66 – 79 (2004).
Glass Science for High Technology. 16th University Conference on Glass Science.
- [172] Du, J. and Corrales, L. R. *Journal of Non-Crystalline Solids* **352**(30), 3255 – 3269 (2006).
- [173] Pota, M., Pedone, A., Malavasi, G., Durante, C., Cocchi, M., and Menziani, M. *Computational Materials Science* **47**(3), 739 – 751 (2010).
- [174] Deng, L., Urata, S., Takimoto, Y., Miyajima, T., Hahn, S. H., van Duin, A. C. T., and Du, J. *Journal of the American Ceramic Society* **103**(3), 1600–1614 (2020).
- [175] Baral, K. and Ching, W.-Y. *Journal of Applied Physics* **121**(24), 245103 (2017).
- [176] Jabraoui, H., Vaills, Y., Hasnaoui, A., Badawi, M., and Ouaskit, S. *The Journal of Physical Chemistry B* **120**(51), 13193–13205 (2016).
- [177] Hung, P. K., Noritake, F., San, L. T., Van, T. B., and Vinh, L. T. *The European Physical Journal B: Condensed Matter and Complex Systems* **90**(10), 1–11 (2017).
- [178] Cai, B., Zhang, X., and Drabold, D. A. *Phys. Rev. B* **83**, 092202 (2011).

- [179] Ouyang, L. and Ching, W. Y. *Phys. Rev. B* **54**, R15594–R15597 (1996).
- [180] Mazurin, O. and Gankin, Y. *Journal of Non-Crystalline Solids* **342**(1), 166 – 169 (2004).
- [181] Birch, F. *Phys. Rev.* **71**, 809–824 (1947).
- [182] Murnaghan, F. D. *Proceedings of the National Academy of Sciences of the United States of America* **30**(1), 244–7 (1944).
- [183] Togo, A. and Tanaka, I. *Scr. Mater.* **108**, 1–5 Nov (2015).
- [184] Grimley, D. I., Wright, A. C., and Sinclair, R. N. *Journal of Non-Crystalline Solids* **119**(1), 49 – 64 (1990).
- [185] Wright, A. C., Clare, A. G., Bachra, B., Sinclair, R. N., Hannon, A. C., and Vessal, B. *Trans. Am. Crystallogr. Assoc* **27**, 239–254 (1991).
- [186] Johnson, P. A., Wright, A. C., and Sinclair, R. N. *Journal of Non-Crystalline Solids* **58**(1), 109 – 130 (1983).
- [187] Yu, Y., Wang, B., Wang, M., Sant, G., and Bauchy, M. *International Journal of Applied Glass Science* **8**(3), 276–284 (2017).
- [188] Nakano, A., Kalia, R. K., and Vashishta, P. *Journal of Non-Crystalline Solids* **171**(2), 157–163 (1994).
- [189] Du, J. and Corrales, L. R. *Phys. Rev. B* **72**, 092201 (2005).
- [190] Du, J. and Corrales, L. R. *Journal of Non-Crystalline Solids* **352**(30), 3255–3269 (2006).
- [191] Huang, C. and Cormack, A. N. *The Journal of Chemical Physics* **93**(11), 8180–8186 (1990).
- [192] Jen, J. and Kalinowski, M. *Journal of Non-Crystalline Solids* **38-39**, 21–26 (1980). XIIth International Congress on Glass.
- [193] Sakka, S. and Matusita, K. *Journal of Non-Crystalline Solids* **22**(1), 57 – 66 (1976).
- [194] Misawa, M., Price, D., and Suzuki, K. *Journal of Non-Crystalline Solids* **37**(1), 85 – 97 (1980).
- [195] Yuan, X. and Cormack, A. *Journal of Non-Crystalline Solids* **283**(1), 69 – 87 (2001).
- [196] Soules, T. F. *The Journal of Chemical Physics* **71**(11), 4570–4578 (1979).

- [197] Vessal, B., Amini, M., and Catlow, C. *Journal of Non-Crystalline Solids* **159**(1), 184 – 186 (1993).
- [198] van Beest, B. W. H., Kramer, G. J., and van Santen, R. A. *Phys. Rev. Lett.* **64**, 1955–1958 (1990).
- [199] Ispas, S., Benoit, M., Jund, P., and Jullien, R. *Phys. Rev. B* **64**, 214206 (2001).
- [200] Murray, R., Song, L., and Ching, W. *Journal of Non-Crystalline Solids* **94**(1), 133–143 (1987).
- [201] Yuan, X. and Cormack, A. *Journal of Non-Crystalline Solids* **319**(1), 31 – 43 (2003).
- [202] Donadio, D., Bernasconi, M., and Tassone, F. *Phys. Rev. B* **70**, 214205 (2004).
- [203] Pettifer, R., Dupree, R., Farnan, I., and Sternberg, U. *Journal of Non-Crystalline Solids* **106**(1), 408–412 (1988).
- [204] Mozzi, R. L. and Warren, B. E. *Journal of Applied Crystallography* **2**(4), 164–172 (1969).
- [205] Gibbs, G. V., Hamil, M. M., Louisnathan, S. J., Bartell, L. S., and Yow, H. *American Mineralogist* **57**, 1578–1613 (1972).
- [206] Pota, M., Pedone, A., Malavasi, G., Durante, C., Cocchi, M., and Menziani, M. *Computational Materials Science* **47**(3), 739–751 (2010).
- [207] Adelstein, N., Olson, C. S., and Lordi, V. *Journal of Non-Crystalline Solids* **430**, 9–15 (2015).
- [208] Murray, R. and Ching, W. *Journal of Non-Crystalline Solids* **94**(1), 144 – 159 (1987).
- [209] White, G., Birch, J., and Manghnani, M. H. *Journal of Non-Crystalline Solids* **23**(1), 99 – 110 (1977).
- [210] Zotov, N. *Journal of Physics: Condensed Matter* **14**(45), 11655–11669 (2002).
- [211] Mehl, M. J., Klein, B. M., and Papaconstantopoulos, D. A. *Intermetallic Compounds: Principles/ edited by J. H. Westbrook and R. L. Fleischer*, volume 1. Wiley, New York, (1994).
- [212] Hill, R. *Proceedings of the Physical Society. Section A* **65**(5), 349–354 (1952).
- [213] Surhone, L., Timpledon, M., and Marseken, S. *Woldemar Voigt*. VDM Publishing, (2010).

- [214] Bansal, N. P. and Doremus, R. H. *Handbook of glass properties*. Academic press, New York, (1986).
- [215] Priven, A. I. *Glass Technology* **45**(6), 244–254 (2004).
- [216] Du, J. and Corrales, L. R. *Journal of Non-Crystalline Solids* **352**(30), 3255 – 3269 (2006).
- [217] Pedone, A., Malavasi, G., Menziani, M. C., Cormack, A. N., and Segre, U. *The Journal of Physical Chemistry B* **110**(24), 11780–11795 (2006).
- [218] Pedone, A., Malavasi, G., Cormack, A. N., Segre, U., and Menziani, M. C. *Chemistry of Materials* **19**(13), 3144–3154 (2007).
- [219] Li, W., Li, D., Fu, Q., and Pan, C. *RSC Adv.* **5**, 80428–80433 (2015).
- [220] Cao, M., Luo, Y., Xie, Y., Tan, Z., Fan, G., Guo, Q., Su, Y., Li, Z., and Xiong, D.-B. *Advanced Materials Interfaces* **6**(13), 1900468 (2019).



OHIO
UNIVERSITY

Thesis and Dissertation Services